APPLICATION OF PANEL METHODS FOR SUBSONIC AERODYNAMICS

by

Meung Jung Kim

Dissertation submitted to the Faculty of the

Virginia Polytechnic Institute and State University

in partial fulfillment of the requirements for the degree of

Doctor of Philosophy

in

Engineering Mechanics

APPROVED:

D. T. Mook, Chairman

A. H. Nayfeh

D. P. Telionis

J. N. Reddy

L. T. Watson

January 1985

Blacksburg, Virginia

ACKNOWLEDGEMENTS

The author would like to take this opportunity to express his deep appreciation to Professor Mook for his continuous and patient guidance and assistance during the course of this work. The author would also like to use this opportunity to thank Professors Nayfeh, Reddy, Saric, Telionis, and Watson for their contribution to his education and for their help during the course of this research. Sincere appreciation is also extended to Professors Frederick and Sword for their continuous support and encouragement.

Infinite thanks are due to the author's wife, , two daughters, and , his parents, and his sisters, and , for continuous inspiration, encouragement, and support.

TABLE OF CONTENTS

LIST OF ILLUSTRATIONS

I. INTRODUCTION

1.1 INTRODUCTION AND LITERATURE REVIEW

With the development of aviation, shipbuilding, and other technical domains, the demand for aerodynamic and hydrodynamic data has increased, and it has been a long-standing problem to predict aerodynamic and hydrodynamic loads on, and details of flows over, various types of bodies.

In aerodynamics, these problems can be classified into two groups, nonlifting problems and lifting problems. Depending on the region of interest, these problems can also be studied as two-dimensional problems or three-dimensional problems.

For high-aspect-ratio wings, the flows can be considered two-dimensional except in small regions near the wing tips and wing roots. The two-dimensional problems are the stepping stone to fully three-dimensional problems, and steady two-dimensional problems have been well established compared to unsteady two-dimensional problems. The unsteady two-dimensional problems still pose some difficulties, such as implementation of the Kutta condition at the trailing edge.

Wagner[1925] obtained the solution for the linear time-dependent normalized circulatory lift (i.e., circulation) of a flat plate which started impulsively from rest at an infinitesimal angle of attack. Kussner[1940] obtained the normalized lift acting on a flat plate that is passing into a sharp-edged vertical gust of infinitesimal strength. The flat plate and its wake were assumed not to affect the gust boundary.

Kussner's function was later generalized by Drischler and Diederich[1957] to include the case of a gust with a horizontal as well as a vertical component of velocity. Theodorsen[1935] and Karman and Sears[1938] obtained the normalized lift acting on a flat plate undergoing simple harmonic oscillation.

A comprehensive analysis was done by Giesing[1968]. Giesing used constant source distributions over each element and put a constant vorticity distribution inside the airfoil in order to satisfy the Kutta condition. The vorticity shed into the wake was modelled with discrete vortices that were convected at local particle velocity at discrete time steps by the use of a predictor-corrector scheme. He showed that the nonlinear effects, due to airfoil thickness and relatively high angles of attack, retard the build-up of time-dependent circulation around impulsively started wings and wings entering a gust. He also showed the nonlinear effects on the time-dependent circulation of the amplitude and frequency of motion of wings oscillating in a steady stream. Later, Basu and Hancock[1978] used essentially the same numerical procedure except that the wake element adjoining the trailing edge was modelled with a vortex sheet and its relative position and length were determined as part of the solution. Basu and Hancock argued that there is no one mathematical statement of the Kutta condition that applies to all numerical schemes and thus the statement of the Kutta condition must correspond to the numerical scheme. In addition, Basu and Hancock found that there are significant differences among the various solutions at the beginning of the impulsive start.

All the methods have in common the linearization of the problem in a small neighborhood of each analytic time and modelling of the wake vortex sheet by a system of discrete vortices. A similar approach was used by Gorelov and Kulyaev[1971] for analysis of flow past a slender profile. Graham[1983] studied the initial development of the lift on an airfoil in an inviscid starting flow. He found that the initial development depends strongly on the rate at which the effective incidence changes compared with the rate of change of streamwise velocity, as well as the trailing edge angle. Moreover, impulsively started airfoils with trailing edge angles less than $\pi/2$ are subject to an initial singularity in the lift followed by decreasing lift and then monotonically increasing lift.

The mutual interaction of vortex sheets has also been studied by others, such as Moore[1974], Raj and Iversen[1978], Katz and Weihs[1978], and the results confirmed the experimental observations that for a small initial separation distance, the vortex sheets roll up together.

The unsteady Kutta condition has also been studied experimentally by Archibald[1975], Satyanarayana and Davis[1978], and Kadlec and Davis[1979], and theoretically/numerically by Karman and Sears[1938], Giesing[1969], and Basu and Hancock[1978]. For detailed discussions of the results, the reader may refer to them. Some discussions relevant to this work will be given at appropriate places in this thesis.

For a wing of infinite length (idealization of large aspect-ratio rectangular wings) the pressure distribution does not vary along the span. This condition cannot exist for finite wings since the pressure differences between the top and bottom have to disappear at the wing tips.

For the case of small-aspect-ratio, sharp-edge delta/delta-like wings, additional separations occur along a sharp leading edge even at small angles of attack. The flow reattaches to the upper surface of the wing, and the aerodynamic forces increase nonlinearly as the angle of attack increases. When this reattachment no longer takes place, the wing loses the aerodynamic forces abruptly (stall phenomenon).

The nonlinear relationships were found in the low-speed wind tunnel tests by Winter[1937], Bartlett and Vidal[1955], Peckham[1958], and Maskell[1962]. The nonlinear relationships were also confirmed in the experiments by others, such as Scholz[1949], Marsden, Simpson, and Rainbird[1957], Bergesen and Porter[1960], Earnshaw and Lawford[1964] and Hummel and Redeker[1972]. They observed the primary vortex at the wing tips of parallelogram wings and along the sharp leading edges of delta wings in the form of a concentrated vortex system. They also found that the core of this system moves inward as the leading edge bevel angle is reduced increasing the lift.

Earnshaw[1961] and Maskell[1962] experimentally observed that the rolled-up region of the vortex sheet emanating from the slender sharp-edged wing consisted of three regions: an outer convection dominated region, an inner region where the rolling-up distance is of the order of the diffusion distance and an inner, diffusion-dominated, viscous core that is very small. In addition, Winter, Peckham, and Maskell observed that the shape and strength of the principal vortex are relatively independent of the Reynolds number. This relative independence of viscosity suggests that the flow may be modelled by an inviscid, potential flow.

Marsden, et al[1957], Bergesen and Porter[1960], and Hummel[1967] observed a secondary vortex on delta wings due to the separation of the boundary layer near the leading edge. Peckham[1958] found that the strength of the secondary vortex is only about 5 per cent of the strength of the primary vortex. The possibility of a tertiary vortex near the leading edge of a delta wing was discussed by Hummel[1967] and Earnshaw[1967]. The effect of thickness on the lift was studied by Peckham[1958] and Belotserkovskii[1967]. They found that the lift decreases as the thickness increases.

Many theoretical methods have been developed to predict the aerodynamic forces. Bollay[1939], Scholz[1949], and others presented nonlinear lifting surface theories for low-aspect-ratio wings. The first fundamental investigation in nonlinear wing theory may be attributed to Bollay[1939]. He modelled the rectangular wing of zero aspect ratio(finite span with infinite chord) with a distribution of spanwise, bound vortices. The wing tip vortices are shed rearward at half the angle of attack in a plane perpendicular to the wing surface. Assuming the lift distribution and the downwash to be constant across the span, he expressed the total normal force coefficient as a nonlinear function of the angle of attack. This theory was also extended to small-aspect-ratio rectangular wings. This method gives fairly good results for small-aspect-ratio wings, but does not predict the flow details and lacks the general applicability for other planforms.

Recognizing the origin of the nonlinear lift, Brown and Michael[1954] and others attempted to solve this problem in a more rigorous way. They represented the vortices due to edge separation as free

vortices embedded in a potential flow at some position above the wing. By making assumptions concerning the forces acting on the free vortices and the vortex sheets connecting the separation line and the free vortices, they obtained relationships among "viscous lift", aspect ratio, and angle of attack. These theories are strictly restricted to sharp-edged wings under the assumption that the line of separation is known.

Noting the fact that none of the theories previously mentioned allow edge geometry as a parameter, Bartlett and Vidal[1955] investigated the effects of wing edges. In order to develop the general expressions suitable for predicting the nonlinear viscous effects that are inherent in aerodynamic characteristics of low-aspect-ratio wings, they examined the cross-flow-drag theory. The cross-flow-drag theory is based on the assumption that there is an additional normal force on each transverse cross section of a very low-aspect-ratio wing, stemming from the drag associated with the two-dimensional viscous flow around a long cylinder of similar section characteristics. It also assumes that the cross flow separates immediately at small angles of attack. This assumption is often erroneous, particularly for the case of round-edge wings. The results obtained by the cross-flow-drag theory with some corrections for edge effects were compared with the experimental data for various types of delta and rectangular wings. They concluded that the viscous contribution to the lift and pitching moment may be of a magnitude roughly equal to the potential contribution or there may be little or almost no viscous contribution, depending on the edge shape. This theory also lacks general applicability.

The leading edge suction analogy provides a method suitable for calculating the aerodynamic forces for various wing planforms. Polhamus[1966] reasoned that the normal force needed for the flow around a leading edge to reattach to the wing is equivalent to the leading edge suction force necessary to force the flow to be attached to the leading edge in an unseparated condition. The unseparated leading edge suction is calculated and then rotated normal to the wing to obtain the lift contribution of the leading edge vortex. Later, Polhamus extended this method to account for the effect of compressibility by using a Prandtl-Glauert transformation. Bradley, Smith, and Bhateley[1973] extended Polhamus' method to more general planforms. Ericsson and Reding[1975], from their studies of steady and unsteady aerodynamics of sharp edged slender wings, developed a semi-empirical approximation for the vortex induced loads and showed that the analytic approximation for sharp edged slender wings gives a good prediction of experimentally determined loads. Lamar[1977] made comparisons with experimental data and the combination of direct and indirect edge forces through the use of the suction analogy for various planforms. In general, the total lift calculated by these methods agrees well with experimental data, but these methods cannot show the flow details or detailed surface pressures either.

Several attempts had been made in the past toward the theoretical prediction of flow details. Most of these methods were limited to slender configurations. After considerable simplification, the problem was reduced to finding the solution of Laplace's equation in the cross-flow plane. Mangler and Smith[1959] developed a conical flow method, which was later improved by Smith[1966]. They could predict qualitatively the

pressure distributions that had been observed experimentally. The conical flow methods overpredict the experimental load distributions considerably near the trailing edge because these methods do not satisfy the Kutta condition. The conical flow methods were followed by fully three-dimensional methods.

There are basically two techniques currently employed to solve for aerodynamic loads on a wing: mode function methods (or kernel function methods) and discrete element methods. In the mode function methods, the unknown downwash velocity on the wing is related to the pressure function by means of an integral. Then, the pressure function is approximated by a preselected interpolation function on the discretized elements. In contrast to mode function methods, the discrete element methods assume the singularity function on the discretized elements(panels) and solve for singularity distributions. Both methods form a linear set of equations by satisfying the boundary conditions. Some discussions on mode function methods can be found in papers by Watkins, Woolston, and Cunningham[1959] and Rowe, Redman, Ehlers, Sebastian[1975]. The discrete element methods are discussed next.

The discrete vortex lattice methods are based on the ideas of Joukowski about the mechanism of formation of lift and the associated vortices and Prandtl's model explaining the orgin of circulation on a wing in an ideal medium (see Prandtl and Tietjens[1931]). In steady problems the numerical method of discrete vortices was first systematically introduced by Falkner[1953]. Other variants of the methods followed in connection with steady and unsteady linear problems. The linear problems were soon followed by nonlinear problems.

The discrete vortex methods approximate the distribution of vorticity by a concentrated vortex filament. The lifting surface is then represented by a vortex lattice and the wake by a finite number of vortex lines which extend to infinity. Ermolenko[1966] introduced a system of spanwise vortex lines to model small aspect ratio rectangular wings with wakes emanating from both wing tips. This method has the same limitations as Bollay's method. Belotserkovskii[1969] first introduced an iterative procedure to determine the position of each segment of a system of line vortices which represents the wake. He successfully applied this method to flow past parallelogram wings at large angles of attack. Rehbach[1973], Mook and Maddox[1974] and Kandil ,Mook, and Nayfeh[1976] independently extended the methods allowing leading edge separation. Later, these methods were extended and refined to treat general unsteady problems by Atta[1978], Atta, Kandil, Mook and Nayfeh[1977], Atta and Nayfeh[1978], Thrasher, Mook, Kandil and Nayfeh[1977], Kandil, Atta and Nayfeh[1977], Atta[1978], and Thrasher[1979]. Independent improvements of these methods were made by others, such as Belotserkovskii and Nisht[1974], Summa[1975], Rehbach[1973,1974] and Lavin and Katz[1981]. The vortex lattice methods were further improved to handle small harmonic oscillations by Nayfeh, Mook and Yen[1979], and Konstandinopoulos[1981].

The vortex lattice methods, which are applied to harmonic oscillatory problems, are called doublet lattice methods. The doublet lattice methods have been used by many researchers, such as Albano and Rodden[1969], Kalman, Rodden, and Giesing[1971], and Giesing, Kalman, and Rodden[1972]. A quasi-vortex lattice method was developed by Lan[1974] to solve thin wing problems. The spanwise vortex distribution was assumed

to be piecewise constant while the chordwise vortex integral was reduced to a finite sum through a modified trapezoidal rule and the theory of Chebychev polynomials. The nonlinear vortex lattice method was also used by Angelucci[1971] to treat the flow past axisymmetric bodies at an angle of attack under the name of the multi-vortex method. The subvortex technique, which is based upon vortex lattice theory, was used by Maskew[1977] to reduce the errors in near field calculations arising from discretization. He introduced a near field model in which a vortex splits into an increasing number of subvortices as it is approached. By considering two-dimensional problems, he demonstrated that this subvortex technique yields accurate velocities anywhere in the flow field.

In a somewhat different approach, Raj and Gray[1979] developed an iterative method which uses the Bio-Savart law to relax the surface vorticity strength in successive iterations rather than using an integral equation formulation. They applied this method to the flow past a semi-infinite circular cylinder with a spherical tip at one side and showed that convergence was achieved in a few steps.

The boundary integral equation methods(BIEM) are based on the boundary integral representation of the field equations (e.g., Laplace's equation) obtained from Green's theorem (see Chap.2). This method is also called boundary element method (BEM). The governing equations are solved only on the boundary of the required solution domain. Depending on the use of fundamental solutions, BIEM is sometimes called the method of fundamental solutions(MFS). For further information on BIEM's, the reader may refer to Helmholtz[1860], Rayleigh[1887], Kirchoff[1882], Fredholm[1903], Proudman[1925], Jaswon and Ponter[1963], Jaswon[1963],

Symm[1963], Brebbia[1980], Fairweather and Johnston[1982], and Johnston and Fairweather[1984].

The panel method is one of the boundary integral methods. A continuous distribution of singularities on the surface of the body is approximated by a number of piecewise (continuous) distributions of singularity on the surface elements(i.e., panels). The panels are obtained by dividing the surface of the body into a finite number of elements. The singularity strength on a typical panel is given by a function. The integral equation is computed for the function on each panel. The boundary conditions are only satisfied at a finite number of points (i.e., control points) on the surface of the body. The evaluation of these discrete singularity distributions by applying the boundary conditions leads to a large algebraic system. By solving this system, the singularity strengths and thereby the flow field can be determined.

Depending upon the location of the panels, these methods are sometimes classified as surface panel methods, mean surface panel methods, and field panel methods. The field panel methods deal with plane nonlinear subsonic flow equations and the panel mesh covers the whole flow field. This method is based on an idea of Oswatitsch[1950]. The plane nonlinear subsonic flow, which is governed by a Poisson equation, may be treated as an incompressible flow on which another flow field is superimposed. Another flow field is created by compressibility sources throughout the flow field whose strength is equivalent to the term on the right hand side of the Poisson equation (e.g., Kandil[1983]). Depending upon the order of the singularity function, those are divided into first(or low)-order panel methods and higher-order panel methods. The

first-order panel methods employ a constant strength singularity on a panel. Also, those are classified as source panel methods, doublet panel methods, and vorticity panel methods depending upon the type of singularity. In many cases a combination of two types of singularities is used.

One of the first applications of the panel methods was to solve two-dimensional nonlifting problems (e.g., Smith and Hess[1962], Hess[1964] and Giesing[1965]). The consideration of lift in two-dimensional cases was soon possible (e.g., Giesing[1968]). The two-dimensional methods were soon followed by fully three-dimensional panel methods.

Hess and Smith[1962] introduced a constant source panel method and applied it to nonlifting problems. In their approach they used a quadrilateral element whose corners are projections of the four corners of the actual element on the body surface onto the tangent plane. The source distribution over a quadrilateral element was assumed constant. The method was applied to flows over various three-dimensional nonlifting bodies. The agreement between theoretical solutions and experimental results was generally good. Rubbert and Saaris[1968] modified the three-dimensional method of Hess and Smith[1962] to include lift effects.

Hess[1972] extended his method to include lift effects. Vortex distributions were placed on the upper and lower surfaces of the wing, with both vortex layers flowing off at the trailing edge. A somewhat different approach was used by Woodward, Tinoco, and Larsen[1967] in applying a panel method to a three-dimensional case. The general thick wing at an angle of attack was treated by: (1) separating the thickness and

camber problems, (2) linearizing the boundary conditions(the boundary conditions are satisfied on the mean chord line rather than the actual surface), and (3) distributing a singularity on the wing chord line. This method which was initially developed only for supersonic flows was later extended to the subsonic region and further refined by Carmichael[1971].

Asfar, Mook, and Nayfeh[1979] utilized a combination of vortex lattice and constant sources to represent the body surface and tested the method for several nonlifting cases. They concluded that a vortex lattice method alone can be used for the flow over an arbitrary three-dimensional body at least as well as, and in many cases better than, a source distribution alone. Moreover, for blunt bodies, the combination of the vortex lattice with sources was shown to give better results. For slender bodies, the vortex lattice alone was superior to a combination.

The constant doublet panel methods were used to treat potential flows about three-dimensional lifting configurations by Summa[1975,1977]. Maskew[1982] introduced a method which uses piecewise constant doublet and source singularities. Calculated results were compared with higher-order solutions for a number of cases. It was demonstrated that the low-order method gives comparable accuracy to higher-order solutions for comparable density of control points.

The higher-order panel methods have been developed to overcome difficulties connected in general with the first-order approach such as leakage problems, inaccuracy of the velocity gradient for boundary layer calcualtions and improper treatment of critical regions such as wing root and wing tip. The surface panels are no longer planar and the elementary singularity distribution on each panel can have a linear, parabolic or

higher-order behavior with spline fitting across the panel boundaries. Johnson and Rubbert[1975] introduced an advanced panel method. The method employs curved quadrilateral panels over which there is a combination of linear source and quadratic doublet distributions. The technique appears versatile and adaptable to complex panel patterns. The method especially appears not to be sensitive to the panel shapes employed. Weber, Brune, Johnson, Lu, and Rubbert[1976] and Johnson, Tinoco, Lu, and Epton[1979] developed similar methods to treat three-dimensional flows over wings with leading edge vortex separation. Johnson, Tinoco, Lu, and Epton[1979] later improved the previous method in order to overcome two major shortcomings, namely convergence failures in seemingly random cases, and over prediction of lift coefficients for high-aspect-ratio wings. They introduced improved panel numerics in an attempt to eliminate the highly nonlinear effects of ring vortices around doublet panel edges, and developed a least squares penalty procedure to damp the instability that causes divergence of numerical calculations. However they were forced to use a fixed design wake to correct the second problem.

Some other methods were developed based on similar concepts. Among them are doublet point methods (e.g., Lawrence and Gerber[1952] and Ueda and Dowell[1982]) and interior singularity panel methods (e.g., Chen and Dalton[1982]). In the approach of Ueda and Dowell, the lifts of individual panels were represented by single concentrated forces which correspond to the acceleration doublet points mathematically. The method employed by Chen and Dalton is closely related to the mean surface panel methods.

In contrast to source/doublet panel methods, the continuous vorticity panel methods have not attracted much attention so far, despite being well known in mathematics. The continuous panel methods employ continuous distributions of vorticity on the configuration surface. Yen, Mook, and Nayfeh[1980] introduced a method that utilized linear vorticity distribution over a planar triangular panel. Both the lifting surface and the wakes were modelled by the same linear vorticity panels. The tight rolling-up of the wakes was lumped into equivalent concentrated vortex filaments. Kandil, Chu, and Tureaud[1984] extended this method to unsteady flows under the name of the hybrid vortex method. The lifting surfaces treated by them were planar and of no thickness. It is evident that those methods can not be applied to nonplanar configurations.

1.2 MOTIVATION

With the appearance and development of electronic computers and progress in the realms of theoretical aerodynamics and computational mathematics, a number of computational methods have been developed for predicting the aerodynamic loads and pressure distribution on a wing. The vortex lattice methods, doublet(source) panel methods, and vorticity panel methods comprise most of the methods and have been used successfully on the various types of bodies. Each method has certain advantages as well as disadvantages over other methods.

The vortex lattice methods are very simple to use and yield generally accurate total loads. However these methods do not always lead to accu-

rate predictions of pressure distributions due to the strong algebraic singularity associated with the Bio-Savart law.

The doublet panel methods are generally reliable and versatile and can predict accurately the total loads as well as the pressure distributions on the wing. But, from the manner in which quadrilateral elements are formed in the doublet panel methods, it is evident that there are small openings between elements. These openings are responsible for the inability to satisfy the continuity of the derivatives of the doublet strength between elements. Moreover, in evaluating the velocity field one must consider the transfer of the integral from the actual to the approximating surface.

In contrast to the vortex lattice methods and doublet panel methods, the continuous vorticity panel methods have not attracted much attention in aerodynamics until now. There are some major differences between the vorticity panel methods and other methods. First, since the vorticity field is divergenceless, the approximating vorticity function over each element must satisfy this divergenceless condition (i.e., conservation condition). The additional equations from the conservation condition over each element can create a storage problem as well as render the influence matrix equations ill-posed. Secondly, the vorticity must be tangent to the boundary (see Chap. 2). The tangency condition causes some difficulty in handling the nonplanar or three-dimensional configurations. In other words, the tangency condition is violated whenever the discretized surface loses continuity of the slopes along the edges of elements. Violation of the tangency condition is equivalent to violation of the continuity condition for vorticity on the surface on assembly in

the finite element sense. Thirdly, the surface velocities are directly related to the surface vorticities which are the primitive unknowns of the problem. Direct interpretation of the surface velocities saves computational time and may increases the computational accuracy.

The two major problems, i.e., the large matrix system due to the conservation conditions over each element and the discontinuity of the surface vorticities on assembly which is crucial to finite element type methods, had not been overcome in the past. The theoretical framework did exist, though (see Strang and Fix[1973], Fix[1975], and Fix[1979]). These two problems appear to have deterred people from using the vorticity panel methods although the methods have many advantages, e.g., direct interpretation of surface velocities, over other methods.

In this thesis, three continuous vorticity panel methods and an advanced continuous source panel are developed overcoming the major problems mentioned above. These methods are applied to two-dimensional unsteady bodies, three-dimensional nonlifting bodies, and thin and thick lifting bodies.

In Chapter 2, the basic equations are stated for an incompressible, inviscid fluid. Further, the governing equations are transformed to integral equations with the help of Green's theorem.

In Chapter 3, a vorticity panel method is used to model the two-dimensional, unsteady flows. The body surface is modelled with a vortex sheet which wraps around the body and joins at the trailing edge. The wake is modelled with discrete vortices. The nonlinearity due to wake distortion and geometry is examined as part of this work.

In Chapter 4, a source panel method and a vorticity panel method are developed. Both methods use the triangular element over which the linear singularity function is distributed. The source panel method employs a curved surface to investigate the effect of weakly nonlinear geometry. The vorticity panel method uses flat elements and satisfies the tangency condition by introducing a scheme of rotation. The constraint conditions are satisfied together with the influence matrix equations in a least squares sense.

In Chapter 5, the vorticity panel method developed in Chapter 4 is extended to treat lifting body problems with separations along the sharp edges. Two schemes are considered: thin wing problems and thick wing problems. The lifting surface is modelled with continuous vorticity panels while the wakes are modelled with a number of discrete lines which extend to infinity. This combination enables one to calculate continuous pressure distributions on the lifting surface and to capture the tightly rolled-up wakes along the sharp edges.

In Chapter 6, some conclusions and recommendations concerning further extensions and improvements of the present methods are discussed.

II. PHYSICS AND BOUNDARY INTEGRAL REPRESENTATION

Here we briefly review the basic equations that govern the motion of an inviscid incompressible fluid, develop the boundary-integral representations, and discuss the boundary conditions.

2.1 PHYSICS

The continuity equation for an incompressible fluid is

$$\text{div } \bar{V} = 0 \tag{2.1}$$

Here the V is the velocity in the flow field. For irrotational flows, the pressure is related to the velocity through Bernoulli's equation (an integral of the momentum equation):

$$\partial\Phi/\partial t + P/\rho + V^2/2 = P_r/\rho + V_r^2/2 \tag{2.2}$$

where the subscript r denotes the 'reference state', Φ is the velocity potential, P is the pressure and ρ is the density of the fluid. In this thesis, considerations are given mostly to flows related to the motion of a body through a fluid which is otherwise undisturbed; hence Φ_r is not a function of time.

Here considerations are limited to solid surfaces so that fluid does not penetrate the boundary. The no-penetration condition is

$$\bar{V} \cdot \bar{n} = \bar{V}_B \cdot \bar{n} \tag{2.3}$$

everywhere on the surface of the body and the subscript B means 'Body'. Conditions at infinity are given by prescribing the velocity (usually zero) and pressure, which are used as a reference state.

$$\bar{V}_r = \bar{V}_\infty = 0 \quad \text{and} \quad P_r = P_\infty \tag{2.4}$$

The vorticity Ω is defined by

$$\bar{\Omega} \equiv \text{curl } \bar{V} \tag{2.5}$$

Depending on the value of Ω, the velocity field, or flow, is called either rotational ($\Omega \neq 0$) or irrotational ($\Omega = 0$). In this thesis both rotational and irrotational velocity fields are used to develop the numerical schemes.

2.2 BOUNDARY INTEGRAL REPRESENTATION

It follows from Equation 2.5 that for irrotational flow, the velocity field can be represented by the gradient of a scalar.

$$\bar{V} = \nabla \phi \tag{2.6}$$

where ϕ is called a velocity potential. Substituting Equation 2.6 into Equation 2.1. yields the well known Laplace's equation.

$$\nabla^2 \phi = 0 \tag{2.7}$$

Here we note that the irrotational motion of an ideal fluid involves only two scalar unknowns (the pressure and the velocity potential) rather than four scalar unknowns (the pressure and the three components of the velocity). Moreover, the unknowns in the general motion of an ideal fluid must be determined by simultaneously solving the continuity equation and the equation of motion. For irrotational motion, however, this is no longer necessary because one can solve for the potential from the continuity equation independently of the equation of motion. Thus, the entire problem of irrotational motion of an ideal fluid reduces to one of solving for the velocity potential from the continuity equation, Equation 2.7.

For rotational flow, one is concerned with the problem of expressing the velocity field in terms of the vorticity field. The continuity equation suggests that the velocity field may be expressed as the curl of a vector.

$$\bar{V} \equiv \nabla \times \bar{A} \tag{2.8}$$

where A is called the vector potential.

Substituting Equation 2.8 into Equation 2.5 and taking div A = 0, we obtain

$$\nabla^2 \bar{A} = - \bar{\Omega} \tag{2.9}$$

It is permissible to put div A = 0 because the vector potential is indeterminate to the extent of a gradient of a scalar. The significance of this is that the vorticity vector must be tangent to the boundary of the region of vorticity and the proof is given in Appendix A. Here the problem at hand is to determine the unknown vector potential by solving Poisson's equation.

In order to find the solutions of Laplace's equation or Poisson's equation, we begin with the divergence theorem:

$$\int\int_{\tau}\int \nabla \cdot \bar{B} \, d\tau = \int_{\sigma}\int \bar{B} \cdot \bar{n} \, d\sigma \tag{2.10}$$

where τ is the domain enclosed by the boundary σ, n is an outward normal unit vector from the domain, and B is continuous in τ. By setting $B = u\nabla v$, where u and v are any admissible functions which satisfy the continuity conditions in σ and τ, Green's second theorem is obtained:

$$\int\int_{\tau}\int \{u\nabla^2 v - v\nabla^2 u\} d\tau = \int_{\sigma}\int \{u\partial v/\partial n - v\partial u/\partial n\} d\sigma \tag{2.11}$$

In order to use this theorem to solve Poisson's equation, we introduce singularity functions that have a picking-out property. They are 1/r for three-dimensional problems and $\ell n(r)$ for two-dimensional problems where

r is the distance between two field points, $P(x,y,z)$ and $Q(\xi,\eta,\zeta)$. The singularity function is harmonic except at $r = 0$ and can be expressed in three dimensions as:

$$\nabla^2(\frac{1}{r}) = -4\pi\,\delta(r) \tag{2.12}$$

where $\delta(r)$ is a Dirac delta function. For a more detailed discussion of the subject the reader may refer to any standard book on partial differential equations (e.g.,Chester[1971]).

For the three dimensional problem, we set $u = 1/r$. Then Equation 2.11 becomes

$$\int\int_\tau\int \{\frac{1}{r}\nabla^2 v - v\nabla^2\frac{1}{r}\}d\tau = \int_\sigma\int \{\frac{1}{r}\partial v/\partial n - v\partial(1/r)/\partial n\}d\sigma \tag{2.13}$$

Using the picking-out property, we obtain

$$v(P) = -\frac{1}{4\pi}\left[\int\int_\tau\int \frac{1}{r}\nabla^2 v\, d\tau - \int_\sigma\int \{\frac{1}{r}\partial v/\partial n - v\partial(1/r)/\partial n\}d\sigma\right] \tag{2.14}$$

where ξ, η, ζ are the variables of integration. If the problem is two dimensional, the factor 4π is replaced by 2π and the singularity function $1/r$ is replaced by $\ell n(r)$ in Equation 2.14.

$$v(P) = -\frac{1}{2\pi}\left[\int_\sigma\int \ell n(r)\nabla^2 v\, d\sigma + \int_c\{\ell n(r)\partial v/\partial n - v\partial\ell n(1/r)/\partial n\}ds\right] \tag{2.15}$$

Equations 2.14 and 2.15 say that the unknowns can be expressed in terms of an integral over the domain plus an integral over the boundary. These equations are the starting point for the determination of the specific formulae for the various cases.

For three-dimensional irrotational flow, we view the flow field as the region outside a closed body defined by the surface σ in three dimensions or the curve C in two dimensions. Then we identify v with the velocity potential and note that $\nabla^2\phi = 0$ everywhere in τ. Then Equations 2.14 and 2.15 become

$$\phi(P) = -\frac{1}{4\pi}\int_\sigma\int \{\frac{1}{r}\partial\phi/\partial n - \phi\partial(1/r)/\partial n\}d\sigma \tag{2.16}$$

for three dimensional flows and

$$\phi(P) = -\frac{1}{2\pi}\int_C \{\ell n(r)\partial\phi/\partial n - \phi\partial(\ell nr)/\partial n\}ds \tag{2.17}$$

for two-dimensional flows. The first term of the integrand represents a source distribution and the second term a doublet distribution. It can be shown (e.g., Karamcheti, Chester) that either one is sufficient. In our approach, rather than using both singularity distributions on the boundary, we employ only the source distribution over the boundary. Taking the gradient of the velocity potential, we obtain the velocity in the following form:

$$\bar{V}(x,y,z) = \frac{1}{4\pi}\nabla_P\left[\int_\sigma\int \frac{S(\xi,\eta,\zeta)d\sigma(\xi,\eta,\zeta)}{r}\right] \tag{2.18}$$

where

$$r \equiv |\bar{r}(x,y,z) - \bar{r}'(\xi,\eta,\zeta)| = \sqrt{\{(x-\zeta)^2 + (y-\eta)^2 + (z-\zeta)^2\}}$$

We shall use this equation for the source formulation in Chapter 4.

For three-dimensional rotational flow, substituting Equation 2.9 into Equation 2.14 , leads to

$$\bar{A}(x,y,z) = -\frac{1}{4\pi}\int\int_{\tau}\int \frac{\bar{\Omega}}{r}\, d\tau(\xi,\eta,\zeta) \tag{2.19}$$

Here we assumed that the body was part of the flow field. Assuming that the vorticity is confined to the surface of the body, we take the limit by letting the thickness of the region of vorticity go to zero and the vorticity go to infinity in such a way that the thickness times vorticity remains constant. In this way the region of vorticity becomes a vortex sheet. Taking the curl of the vector potential, we obtain

$$\bar{V}(x,y,z) = -\frac{1}{4\pi}\nabla_P \times \left[\int_{\sigma}\int \frac{\bar{\Omega}}{r}\, d\sigma(\xi,\eta,\zeta)\right] \tag{2.20}$$

Note that the Ω now represents the strength (vorticity times thickness) of the vortex sheet rather than the vorticity in the domain. If the domain of the vorticity is assumed to be a vortex filament, the velocity formula becomes

$$\bar{V}(x,y,z) = \frac{\Gamma}{4\pi h}(\cos\theta_1 - \cos\theta_2)\,\bar{e}_P \tag{2.21}$$

where the e_p is the unit vector perpendicular to the plane formed, according to right hand rule, by the vortex filament and the field point P, and Γ is the constant circulation around the vortex filament. For

further details, the reader may refer to the book by Karamcheti[1980]. This is the well known Bio-Savart law.

Had the problem been developed in two dimensions, the velocity induced by the vortex sheet would be

$$\bar{V}(x,y) = \frac{1}{2\pi} \nabla_P \times [\int_c \gamma(\xi,\eta)\, \bar{k}\, \ell n(r)\, ds] \tag{2.22}$$

where k is the unit vector in the z-direction out of the plane of motion and the velocity induced by a vortex filament would be

$$\bar{V}(x,y) = \frac{\Gamma}{2\pi h} \bar{e}_P \tag{2.23}$$

More details of the development of velocity formulas can be found in Karamcheti. We will use Equation 2.18 and Equations 2.20 - 2.23 to develop the numerical schemes in the following chapters.

III. UNSTEADY TWO-DIMENSIONAL LIFTING FLOWS

3.1 GENERAL

Here we develop a numerical method that can predict the aerodynamic forces and the details of the flow past an airfoil executing arbitrary two-dimensional maneuvers. The present method is based upon a continuous distribution of vorticity over the surface. Such distributions of surface singularities have been used to model steady flows (e.g.,Raj and Gray[1978]), but the extension to unsteady flows has not been effected. Here we describe one way in which this can be done. Unlike the earlier schemes used to attack this problem, the present approach views the body as moving through the air and poses the mathematical problem in terms of a moving coordinate system attached to it. If the airfoil is deforming with time, then the moving coordinate system is attached to a reference configuration. The airfoil can execute arbitrary two-dimensional maneuvers.

The present approach provides an attractive alternative to the earlier treatments of this same problem, being easy to formulate, easy to use, and very accurate. Its accuracy stems from the fact that the basic unknowns are primitive variables, the values of the potential-flow velocity on the surface of the airfoil.

3.2 BACKGROUND

The position and orientation of the moving frame are given by $R_A(t)$ and $\theta(t)$ as shown in Figure 1. It follows that

$$\bar{R} = \bar{R}_A + \bar{r} \tag{3.1}$$

where

$$\bar{R} = X\,\bar{I} + Y\,\bar{J}$$

$$\bar{R}_A(t) = X_A(t)\,\bar{I} + Y_A(t)\,\bar{J}$$

and

$$\bar{r}(t) = x(t)\,\bar{i} + y(t)\,\bar{j}$$

Substantial differentiation of Equation 3.1 yields

$$\bar{V} = \bar{V}_A + \bar{\Omega} \times \bar{r} + \bar{v} \tag{3.2}$$

where V is the velocity of a fluid particle with respect to the fixed reference frame (the absolute velocity), v is the velocity with respect to the moving frame (the relative velocity), V_A is the absolute velocity of the origin of the moving frame, Ω is the angular velocity of the moving frame ($\Omega = d\theta/dt\ k$), and r is the position of the fluid particle relative to the moving frame.

When the airfoil moves, it sets the air in motion which creates vorticity in the boundary layer on its surface. In an unsteady flow, the distribution of this vorticity changes, causing the circulation around the airfoil to change. The Kelvin-Helmholtz theory of conservation of

vorticity and experimental observations in an inviscid fluid dictate that the change in circulation around the airfoil is matched by a change in circulation around the wake of equal magnitute and opposite sign, that vorticity enters the wake when it is shed from the trailing edge, and that vorticity is convected away from the airfoil at the local particle velocity.

Using the ideas of boundary-layer theory, one can readily verify that the integral of curl V across the boundary-layer equals the velocity of the outer flow on the surface. The surface vorticity, equivalently surface velocity, is the unknown. Outside the boundary layer and wake the flow is irrotational. The loads are computed from the pressure on the surface, which is given by Bernoulli's equation. The form of Bernoulli's equation applicable to a moving frame is discussed next.

The potential function expressed in terms of R and t is denoted by Φ, while the one in terms of r and t is denoted by ϕ. Both potentials describe the same velocity field; thus,

$$\bar{V} = \nabla_R \Phi = \nabla_r \phi \tag{3.3}$$

Because r must change with time when R is constant, the time derivatives are related by

$$\frac{\partial \Phi}{\partial t}\Big|_R = \frac{\partial \phi}{\partial t}\Big|_r - \bar{V} \cdot (\bar{V}_A + \bar{\Omega} \times \bar{r}) \tag{3.4}$$

where $|_R$ indicates R is constant and $|_r$ indicates r is constant. In a fixed reference frame Bernoulli's equation has the form

$$\frac{\partial \Phi}{\partial t} + \frac{V^2}{2} + \frac{P}{\rho} = H(t) \tag{3.5}$$

where V is the magnitude of the velcity, ρ is the density, P is the pressure, and H(t) is a spatially uniform function of time. At large distances from the airfoil and its wake, P is constant and V is zero. Hence, we let $H(t)=P_\infty/\rho$ a constant. Using this and Equation 3.4, one can re-write Equation 3.5 as

$$\partial\phi/\partial t - \bar{V} \cdot (\bar{V}_A + \bar{\Omega} \times \bar{r}) + V^2/2 + P/\rho = P_\infty/\rho \tag{3.6}$$

It is convenient to introduce dimensionless variables(denoted by asterisks)

$$\bar{V} = U_c \bar{V}^*, \quad \bar{V}_A = U_c \bar{V}_A^*, \quad \bar{\Omega} = U_c \bar{\Omega}^*/L_c \tag{3.7}$$
$$\bar{r} = L_c \bar{r}^*, \quad \text{and } t = L_c t^*/U_c$$

where U_c and L_c are a characteristic speed and a characteristic length. Here we take L_c to be the chord. Substituting these definitions into Equation 3.6 and then dropping the asterisks in the result leads to

$$\begin{aligned} C_P &= (P - P_\infty)/(\rho U_c^2/2) \\ &= -2 \frac{\partial \phi}{\partial t} + 2 \bar{V} \cdot (\bar{V}_A + \bar{\Omega} \times \bar{r}) - V^2 \end{aligned} \tag{3.8}$$

Equation 3.8 is used to calculate the loads.

To obtain the surface velocity, one must impose the no-penetration boundary condition, a trailing-edge condition, and the requirement that

the circulation around both airfoil and wake remain constant. These are discussed next.

For the moving airfoil the no-penetration boundary condition takes the form

$$(\bar{V} - \bar{V}_s) \cdot \bar{n} = 0 \tag{3.9}$$

everywhere on the surface of the airfoil, where V_s is the absolute velocity of a point in the surface of the airfoil, V is the velocity of the fluid particle in contact with that point, and n is a vector normal to the surface at that point. If the airfoil is considered a rigid body, then V_s is given by an expression of the form

$$\bar{V}_s = \bar{V}_A + \bar{\Omega} \times \bar{r}_s \tag{3.10}$$

where r_s is the relative position of the point in the surface. In general, the velocity of a fluid particle can be expressed as

$$\bar{V} = \bar{V}_B + \bar{V}_W \tag{3.11}$$

where V_B is the velocity induced by the vorticity on the surface and V_W is the velocity induced by the vorticity in the wake (For flows that appear steady in the moving frame, $V_W = 0.$). Using Equations 3.10 and 3.11, one can re-write Equation 3.9 as

$$\bar{V}_B \cdot \bar{n} = (\bar{V}_A + \bar{\Omega} \times \bar{r}_s - \bar{V}_W) \cdot \bar{n} \tag{3.12}$$

We require the pressures along the upper and lower surfaces to approach the same value at the trailing edge. This idea, of course, is common to all models of lifting flows. In establishing the statement of this requirement suitable for the present numerical scheme, we follow a procedure similar to the one developed by Basu and Hancock[1978]. They referred to unpublished correspondence with E.C.Maskell, and they noted that earlier Giesing[1968] had arrived at essentially the same conclusions. Recent experimental studies by Telionis and Poling[1984] seem to support the conclusions. The ideas are discussed next.

In the potential-flow model of the actual flow, we assume that the streamlines along the upper and lower surfaces, when viewed in the moving reference frame, always merge at the trailing edge where separation occurs. One must consider what is happening along each streamline. If the trailing edge is not a cusp, then the situation there can be described by one of the following:

(i) Both merging streamlines have a sharp bend, and the streamline emanating from the trailing edge passes outside the wedge formed by the two tangents, as shown in Figure 2a. If this happens, the speed along one of the merging streamlines (the bottom line in Figure 2a) is infinite, while the speed along the other is zero at the trailing edge.

(ii) Only one merging streamline has a sharp bend, the other is smooth, and the streamline emanating from the trailing edge is tangent to one side of the wedge, as shown in Figure 2b. If this happens, the speed is zero on the bent streamline and non-zero, but finite, on the other at the trailing edge.

(iii) Both merging streamlines have a sharp bend, and the streamline emanating from the trailing edge remains inside the wedge, as shown in Figure 2c. If this happens, the speed is zero on both streamlines at the the trailing edge.

To see the impliciations of these possibilities, we apply Bernoulli's equation along the upper and lower surfaces. It follows from Equation 3.8 that

$$C_{P\ell} - C_{Pu} = 2\frac{\partial}{\partial t}(\phi_u - \phi_\ell) + V_u^2 - V_\ell^2 + 2(\bar{V}_\ell - \bar{V}_u)\cdot(\bar{V}_A + \bar{\Omega} \times \bar{r}) \tag{3.13}$$

where the subscripts ℓ and u denote the lower and upper surfaces. The requirement that $C_{p\ell} = C_{pu}$ leads to

$$2\frac{\partial \Gamma}{\partial t} = V_\ell^2 - V_u^2 + 2(\bar{V}_u - \bar{V}_\ell)\cdot(\bar{V}_A + \bar{\Omega} \times \bar{r}) \tag{3.14}$$

where Γ is the circulation around the airfoil. For circulation around both airfoil and wake to remain constant, the rate of change of the circulation around the wake must be the negative of that given by Equation 3.14.

Had the problem been posed in a fixed reference frame, Equation 3.14 would have been replaced by

$$2\frac{\partial \Gamma}{\partial t} = V_\ell^2 - V_u^2 \tag{3.15}$$

Equation 3.15 was given by Basu and Hancock as well as Telionis and Poling. Prandtl and Tietjens[1957] gave the right-hand side of Equation 3.15 as the expression for the addition of vorticity to the wake.

For case (i), $V_u = 0$ and $V_\ell = \infty$; hence, Equation 3.14 suggests that the rate of production of circulation is infinite. For case (ii), $V_u = 0$ and V_ℓ = a nonzero, finite value; hence, Equation 3.14 suggests that the rate of production of circulation is nonzero, but finite. For case (iii), $V_u = V_\ell = 0$; hence, Equation 3.14 suggests that the rate of production of circulation is zero, Γ is constant.

The first case can be used to simulate the situation at the instant of an impulsive start. After the sudden start and while conditions are unsteady, the situation is modelled by the second case. The steady state is modelled by the third case.

There is no inconsistency with the speed on the upper-surface streamline differing from the speed on the lower-surface streamline at, and downstream of, the point of merger. This is the potential-flow imitation of the wake. There is no discontinuity in the pressure across the wake if the vorticity is convected at the local particle velocity (e.g., Karamcheti[1980]).

In the case of a trailing-edge cusp, the streamlines have a sharp bend at the trailing edge when the rate of change of circulation is infinite, and are tangent to the trailing-edge otherwise. When the rate of change of circulation is nonzero, but finite, the speeds on the upper and lower surfaces approach different values. When the rate of change is zero, the speeds approach the same value.

3.3 PRESENT NUMERICAL SCHEME

The surface of the airfoil is approximated by a series of short straight segments as shown in Figure 3. The ends of the segments, which are called nodes, lie on the surface of the airfoil. The surface velocity is approximated by a continuous function that varies linearly between the nodes.

For steady flows, it has been found that the use of a piecewise constant, discontinuous distribution of vorticity (or equivalently surface velocity) can lead to inaccuracies such as oscillating values of the vorticity on successive panels. Anderson[1984] discussed some of these problems. The same problems occur in unsteady flows. The use of a linearly varying, continuous distribution of vorticity eliminates these problems.

The main building blocks of the present method are the formulas for the velocity fields induced by a linearly varying vortex sheet and a point vortex. Referring to Figure 4, we can write the velocity components at a point(x,y) as follows:

$$\text{(Case 1)} \quad \begin{aligned} V_x &= (1 - \frac{x}{\ell})\Delta\theta - \frac{y}{\ell}\,\ell n(R) \\ V_y &= (1 - \frac{x}{\ell})\ell n(R) + \frac{y}{\ell}\Delta\theta - 1 \end{aligned} \tag{3.16}$$

$$\text{(Case 2)} \quad \begin{aligned} V_x &= \frac{x}{\ell}\Delta\theta + \frac{y}{\ell}\ell n(R) \\ V_y &= \frac{x}{\ell}\ell n(R) - \frac{y}{\ell}\Delta\theta + 1 \end{aligned} \tag{3.17}$$

where

$$\Delta\theta = \tan^{-1}[(1 - \frac{x}{\ell})/(\frac{y}{\ell})] - \tan^{-1}[-\frac{x}{y}]$$

and

$$R = \{\frac{(\ell-x)^2 + y^2}{x^2 + y^2}\}^{1/2} \tag{3.18}$$

For the vortex core having the clockwise circulation 2π, the velocity field is

$$V_x = \frac{y}{x^2 + y^2} \qquad \text{and} \qquad V_y = \frac{-x}{x^2 + y^2} \tag{3.19}$$

Next the procedure for general unsteady flows is described. It follows from Equation 3.14 and the requirement of constant circulation around both airfoil and wake that, during a small time interval Δt, a vortex having approximately the circulation

$$\Delta\Gamma_W = -\frac{1}{2}\{V_\ell^2 - V_u^2 + 2(\bar{V}_u - \bar{V}_\ell)\cdot(\bar{V}_A + \bar{\Omega} \times \bar{r})\}\Delta t \tag{3.20}$$

is added to the wake. With the present method this vortex is modelled as a discrete point, or core. One is formed at each time step. These cores are convected away from the trailing edge of the airfoil at the local particle velocity and constitute the wake. Instead of using Equation 3.20 directly, the present method imitates conditions at the trailing edge by setting both V_u and V_ℓ equal to zero and placing a core of unknown strength there.

The values of V_u and V_ℓ are consistent with the requirement for steady flow around airfoils of non-zero trailing-edge angle. As the numerical examples in the next section show, this is also the proper choice for airfoils with a trailing-edge cusp.

In a recent study, Duffy, Czajkowski, and Jaran[1984], who considered a sinusoidally oscillating flat plate, arrived at a result equivalent to Equation 3.20. They used a finite-element representation of the plate, which is essentially a two-dimensional version of the vortex-lattice method. They represented the wake with discrete vortex cores, as we do, but they did not convect these cores at the local particle velocity. Instead, they moved the cores at the velocity of the undisturbed free stream. As a result, their wakes are always flat and parallel to the free stream.

The no-penetration boundary condition, Equation 3.12, is only imposed at discrete times and discrete points. There is one point in each element, called the control point, where this condition is enforced. It lies on the straight segment midway between the nodes. The normal to the surface is approximated by the perpendicular to the straight segment.

Using Equations 3.16 - 3.19, one can develop an influence matrix and replace Equation 3.12 with the following:

$$\sum_{j=1}^{N} A_{ij}\,\gamma_j + T_i\Gamma_{TE} = (\bar{V}_A + \bar{\Omega} \times \bar{r}_i - \bar{V}_{Wi}) \cdot \bar{n}_i \qquad (3.21)$$

for i = 1,2, - - - ,N-1. There are N nodes and N-1 segments. A_{ij} is the normal component of the velocity at the control point of element i induced by unit surface velocity at node j, and γ_j is the unknown value of the

surface speed at node j. T_i is the normal component of velocity induced by a discrete vortex core of unit circulation at the trailing edge, and Γ_{TE} is the unknown circulation around the core at the trailing edge. V_{Wi} is the velocity induced by all the cores in the wake except the one at the trailing-edge. n_i is the unit vector perpendicular to the surface of element i.

In addition to Equation 3.21, there is the condition at the trailing edge

$$\gamma_1(\text{or } V_\ell) = \gamma_N(\text{or } V_u) = 0 \tag{3.22}$$

and the condition of constant circulation around airfoil and wake

$$\int_c \bar{V} \cdot d\bar{r} + \sum_{i=1}^{M} \Gamma_i = 0 \tag{3.23}$$

where c is a path around the airfoil through the trailing edge and Γ_i are the circulations around the M cores making up the wake. The integral is evaluated explicitly on the basis of a linear distribution of vorticity (or surface speed).

Equations 3.21 - 3.23 form a system of N + 2 equations for N + 1 unknowns (the γ_i and Γ_{TE}). Hence, we obtain the unknowns by an optimization technique (see Appendix B). Specifically, we minimize the sum of the squares of the errors of Equation 3.21 subject to the three equality constraints given by Equations 3.22 - 3.23.

After the unknowns have been obtained, the wake is convected. Then the unknowns are obtained again. This procedure can be repeated indefi-

nitely. All one needs to start the procedure is a set of initial conditions (i.e., positions and circulations for the cores in the wake).

To convect all the cores in the wake except the one at the trailing edge, we use

$$\bar{r}(t + \Delta t) = \bar{r}(t) + \bar{V}\,[\bar{r}(t)]\Delta t \tag{3.24}$$

Initially, for the core at the trailing edge, we used

$$\bar{r}(t + \Delta t) = \bar{r}(t) + \bar{V}\,[\bar{r}(t + \Delta t)]\Delta t \tag{3.25}$$

Here V[r(t)] denotes the velocity at the position r(t). Equation 3.25 is satisfied by iteration; it was used to avoid calculating the velocity at the trailing edge. However, a comparison of the results from both Equations 3.24 and 3.25 to convect the core at the trailing edge showed little difference and hence Equation 3.24 is used in the following.

In earlier treatments, Giesing[1968] and Basu and Hancock[1978] solved for the strengths of the sources and vorticity, instead of solving for the surface velocity at the nodes, as one does with the present method. Then they calculated the surface velocity at the control points.

Giesing used a predictor-corrector scheme to convect the cores in the wake. For the small step sizes used here, we found very little difference between the results obtained by the two procedures. All the results presented here are based on Equations 3.24 and 3.25.

Equation 3.19 is used to calcualte the velocity field generated by the wake. These expressions have an algebraic singularity; hence, fol-

lowing the usual practice, we introduce a cutoff length. Whenever the distance between the field point and the core is less than the cutoff length, the contribution of that core is ignored. For all the present calculations the cutoff length is twice the chord devided by the number of elements. Numerical experimentation has shown that the results depend upon the cutoff length, but there is a range of cutoff for which the results are very nearly constant. The present choice lies in this range.

3.4 NUMERICAL EXAMPLES

3.4.1 STEADY FLOWS

The dual purpose of considering steady flows is to establish the trailing-edge condition, for both cusp and nonzero wedge angle, and to demonstrate the accuracy of the present scheme. For steady flow, $V_W = 0$, $\Omega = 0$ and $V_A = u$, a unit vector of constant direction. We consider Karman-Trefftz airfoils defined by

$$z = z_T\{(\zeta + \zeta_T)^n + (\zeta - \zeta_T)^n\}/\{(\zeta + \zeta_T)^n - (\zeta - \zeta_T)^n\} \qquad (3.26)$$

Equation 3.26 transforms a unit circle in the ζ-plane onto an airfoil in the z-plane. z_T is the point at the trailing edge of the airfoil and ζ_T is its image. Some discussion of these airfoils can be found in Karamcheti. The trailing-edge angle is related to the exponent n according to

$$\beta = (2 - n)\pi \tag{3.27}$$

The special case of n = 2 yields a Joukowski airfoil, which has a cusp at the trailing edge.

For steady flows, Equation 3.21 is modified by setting Γ_{TE} and V_{wi} equal to zero, and Equation 3.23 is dropped. We consider two possibilities for treating the trailing edge: (1) $V_u + V_\ell = 0$ and (2) Equation 3.22. For the former, we can eliminate one unknown and use Equation 3.21, directly; the number of unknowns is the same as the number of equations. For the latter, we can eliminate two unknowns; the number of equations is one more than the number of unknowns, and we use an optimization scheme. Either condition is the equivalent of the so-called Kutta condition and leads to a unique value of the circulation around the airfoil.

Raj and Gray set $V_\ell = V_u = 0$, but then, instead of using an optimization scheme, they simply ignored one of the control points. Such a scheme is also described by Anderson[1984]. This scheme raises the question of which control point to ignore. The results can vary considerably, depending on the choice. The present scheme eliminates the need to make such a choice, though one can arbitrarily weight the squares of the normal components at the control points and hence introduce some arbitrariness. In all the present results, the weighting is uniform.

The results for the first way of treating the trailing edge are given in Tables 3-1 and 3-2. In Table 3-1 the value of n in Equation 3.27 is 1.95. For a small number of elements, the results are encouraging. But clearly as the number of elements increases, the trend is wrong; V_u and

V_ℓ change sign and are inconsistent with physical demands. The situation is worse when n = 2, as the results in Table 3-2 show. For a non-cusp trailing edge, the values of V_u and V_ℓ should be zero. For a cusp trailing edge these values are not expected to be zero, but here the signs of V_u and V_ℓ are inconsistent with the requirement of smooth flow from the trailing edge and there clealy is no indication of convergence.

The problem stems from the fact that the elements near the trailing edge become more nearly coincident as the number of elements increases, and the results become vulnerable to round-off error. As a consequence, the trailing edge is better modelled as a single element that merges the vortex sheets on the upper and lower surfaces and has zero combined vorticity at the trailing edge. Without any modifications to accomodate the cusp and without experiencing any numerical problems, the second way of treating the trailing edge, which sets $V_u = V_\ell = 0$ and uses optimization, can in effect accomplish the merger.

In Tables 3-3 and 3-4, numerical results obtained by the second way of treating the trailing edge and the exact solution for n = 1.95 and n = 2 are given. The results indicate that the numerical solution converges to the exact solution as the number of elements increases. For the cusp the present results and the exact solution are in close agreement everywhere except at the trailing edge. These results suggest that the present scheme is capable of producing a very accurate approximation to the solution of potential-flow problem. The second way of treating the trailing edge is used for the remainder of the examples. The lift is accurately predicted by both methods because the effect of the irregularity at the trailing edge cancels. Using a total of only eight elements to model both

the upper and lower surfaces, the present procedure predicts the lift to within five percent.

As a second example, we consider an NACA 23012 airfoil at various angles of attack. The experimental pressure measurements are compared with the predictions of the present method in Figure 5. The agreement is generally quite good; however, in part (e) the data suggest the presence of a separation bubble, which is not modelled by the present approach. In Figure 6 experimental and numerical results are shown for the same airfoil in the presence of an external airfoil flap. Here Equation 3.22 is imposed at both trailing edges. There is interaction between the two airfoils. The no-penetration condition on each airfoil simultaneously accounts for the disturbance created by both. Again the agreement is quite good. This suggests that the present method correctly captures the aerodynamic interference.

3.4.2 UNSTEADY FLOWS

The time-dependent loads are obtained by integrating the pressure over the surface. The velocity potential ϕ is obtained by numerically evaluating a line integral. Several different paths from the same starting point and several different starting points were used to check the results. A finite-difference formula is used to obtain the derivative of ϕ with respect to time. In Table 3-5 the potentials at two adjacent nodes on an airfoil computed by numerical integration (Gauss-Legendre formula) are compared with the theoretical values for the steady case. In the computation, the position of infinity is chosen as ten chord

lengths from the point on the airfoil perpendicular to the motion of the airfoil (see Figure 7). This choice is based on the fact that the computed velocity at the position of infinity is different by less than one percent of the characteristic speed. Convergence is shown clearly with the number of elements. For the unsteady case, the circulation around the airfoil and cores in the wake for the impulsively started airfoil was computed by a line integral and the result was found to be nearly zero.

In the first example, a symmetric Karman-Trefftz airfoil is advancing at a constant speed while executing a sinusoidal heaving motion. The angle θ is always zero and

$$Y_A(t) = 0.018 \sin \omega t \tag{3.28}$$

These conditons imitate the experiment of Bratt[1953]. For Figure 8, $\omega = 4.3$, which is the smaller of the two reduced frequencies considered by Bratt. 20, 40, and 80 elements are used in Figure 8a, b, and c, respectively. As the number of elements increases, the time step correspondingly decreases and the cores in the wake become more densely packed. The time step is chosen to be approximately the length of time required for a fluid particle, moving at the characteristic speed, to travel the length of the element on the lower surface at the trailing-edge. There appears to be convergence. In part c, the discrete cores in the wake are so densely packed that near the trailing edge the graphical representation resembles a continuous line. Similar results are shown in Figure 9 for $\omega = 17$, the larger of the two frequencies considered in the experiment. The results in both figures are in good qualitative agreement with the

smoke visualization of the flow by Bratt[1953], the numerical results obtained earlier by Giesing[1968], and the semi-analytical results of Katz and Weihs[1978] for a flat plate.

Attempts to model the wake with continuous elements of vorticity were generally unsuccessful and certainly not robust, as the present approach is. Figures 8 and 9 clearly show the problem: continuous elements are not able to produce the clustering shown in these figures. From the experiment it appears that vorticity does concentrate, and hence this clustering of discrete vortex cores is likely an accurate imitation of the actual flow.

There are many closely packed cores in the wake so that the velocity field they generate is quite smooth very near the wake. Consequently, the predicted effect of the wake on the wing is most likely accurate. One would expect the accuracy to be poorest near the trailing edge.

In Figure 10 the lift, moment, drag, circulation, and position are shown as functions of time for the lower of the two frequencies. These results show that the loads are not in phase with each other or the motion. It is interesting to see that the mean value of the drag is negative, indicating that the pumping action of the airfoil produces a small thrust. The loads and circulation converge rapidly as the number of elements increases. In Figure 11, lift, moment, drag and circulation are plotted as functions of position in the y-direction for the same frequency. Hysteresis is clearly evident.

In the second example, a symmetric Karman-Trefftz airfoil is impulsively started and then moved forward at constant velocity and fixed angle θ. In Figure 12 the streamlines and positions of cores in the wake

are shown. In Figure 12a, the motion has just started, and the wake consists of only one vortex core at the trailing edge. The situation after many time steps is shown in Figure 12b. The results in Figure 12 closely resemble the figures in the texts by Karamcheti[1980] and Prandtl and Tietjens[1957]. Further numerical experiments showed that the results converged rapidly as the number of elements increased.

In Figure 13, the lift, moment, drag, and circulation are shown as functions of the distance travelled. The zero position corresponds to the instant the first core forms at the trailing edge; hence circulation is not zero there. It is interesting to note the large initial values of the loads. The small wiggles near the position where minimum lift occurs are most likely a numerical aberration caused by the use of discrete cores. The drag decreases monotonically, but the lift and pitching moment about the nose of the airfoil first decrease rapidly and then grow slowly. The minimum value of lift and moment occur when the airfoil has travelled approximately one tenth chord. Graham[1983] predicted similar behavior for the lift. The present results for lift are compared with those of Basu and Hancock[1978], Giesing[1968], and Wagner[1925] in Figure 14a. Only the present results predict the large initial loads. Shortly after the start, all are in close agreement in spite of the fact that Wagner's results are for a flat plate and the others are for thick airfoils. In Figure 14b, the present results for drag are compared with those of Basu and Hancock. The reason for the difference is not known.

In Figure 15, the present results are compared with the experimental data of Walker (Walker's data can be found in the text by Goldstein[1965]) and the analytical results of Wagner for a flat plate. In the experiment,

a symmetric R.A.F. 30 airfoil was placed in a long towing tank. The airfoil was started suddenly in an attempt to create an impulsive start and then moved at constant speed. The angle of attack was 7.5 degrees. Oil drops that were suspended in the water and illuminated by a bright light were photographed. Exposures of known, short duration yielded the velocity field. The circulation was obtained by evaluation of a line integral around the airfoil. The present results are for a symmetric Karman-Trefftz airfoil having the same thickness as the R.A.F. 30.

In Figure 16, the effect of thickness is shown to retard the build-up of lift and circulation. In Figure 17, the effect of angle of attack is shown to produce a similar effect. The distortion of the curve for higher angles of attack shortly after the motion starts is due to the nonlinear effect of the wake deformations. It is interesting to see the two curves in part (b) cross each other once shortly after the motion starts. The reason is not known.

The final example is an impulsively started airfoil with flap. These are the same airfoil and flap used in the static examples. For the purpose of illustrating the nature of this problem, we suppose that the number of nodes on the main airfoil is the same as that on the flaps, N nodes and N - 1 elements. Equation 3.21 forms a system of 2N - 2 equations; the trailing-edge constraints, Equation 3.22, yield four additional equations; and the requirement that the circulations around both airfoils and their wakes remain constant gives two more. There is a total of 2N + 4 equations and 2N + 2 unknowns (the γ_i on both and Γ_{TE} for both). Again the optimization scheme is used, the trailing-edge condition and the requirement of constant circulation being treated as constraints.

In Figure 18 the development of the wake with time is shown. The vorticity from the airfoil is drawn down very near the surface of the flap, and the two wakes appear to merge at the trailing edge of the flap. In Figure 19, the computed steamlines are shown at the instant the first cores form at the trailing edges and in the steady state. Figure 19b corresponds to the numerical data in Figure 6.

IV. THREE-DIMENSIONAL NONLIFTING PROBLEM

4.1 GENERAL

In the past two decades, various extensions of the panel methods that utilize a distribution of singularities over the body surfaces have been developed, and the number of flow situations that can be handled has continually increased.

Here we are concerned with flows past arbitrary three dimensional nonlifting bodies. We develop two numerical methods based on triangular elements whose three nodes lie exactly on the actual body surface. The use of flat triangular elements eliminates the need to transfer the evaluation of velocity from the actual to an approximating surface as well as the openings between elements which cause some divergence problems in many doublet panel methods. One method utilizes a linear source distribution over a curved element while the other uses a linear vorticity distribution over a flat element.

The source panel method based on a flat element is a special case of the method based on a curved element and is readily obtained from the latter. The source panel method based on curved elements is developed in a way similar to the advanced panel-type method by Johnson and Rubbert[1975]. There are some major differences, though, such as the way the approximating surface and the shape of panel are determined.

In order to eliminate the openings between elements, the vorticity panel method is developed based on the flat elements. Some ways to

eliminate two major difficulties arising from the discretization of the surface of the body are discussed in the following.

Yen, Mook, and Nayfeh[1980] used the Lagrange multiplier method to treat the equations from the conservation conditions. The additional constraint equations from the conservation conditions can create a storage problem as well as render the influence matrix ill-posed. Since the number of additional equations is the same as the number of equations from the boundary conditions, the storage problem may be serious, especially for three-dimensional problems. Moreover the conservation matrix has all zero entries except those which correspond to the global node numbers of the particular elements. In addition, depending on the discretization scheme of the surface of the body, all the constraint equations are not independent. This produces a singular matrix when one uses the Lagrange multiplier method. There seems to be no systematic way of finding the dependent equations and eliminating them. The least-squares optimization scheme for both the influence matrix and the conservation matrix resolves both problems: the storage problem and the problem of an ill-conditioned matrix.

Because of the tangency condition, the vorticity must be tangent to the surface of the body. This condition cannot be satisfied over the discretized surface of the body because the slope of the surface is not continuous along the edges of elements. This implies that the vorticity along the edges of elements loses continuity on assembly. This problem is overcome by introducing a scheme of rotation. The vorticity lying on an element rotates onto the plane of the neighboring element as soon as

it crosses the border while keeping its magnitude. In this sense the tangency condition is satisfied all over the surface.

In this chapter, two panel methods are developed and their computed results about various bodies are compared.

4.2 DESCRIPTION OF THE METHOD

The surface of the body is divided into a finite number of triangular elements (see Figure 20(a)). Using triangular elements, we ensure that the three nodes of the element lie on the surface exactly. Surface singularity functions are approximated by linear functions. Introducing the local coordinates (Figure 20(b)), we then express the approximating function over an triangular element in terms of linear interpolation functions and nodal values. In the following we develop two methods: a piecewise continuous (linear) source panel method and a piecewise continuous (linear) vorticity panel method.

4.2.1 SOURCE FORMULATION

In Chapter 2, the boundary-integral formula for velocity was obtained as follows:

$$\bar{V}(x,y,z) = \frac{1}{4\pi} \nabla_P \left[\int_\sigma \int \frac{S(\xi,\eta,\zeta)d\sigma(\xi,\eta,\zeta)}{r} \right] \qquad (4.1)$$

Using this formula, we seek the velocity induced by an element. First, the real curved surface is approximated by a paraboloidal surface defined as follows:

$$\varepsilon D_0 - \zeta = \varepsilon\{(\xi - A_0)^2 + k(\eta - B_0)^2\} \tag{4.2}$$

where ε, k, A_0, B_0 and D_0 are parameters to be determined. We determine them by forcing the simulated surface to fit the real surface best in the least-squares sense under the assumption of weakly nonlinear geometry. Note that the special case of a flat element is obtained by setting $\varepsilon = 0$ in Equation 4.2. The details are given in Appendix D.

The linear source distribution over an element is approximated and expressed in terms of linear interpolation functions and nodal values of sources in the following way:

$$S(\xi,\eta,\zeta) = \sum_{i}^{3} S_i \psi_i \tag{4.3}$$

where ψ_i is the linear interpolation function at the i-th node of a triangular element and S_i is the nodal value of source strength (see Reddy[1984]). Substituting Equations 4.2 and 4.3 into Equation 4.1 and carrying out the integration under the assumption of weakly nonlinear geometry, we obtain explicit expressions for the potential and the velocity components. For the details of this development, see Appendix E. Then, the velocity potential can be expressed as:

$$\phi = \sum_{i}^{3} S_i(a_i\phi_1 + b_i\phi_2 + c_i\phi_3) \equiv \sum_{i}^{3} S_i\bar{\phi}_i \tag{4.4}$$

The a_i, b_i and c_i are the coefficients of interpolation functions. ϕ_1, ϕ_2 and ϕ_3 represent the potential for constant source strength, the potential for linear source distribution in the x-direction and the potential for linear source distribution in the y-direction respectively. The velocity is then obtained by taking the gradient of the potential and dropping the summation notations:

$$
\begin{aligned}
V_x &= S_i(a_i \partial\phi_1/\partial x + b_i \partial\phi_2/\partial x + c_i \partial\phi_3/\partial x) \equiv S_i \partial\Phi_i/\partial x \\
V_y &= S_i(a_i \partial\phi_1/\partial y + b_i \partial\phi_2/\partial y + c_i \partial\phi_3/\partial y) \equiv S_i \partial\Phi_i/\partial y \\
V_z &= S_i(a_i \partial\phi_1/\partial z + b_i \partial\phi_2/\partial z + c_i \partial\phi_3/\partial z) \equiv S_i \partial\Phi_i/\partial z
\end{aligned}
\qquad (4.5)
$$

These are the required equations. The velocity induced by an element at its own control point is calculated by taking the limit of these formulas.

The evaluation of the formulas in Equation 4.5 is quite time-consuming. The complicated nature of these formulas stems from the fact that they account for the effects of all the details of the geometry. It is not difficult to imagine that if a field point under consideration is far from the element, the details of the geometry are not important and the potential and velocity at that point depend mainly on certain overall parameters. It is natural to consider an approximation by means of a multipole expansion. For the far-field velocity formulas, Appendix F may be consulted.

4.2.2 VORTICITY FORMULATION

We begin with the velocity formula developed in Chapter 2.

$$\bar{V}(x,y,z) = \frac{1}{4\pi} \mathrm{curl}_P \int_\sigma \int \frac{\bar{\Omega}(\xi,\eta,\zeta)d\sigma(\xi,\eta,\zeta)}{r} \tag{4.6}$$

The vorticity is approximated by linear interpolation functions over a flat element as follows:

$$\bar{T}(\xi,\eta,\zeta) = (T_{kx}\bar{i} + T_{ky}\bar{j})\psi_k \tag{4.7}$$

where T is the vorticity lying on the surface of an element and T_{kx} and T_{ky} are the vorticity components at elementary node k.

From the Figure 21, it is evident that vorticity tangent to one element cannot also be tangent to a neighboring element unless they are coplanar. The tangency condition of vorticity at a point on the surface is determined by the normal unit vector at that point (see Appendix A).

Here we introduce two normal unit vectors, a global normal unit vector and a local normal unit vector. The former is a unit vector normal to the body surface and is obtained by taking the average of the normal unit vectors of all the elements that share the point where the normal unit vector is evaluated. The local normal unit vector is a unit vector normal to an element where the point lies.

From the definition of two normal unit vectors, it is clear that, in general, two vectors are the same except when these stand on the edges of elements. In other words, there exist two normal unit vectors on the

edges of elements and they are used separately depending on the viewpoints, either global or local viewpoint.

The difference between two normal unit vectors along the edges of elements causes the discontinuity of the unknown vorticity vector there. In order to eliminate this problem of discontinuity of vorticity, a unique scheme is developed to rotate the vorticity vector across the edges of elements. In other words, the vorticity tangent to an element rotates and becomes tangent to another element as soon as it crosses the border of the two elements. This means that a vorticity vector at a point on the border can be viewed differently depending upon the element under consideration. In this way, the continuity of vorticity is satisfied. Since the unknown vorticities are located at nodes(i.e., border of elements), the nodal vorticities must be rotated on assembly. Thus, the relationship between unrotated and rotated vorticities at a node must be known.

In the following the relationship between two vectors will be derived in the local coordinates (see Figure 22). We begin with the tangency condition. This condition states that the vorticity vector must be tangent to the surface and is expressed as follows:

Vorticity vector

$$\bar{N} \cdot \bar{\omega} = 0$$

or

$$N_x\omega_x + N_y\omega_y + N_z\omega_z = 0 \tag{4.8}$$

where N and ω are a normal unit vector and a vorticity vector, respectively. Here, we note that only two components are independent among the

three of the vorticity vector. Therefore, the z-component of the vorticity can be expressed in terms of the other two components as:

$$\omega_z = - (N_x\omega_x + N_y\omega_y)/N_z \tag{4.9}$$

where N_z is not equal to zero.

As a first condition of continuity, the magnitude of the vorticity should be preserved.

$$T_x^2 + T_y^2 = \omega_x^2 + \omega_y^2 + \omega_z^2 \tag{4.10}$$

In addition the rotated vorticity should lie on the Nω-plane to retain its sense on the surface.

$$\bar{N} \times \bar{T} = c\, \bar{N} \times \bar{\omega}$$

or

$$T_x = c(\omega_x - N_x\omega_z/N_z) \quad \text{and} \quad T_y = c(\omega_y - N_y\omega_z/N_z) \tag{4.11}$$

where the c is a scaler factor to be determined. From Equations 4.10 and 4.11 with Equation 4.8, it follows that

$$c = \omega \,/\, \sqrt{\omega^2 + (\omega_z/N_z)^2} \tag{4.12}$$

where ω is the magnitude of the vorticity. Substituting Equation 4.9 into Equation 4.11 yields the components of the rotated vorticity expressed in terms of two components of unrotated vorticity as:

$$T_x = c(A_{11}\omega_x + A_{12}\omega_y) \quad \text{and} \quad T_y = c(A_{21}\omega_x + A_{22}\omega_y) \tag{4.13}$$

where

$$A_{11} = 1 + (N_x/N_z)^2$$

$$A_{12} = N_x N_y / N_z^2 = A_{21}$$

and

$$A_{22} = 1 + (N_y/N_z)^2$$

Substituting Equation 4.7 into Equation 4.6 and carrying out the integral, we obtain the velocity formula in terms of the rotated vorticity vector in the local coordinates.

$$\bar{V} = - T_{ky}\partial\Phi_k/\partial z\ \bar{i} + T_{kx}\partial\Phi_k/\partial z\ \bar{j} + (T_{ky}\partial\Phi_k/\partial x - T_{kx}\partial\Phi_k/\partial y)\ \bar{k} \tag{4.14}$$

where the i, j and k are orthogonal unit vectors in x, y and z-directions, respectively. For details of the development of the velocity formula, the reader may refer to the underlined parts in Appendix E. Substituting Equation 4.13 into Equation 4.14 , we can express the velocity in terms of the global vorticity components as:

$$V_x = - c\ (A_{k21}\omega_{kx} + A_{k22}\omega_{ky})\partial\Phi_k/\partial z$$

$$V_y = \quad c\ (A_{k11}\omega_{kx} + A_{k12}\omega_{ky})\partial\Phi_k/\partial z \tag{4.15}$$

$$V_z = c\{(A_{k21}\omega_{kx} + A_{k22}\omega_{ky})\partial\Phi_k/\partial x - (A_{k11}\omega_{kx} + A_{k12}\omega_{ky})\partial\Phi_k/\partial y\}$$

where c is known from Equation 4.12. These are the required equations for the vorticity panel method. The velocity formula in Equation 4.15

can be transformed to the global coordinates. After transformation, the tangency condition should be used again because there appear again all three components of the voticity. Note that the tangency condition in the global coordinates must be used case by case depending upon the magnitude of the components of the global normal unit vector at the node.

Since the vorticity, ω, is approximated by a linear function the divergenceless field of vorticity will be violated unless we force the approximated vorticity to satisfy the condition. This will produce as many subsidiary conditions as the number of elements on the surface.

$$0 \equiv \text{div } \bar{T} = (\partial\psi_k/\partial x)T_{kx} + (\partial\psi_k/\partial y)T_{ky}$$
$$= c\,[(A_{11}b_k + A_{21}c_k)\omega_{kx} + (A_{12}b_k + A_{22}c_k)\omega_{ky}] \qquad (4.16)$$

We refer to this equation as the conservation equation. Again the divergenceless conditions can be transformed to the global coordinates on assembly.

4.2.3 BOUNDARY CONDITIONS

The boundary conditions are satisfied at only a finite number of control points (centroid of each element). By applying the no-penetration conditions at each control point on assembly, one can develop the influence matrix in the following form:

$$P_{ij}\, x_j = Q_i \qquad (4.17)$$

for i = 1,2, --- ,NEM (number of elements) and j = 1,2, --- ,NN (number of nodes) for source formulation or j = 1,2, --- ,NN2 (twice the number of nodes) for vorticity formulation. x_j represents the unknown singularity strength at j-th node.

For the vorticity formulation, the divergenceless condition over each element gives the conservation matrix.

$$C_{ij}\, x_j = 0 \tag{4.18}$$

for i = 1,2, --- ,NEM and j = 1,2, --- , NN2. This matrix has only a few non-zero entries for each index i. Moreover not all these equations may be independent.

The system is over-determined in the source formulation and under-determined with subsidiary conditions in the vorticity formulation. In order to solve these systems, we introduce a least squares method (see Appendix B). In both formulations, we optimize the errors in the no-penetration boundary condition. In addition, the conservation condition in the vorticity formulation is handled either by using the Lagrange multiplier method or by including this in the least squares optimization. In this thesis, we use the least squares method for both conditions unless otherwise mentioned. This scheme actually serves two purposes; it uses much less storage than the Lagrange multiplier method and it eliminates the possibility of the ill-conditioned matrix that may occur from dependence of some constraint equations. This dependence of some constraint equations on each other is almost impossible to find in general. We further reduce the storage need by introducing another scheme, which

constructs the optimized influence matrix without constructing the intermediate matrices; the influence matrix and the conservation matrix.

Once the optimized influence matrix is obtained, the unknowns are readily obtained by any standard procedure. But the procedure of rotating the vorticity at the nodes on the surface renders the problem nonlinear in the vorticity formulation. Thus the problem is solved iteratively in this case starting with initial guesses. The obvious initial guess for the factor c in Equation 4.12 is unity.

4.2.4 CALCULATION OF LOADS

For the source formulation, the velocity at a point in the flow field is calculated by using the velocity formula with known source distributions. For the vorticity formulation, the surface velocity is directly related to the surface vorticity by the following relationship (see Karamcheti):

$$\Delta\bar{V} \equiv \bar{V}_T - \bar{V}_B = \bar{\Omega} \times \bar{n} \tag{4.19}$$

where V_T and V_B are velocities on the upper and lower surfaces of the vortex sheet, respectively. Note that the velocity of the lower surface is zero if the lower surface belongs to a thick body. Therefore the surface velocity has the same magnitude as the surface vorticity and is perpendicular to the surface vorticity.

The pressure distributions on the surface of the body are readily obtained from Bernoulli's equation. The nondimensionalized pressure, (i.e., the pressure coefficient) is defined as:

$$C_p \equiv (P - P_\infty)/(\rho V_r^2/2) = (1 - V^2/V_r^2) \tag{4.20}$$

where the reference velocity is the velocity of the body under consideration. The forces and moments acting on the body are obtained by integrating the known pressure distributions if necessary.

4.3 NUMERICAL RESULTS

In order to determine the accuracy of the present methods, the surface velocity distributions for various body shapes are calculated. The numerical results then are compared with exact analytic solutions as well as the numerical results obtained by others.

In addition, the effect of the geometric nonlinearity is examined by comparing the results with and without the geometric nonlinearity for the source formulation. The geometric nonlinearity is eliminated by letting ε in Equation 4.2 equal zero.

In Figure 23, we show two typical discretized surfaces of axi-symmetric bodies: a sphere and an oblate spheroid. In Table 4-1, the numerical results obtained from the present methods are compared to one another for the same number of elements and the same shape of discretization of a sphere. Table 4-1(a) shows that the curved panel method converges to the exact solution faster than the flat panel method

for the source formulation. Moreover, the vorticity panel method converges even faster than the source curved-panel method. It is surprising to see that the vorticity panel method yields almost the exact solution at the top of the sphere with only 48 elements. In the computation no attempt has been made to obtain better results by varying the spacings of the panels. Equal spacings were used. The velocities were calculated at nodal points which lie exactly on the actual surface of the body. The results for the vorticity panel method in Table 4-1(a) are obtained by solving the optimized influence matrix (optimization of only the influence matrix) under the constraint equations from the conservation condition with the use of Lagrange's multiplier method. In Table 4-1(b), the results from the vorticity panel method are computed by solving the optimized matrix (optimization of both the influence and conservation matrices). The results compare well with those in Table 4-1(a) and justify the present optimization scheme. In what follows the computed results are basd on the second scheme: optimization of both the influence and conservation matrices.

In Figures 24 - 26, we show the convergence of the velocity distributions over a sphere computed by the present methods as the number of elements increases. Comparing the three results, we can conclude, in general, that including the effect of the weakly nonlinear geometry accelerates the convergence of the numerical solutions to the exact solution as the number of elements used for the source formulation increases. The vorticity panel method shows even faster convergence than the source panel method. Hess and Smith[1962] used 4320 quadrilateral elements to obtain similar accuracy. Further investigation (not shown in this thesis) of

convergence with the number of elements used confirmed the conclusions stated above for most of the cases tried.

In addition, it was found that the source flat panel method has some difficulties in accurately predicting the velocity distributions near the region of high velocity gradient. The curved panel method appears to yield fairly good results even in this region. The cases tried are a prolate spheroid with fineness ratio 1/10, an oblate spheroid with fineness ratio 10, and various types of ellipsoids. For a prolate spheroid with 2640 elements, the planar source panel method yields only 2 computed values with more than 0.5 % error, and the rest of them have much less than 0.1 %. The curved source panel method achieved almost the same accuracy with 1104 elements.

In Figure 27, the effect of element spacings is demonstrated for a prolate spheroid by using the vorticity panel method. Distributing more elements for high velocity gradient region clearly gives better results.

In Figure 28, the extremely stable convergence of the vorticity panel method with respect to the number of elements used is demonstrated by calculating the velocity distributions over one of the most difficult shapes to treat, an oblate spheroid with finess ratio 10. These results again confirm the advantages of the vorticity panel method over other methods in which the unknowns are not the primitive variables.

In Figure 29, we compare the velocities computed by the present flat source panel method with the exact solution along various contours of an ellipsoid with major axes ratios 1 : 2 : 0.5. The agreement is generally quite good; except the computed results for z-onset flow in Figure 29(b) show some deviation from the exact solution. In Figure 29(b) the results

computed by the present curved panel method are also shown. The present curved source panel method shows better agreement than the flat source panel method.

For the far-field velocity calcualtion, we use the approximate induced velocity formulas in Appendix F in two forms. In one, they are used exactly as they stand, which is equivalent to replacing the triangular element by point sources and point quadrupoles. In the second, only the point source terms are retained. The criterion that determines the form of the approximate equations is the ratio of the distance between that point and the centroid of the triangular element to some characteristic dimension of the triangular element (in our case, the length of the largest edge of the element). If this ratio is larger than a certain prescribed number, the triangle is replaced by a point source and a quadrupole, unless the ratio is also larger than a second prescribed number, in which case the triangle is replaced by a point source alone. A number of cases are tested by comparing the velocities computed by the exact and approximate formulas for a variety of triangular shapes having unit source strength at all three nodes. In Figures 30 and 31 we show two typical results.

The local coordinates are (0,0), (0.5,1), (2,0). The centroid of the element is chosen as the center of the expansion. Thus the dipole terms are identically zero (for details, see Appendix F). From the extensive tests, we choose the factors 2.0 and 3.0 in order to keep the error less than 2 %. The error is evaluated by dividing the difference between the exact and approximate speeds by the exact value. For the curved element, the parameter ε in Equation 4.2is chosen to be 0.1332 from

the maximum allowable criterion we have chosen (see Appendix D). Even though the 2 % error looks too big, it does not cause any significant computational error because the actual contribution from an element far from the point is much smaller than from an element near the point. The extensive numerical experiments also confirmed this fact.

Since the basic velocity formulas are same for both the source and vorticity formulation, the statement about the multipole expansion also applies to the vorticity formulation.

V. THREE-DIMENSIONAL LIFTING PROBLEM

5.1 GENERAL

In the previous chapter, two numerical schemes were developed based on source and vorticity distributions to handle the nonlifting potential flows about arbitrary three dimensional bodies. The accuracy and stability of the vorticity formulation were shown to be far superior to the source formulations. Here we make the natural extension of the methods developed in the previous chapters to lifting bodies. Particular interest will be in small-aspect-ratio lifting bodies for which nonlinear relationships exist between aerodynamic forces and angles of attack. Some typical lifting bodies are wings of aircrafts and missiles and rudders of ships and submarines. Many of today's military aircraft and missiles designed for supersonic flight employ highly swept delta and delta-like wings of small aspect ratio which are typically thin. Also hang-gliders and the sails of the boats have the delta shape with negligible thickness. The rudders of ships and submarines have typically low-aspect-ratio rectangular shapes and employ streamlined section shape.

Many methods have been developed to predict the aerodynamic forces and flow details over small-aspect-ratio wings in the past. But the continuous vorticity panel methods have not been utilized extensively compared to other methods. The probable reason may be attributed to the two major difficulties mentioned in Chapter 1.

In this chapter we will develop two numerical methods based on continuous vorticity distributions: one for thin lifting, but not necessarily planar, bodies and the other for thick lifting bodies. Both methods account for vortex sheet separations along the sharp edges. It is assumed that no vortex breakdown occurs in our approach. In the present analysis the lifting surfaces are modelled with bound vortex sheets and the wakes are modelled with free vortex filaments. This combination of vortex sheets and vortex filaments makes the present scheme quite attractive over other methods. First, continuous vorticity distributions over the lifting surfaces make it possible to predict accurately continuous pressure distributions. Secondly, the use of vortex filaments in the wakes makes it possible to capture the tight rolling-up of the separated vortex sheet without any major problems.

5.2 DESCRIPTION OF THE METHOD

Since most of the development in Chapter 4 can be applied to this chapter, we will explain only what is needed to model the lifting surfaces. The description will be given for the thick body. The flat surface is a special case and the corresponding formulas will be mentioned at appropriate places.

5.2.1 DISCRETIZATION AND FORMULATION

We model the surface of the body by two sepatate vortex sheets. Two vortex sheets join along the edges of the body. There are two types of

edges: sharp edges where separation occurs and round edges where separation does not occur. We call the sharp edges where separation occurs separation lines. Along the separation lines two vortex sheets join, leave the wing and form the wake. But along the round edges the two vortex sheets merge into one sheet. The wakes are modelled by a number of strings of vortex filaments.

Referring to Figure 31, we discretize the surface of the body by triangular elements and the strings of vortex filaments in the wake by short straight segments joined end to end. On the wing we refer to the elements with two nodes on the separation line as separation elements (marked by ¢ in Figure 31) and the nodes on the separation lines as separation nodes. Thus two nodes from two elements, upper and lower surfaces, lie on one point on the separation line.

Since we employ two types of basic elements to model the flow, we need two basic velocity formulae. The first is the velocity induced by a linear vorticity distribution over a flat triangular element and was already obtained in Chapter 4. The second is the velocity induced by a small straight segment of vortex filament. This comes from the Bio-Savart law (see Equation 2.21). The velocity at a point in the flow field ,then, is the sum of induced velocities from the elements on the surface of the body and the elements in the wake.

Since there is no mechanism that can generate vorticity in the wake, each string of vortex filaments has constant circulation in steady flows. Moreover, the circulation is related to the strengths of the vortex sheets along the separation line through spatial conservation of vorticity. Referring to Figure 32, we find the amount of circulations coming out of

the lower surface and going into the upper surface. The difference between the two circulations must be shed into the wake and be the circulation of the wake element. In the course of calculating circulation that comes out of, or goes into, the vortex sheet, the vorticity vectors are also rotated onto the elementary plane of the separation element and then only the components perpendicular to the separation line are used. The vortex filament is attached to the center of the edge of the separation element. We obtain the following relationship:

$$\Gamma_w = \{\bar{t}^u \cdot (\bar{T}_1^u + \bar{T}_2^u) + \bar{t}^\ell \cdot (\bar{T}_1^\ell + \bar{T}_2^\ell)\} \frac{\ell}{2} \tag{5.1}$$

where ℓ is the length of the segment of the separation line, t is the unit vector normal to the separation line lying on the elementary plane, the T_1 and T_2 are the vorticity vectors at nodes 1 and 2, respectively, and the superscripts u and ℓ denote the upper and lower surfaces. For thin wings, only a vortex sheet is used and the equation above must be reduced correspondingly.

5.2.2 BOUNDARY CONDITIONS AND SOLUTIONS

In addition to the boundary and divergenceless conditions, two more conditions must be also satisfied for lifting surface with sharp-edges. The Kutta condition requires that the pressure jump must vanish along the edges of the lifting surface. This implies that the flow must come smoothly off the sharp edges of the surface. According to this Kutta condition, the vorticity at the sharp edges of the lifting surface must

be perpendicular to the edge and the first wake elements along the sharp-edges are aligned to be perpendicular to the edges and to lie on the mean-plane between the upper and lower surface. For delta-shaped wings, the first wake elements are fixed (at the center of each elementary edge) along the leading and trailing edges perpendicular to the edge on the mean plane of both surfaces. For parallelogram wings, the first wake elements are fixed only along the trailing edge. According to the Kelvin-Helmholtz theorem for an inviscid fluid, all the vorticity must be convected at the local particle velocity. This condition dictates a force-free wake and is used to obtain the position of wake.

Since the wake positions are not known beforehand, the initial positions are guessed. They are determined as part of the solutions by an iterative technique. The conservation matrix again comes from the divergenceless requirement on vorticity in all the elements on the lifting surface. The no-penetration and conservation conditions are imposed in a least squares sense subject to the constraint of a Kutta condition.

Next, with the known vorticity distribution, we align each segment in the wake with the velocity at its up-stream end. After relocation of the wake, one iteration is accomplished. Realigning the wake changes the velocity field and hence the no-penetration condition is no longer satisfied. Thus this procedure is repeated until some convergence criteria are satisfied. In this approach, we use two criteria: First the wake shape must converge. Second the strength of the vorticity distribution must converge. After the vorticity on the lifting surface and the wake shape have converged, the pressure distribution is readily obtained by

Bernoulli's equation. The details of all the calculations required above are given in Chapter 4.

5.3 NUMERICAL EXAMPLES

Figure 33 shows the discretization scheme of a flat delta wing. In Figure 34a, b, c, and d. we show the computed wake shapes and the vorticity field on a delta wing of unit aspect ratio for angles of attack, 5, 10, 15, and 20 degrees, respectively. The arrows show the direction and relative magnitude of the vorticity. The vorticity field computed by the present method appears to be consistent with that observed by Elle and Jones[1961], Hummel[1972], and that computed by Yen et al[1980]. It is also observed that as the angle of attack increases, the mutual interaction of the lines in the wake becomes stronger and the wake tends to roll up tightly over the upper surface of the wing.

In Figure 35, the normal-force coefficient is given as a function of angle of attack for a flat delta wing of unit aspect ratio. The numerical results obtained by the present method are compared with the experimental data of Peckham[1958] and Totsi[1974], and the theoretical results of Polhamus[1966] and Yen[1982]. There is fairly good agreement among the all results. The convergence of the present method is also shown as the number of rows (equivalently, the number of elements) increases. In Figures 36 - 38, the normal-force coefficients computed by the present method are given as functions of the angle of attack for various aspect ratio, planar delta wings. The agreement with other theoretical, numerical, and experimental results by Bartlett and

Vidal[1955], Peckam[1958], Bergesen and Porter[1960], Polhamus[1966], Wentz[1971], Kandil[1974], and Yen[1982] appears to be good.

Next, the present method is applied to the planar rectangular wing of unit aspect ratio. In Figure 39, the normal-force coefficients obtained by the present method are compared with the experimental data of Ermolenko[1966] and Lamar[1977]. The agreement is also fairly good.

In Figures 40 and 41, the computed pitching moments are compared with other numerical results and experimental data. The agreement is fairly good. Figure 42 compares the computed pressure distributions over a flat delta wing of unit aspect ratio to other numerical values and experimental data.

Figure 43 shows the discretized surface of a thick delta wing (half of the symmetric wing). The outer strip (shaded part) along the edges is the bevelled part of the surface to give sharp-edges. Peckham[1958] used a flat delta wing of unit aspect ratio with the edges bevelled at a 14 degree angle. The thickness was 1 % of the center chord. Exactly the same dimensions which Peckham used to build one of experimental models are used to test the present panel method developed for thick wings. Figure 44 shows the vorticity field on both surfaces and the wake shapes. These results are in close agreement with the result obtained for the flat delta wing before. In Figure 45, the normal-force coefficients computed by the present method show the clear convergence with the number of rows and compare well with the experimental data and the numerical results obtained before for a flat delta wing.

As a final example, we choose a thick rectangular wing. Figure 46 shows the vorticity field predicted by the present method over a NACA

$63_{(3)}$-018 airfoil for 15 degrees angle of attack. The formation of wing-tip vorticies and their movement inboard over the upper surface of the wing are consistent with the experimental observations of Francis and Kennedy[1979]. In Figure 47, we show the normal-force coefficients as a function of angle of attack. The results are compared with those obtained for a flat rectangular wing and the thickness effect on the normal-force coefficient is shown to decrease the lift.

VI. CONCLUSIONS AND RECOMMENDATIONS

In order to study the aerodynamic characteristics over various configurations, several panel methods are developed based on piecewise linear surface singularity distributions over an element. Two types of singularity are used, vorticity and source. Curved elements are also used to investigate the effect of weakly nonlinear geometry. The methods developed are discussed next.

A method for modelling general unsteady, potential, two-dimensional, lifting flows is developed. The problem is posed in terms of a coordinate system fixed to a reference configuration of the moving airfoil. A vortex sheet is wrapped around the surface of the airfoil. The vorticity (or equivalently the surface velocity) is a piecewise continuous, linear function of position on the airfoil. As an imitation of conditions at the trailing edge, the surface velocity there is replaced by a discrete vortex core. During each time step, this core is shed into the wake and a new core is formed. The cores that have been shed model the wake. Each is convected at the local particle velocity. At each time step, the unknowns are the values of the surface velocity at discrete points around the airfoil and the circulation around the new core at the trailing edge. Because the system is over-determined, these are obtained by an optimization scheme.

The present predictions are in good agreement with experimental data and other computations. The present program can also be used to analyze hydrodynamic propulsion. The present approach provides an attractive

alternative to those developed earlier, being easy to formulate, easy to use, and very accurate.

Two methods are developed for the calculation of nonlifting potential flows about arbitrary three-dimensional bodies. One is based on a piecewise linear source distribution over a curved triangular element while the other uses a piecewise linear vorticity distribution over a flat triangular element. Separations are assumed not to take place. For the source formulation, the use of curved elements leads to faster convergence as the number of elements increases than the use of planar elements. The vorticity formulation has three major differences from the source formulations: (1) the surface velocities are directly interpreted, (2) storage problems and the possibility of an ill-posed matrix due to the inter-dependence of the divergenceless equations can occur, and (3) the tangency condition of surface vorticity can be violated. Two major difficulties are resolved by using optimization and by rotating the vorticity along the edges of the elements. Extensive comparisons of the two methods for typical three-dimensional bodies show the superiority of the vorticity formulation; it is more stable and more accurate for a given number of elements.

The vorticity panel method is also extended to treat flows past thin as well as thick arbitrary lifting bodies with sharp-edge separation. To capture the pheonomenon of tightly rolling-up wakes, the wakes are modelled by discrete vorticies. The results predicted by the present methods for various lifting configurations show good quantitative agreement with experimental data as well as other numerical results. The present method predicts continuous pressure distributions on the lifting

surface which the earlier vortex-lattice methods cannot do. The effect of thickness is shown to decrease the aerodynamic forces.

The methods developed in this dissertation are quite general and are not restricted by body configurations and the number of bodies. The three-dimensional methods can also be extended to treat unsteady problems.

This is the first time that the continuous vorticity has been used for two-dimensional unsteady lifting flows. Moreover, two unique schemes, rotation of vorticity and optimization of both no-penetration condition and conservation condition, are introduced for the first time. It is also the first time that the continuous vorticity distribution and discrete vortices are used together in a single model. It is further noted that the slender body can be modelled either by a vortex sheet or by two vortex sheets.

BIBLIOGRAPHY

Albano, E. and Rodden, W. P., "A Doublet-Lattice Method for Calculating Lift Distributions on Oscillating Surfaces in Subsonic Flows," AIAA J., Vol. 7, No. 2, Feb. 1969, pp.279-285.

Anderson, J. D., Fundamentals of Aerodynamics, McGraw-Hill Inc., 1984, Ch. 4.

Angelucci, S. B., "A Multivortex Method for Axisymmetric Bodies at angle of Atack," J. Aircraft, Vol. 8, No. 12, Dec. 1971, pp.959-966.

Archibald, F. S., "Unsteady Kutta Condition at High Values of the Reduced Frequency Parameter," J. Aircraft, Vol. 12, No. 6, June 1975, pp.545-550.

Asfar, K. R., Mook, D. T., and Nayfeh, A. H., "Application of the Vortex-Lattice Technique to Arbitrary Bodies", J. Aircraft, Vol. 13, No. 7, July 1979, pp.421-424.

Atta, E. H., "Nonlinear Steady and Unsteady Aerodynamics of Wings and Wing-Body Combinations," Ph.D Dissertation, Engineering Science and Mechanics, VPI&SU, Blacksburg, VA, 1978.

Atta, E. H., Kandil, O. A., Mook, D. T., and Nayfeh, A. H., "Unsteady Aerodynamic Loads on Arbitrary Wings Including Wing-Tip and Leading Edge Separations," AIAA Paper 77-156, 1977. Plasma Dynamics Conference, July, 1978.

Atta, E. H. and Nayfeh, A. H., "Nonlinear Aerodynamics of Wing-Body Combinations," AIAA Paper 78-1206, AIAA 11th Fluid and Plasma Dynamics Conference, July, 1978.

Bartlett, G. E. and Vidal, R. J., "Experimental Investigation of Influence of Edge Shape on the Aerodynamic Characteristics of Low Aspect Ratio Wings at Low Speeds," J. Aero. Sci., Vol. 22, No. 8, Aug. 1955, pp.517-533.

Basu, B. C. and Hancock, G. J., "The Unsteady Motion of a Two Dimensional Airfoil in Incompressible Inviscid Flow," J. Fluid Mechanics, Vol. 87, pp. 159, 1978.

Belotserkovskii, S. M., "Theory of Thin Wings in Subsonic Flow," Translated from Russian, Plenum Press, N.Y. 1967.

Belotserkovskii, S. M., "Calculations of the Flow Around Wings of Arbitrary Planforms Over a Wide Range of Angles of Attack," NASA TT F-12, 391, May 1969.

Belotserkovskii, S. M. and Nisht, M. I., "Nonstationary Nonlinear Theory of a Thin Wing of Arbitrary Planform," Mechanika Zhidkosti Gasa, No. 4, 1974, pp.100-108.

Bergesen, A. J. and Porter, J. D., "An Investigation of the Flow Around Slender Delta Wings with Leading-Edge Separation," Rept. No. 510, Princeton Univ., Dept. of Aero. Engr., 1960.

Bollay, W., "A Non-Linear Wing Theory and its Application to Rectangular Wings of Small Aspect Ratio," ZAMM 19, 21-35, 1939.

Bradley, R. G., Smith, C. W. and Bhateley, I. C., "Vortex-Lift Prediction for Complex Wing Planforms," J. Aircraft, Vol.10, No. 6, June 1973, pp.379-381.

Bratt, J. B., "Flow Patterns in the Wake of an Oscillating Airfoil," R & M 2773, 1953, Royal Aeronautical Establishment.

Brebbia, C. A., The Boundary Element Method for Engineers, Pentch Press, 1980.

Brown, C. E. and Michael, W. H., "Effect of Leading-Edge Separation on the Lift of a Delta Wing," J. Aero. Sci., Oct. 1954, pp.690-694.

Carmichael, R. L., A Computer Program for the Estimation of the Aerodynamics of Wing-Body Combinations, NASA Ames Program Description, 1971.

Chen, S. and Dalton, C., "Unsteady Lifting case by Means of the Interior-Singularity Panel Mehtod," J. Aircraft, Vol. 19, No. 8, Aug. 1982, pp.634-638.

Chester, C. R., Techniques in Partial Differential Equations, McGraw-Hill, Inc., 1971.

Djojodihardjo, R. H. and Widnall, S. E., "A Numerical Method for the Calculation of Nonlinear, Unsteady Lifting Potential Flow Problems," AIAA J., Vol. 7, No. 10, Oct. 1969, pp.2001-2009.

Drischler, J. A. and Diederich, F. W., "Lift and Moment Responses to Penetration of Sharp-Edged Traveling Gusts, with Application to Penetration of Weak Blast Waves," NACA TN 3956, 1957.

Duffy, R. E., Czajkowski, E., and Jaran, C., "Finite Element Approximation to Theodorsen's Solution for Non-steady Aerodynamics of an Airfoil Section," AIAA Paper No. 84-1540.

Earnshaw, P. B., "An Experimental Investigation of the Structure of a Leading-Edge Vortex," ARC R & M No. 3281, 1961.

Earnshaw, P. B. and Lawford, J. A., "Low-Speed Wind-Tunnel Experiments on a Serious of Sharp-Edged Delta Wings," R & M, No. 3424, March 1964.

Edelen, D. G. B. and Kydoniefs, A. D., An Introduction to Linear Algebra, Elsevier, New York, 2nd Ed., 1976.

Ericsson, L. E. and Reding, J. P., "Unsteady Aerodynamics of Slender Delta Wings at Large Angles of Attack," J. Aircraft, Vol. 12, No. 9, Sept. 1975, pp.721-729.

Ermolenko, S. D., "Nonlinear Theory of Small Aspect Ratio Wings," Soviet Aeronautics,(in English), Vol. 9, 1966, pp.5-11.

Fairweather, G. and Johnston, R. L., "The Method of Fundamental Solutions for Problems in Potential Theory," pp.349-359 of C.T.H. Baker and G.F. Miller (Eds.), Treatment of Integral Equations by Numerical Methods, Academic Press, London, 1982

Falkner, V. M., "The Calculation of Aerodynamic Loading on Surfaces of Any Shape," Aeronautical Research Council, R & M, 1910(1953).

Fix, G. J., "Finite Element Models for Ocean Circulation Problems," SIAM J. Appl. Math., Vol.29, No.3, Nov. 1975, pp.371-387.

Fix, G. J., "On the Finite Element Methods of the Least Squares Type," Comp. Math. Appl., Vol.5, No.2, Nov. 1979, pp.87-98.

Fredholm, I., "Sur une classe d'equations fonctionelles," Acta. Math., Vol. 27, pp.365-390, 1903.

Friedberg, S. H., Insel, A. J., and Spence, L. E., Linear Algebra, Prentice-Hall, Englewood Cliffs, New Jersey, 1979.

Giesing, J. P., "Nonlinear Two-Dimensional Unsteady Potential Flow with Lift," J. Aircraft, Vol. 5, No. 2, March-April 1968, pp.135-143.

Giesing, J. P., "Potential Flow about Two-dimensional Airfoils," Douglas Aircraft Division, Rept. No. LB31946, 1965.

Giesing, J. P., "Vorticity and Kutta Condition for Unsteady Multi-Energy Flows," J. of Applied Mech., Vol. 91, pp. 608, 1969.

Giesing, J. P., Kalman, T. P., and Rodden, W. P., "Subsonic Unsteady Aerodynamics for General Configurations," AIAA Paper, No. 72-26, AIAA 10th Aerospace Sci. Meeting, Jan. 1972.

Goldstein, S., Modern Development in Fluid Dynamics, Vol. 2, Dover Publishing Co., 1965, pp.460.

Gorelov, D. N. and Kulyaev, R. L., "Nonlinear Problem of Unsteady Flow of an Incompressible Fluid Past a Slender Profile," Izvestiya Akademii Nauk SSSR, Mekhanika Zhidkosti i Gaza, No. 6, pp. 38-48, Nov.-Dec., 1971,(in English).

Graham, J. M. R., "The Lift on an Aerofoil in Starting Flow," J. Fluid Mechnics, Vol. 133, 1983, pp.413-425.

Helmholtz, H., "Theorie der Luftsschwingungen in Rohren mit offenen Enden," Crelle's J., Vol.57, pp.1-72, 1860.

Hess, J. L., "Calculation of Nonlifting Potential Flow about Arbitrary Three-dimensional Bodies," J. Ship. Res., 8, 1964.

Hess, J. L., "Calculation of Potential Flow about Arbitrary Three-dimensional Lifting Bodies," MDC J5679-01, final report, 1972.

Hess, J. L. and Robert, P. M. J., "Improved Solution for Potential Flow about Arbitrary Axisymmetric Bodies by the use of a Higher-Order Surface Source Method, Part I. Theory and Results," NASA CR 134694, July 1974.

Hess, J. L. and Smith, A.M.O., "Calcualtion of Nonlifting Potential Flow about Arbitrary Three Dimensional Bodies," Douglas Rept. E.S.40622, 1962.

Hess, J. L. and Smith, A.M.O., "Calcualtion of Potential Flow about Arbitrary Bodies," Progress in Aeronautical Sciences, Vol.8, 1967, pp.1-138.

Hummel, D., "Study of the Flow Around Sharp-Edged Slender Delta Wings with Large Angles of Attack," NASA TT F-15, 107, Sept. 1973, (Translation of Zeitschrift fur Flugwissenschaften, 1967, 15, pp.376-385).

Hummel, D. and Redeker, G., "Experimental Determination of Bound Vortex Lines and Flow in the Vicinity of the Trailing Edge of a Slender Delta Wing," NASA TT F-15, 012, Aug. 1972.

Jawson, M. A. and Ponter, A. R. S., "An Integral Equation Solution of the Torsion Problem," Proc. R. Soc. Lond., Vol. A273, pp.237-246, 1963.

Jawson, M. A., "Integral Equation Methods in Potential Theory,I," Proc. R. Soc. Lond., Vol. A275, pp.23-32, 1963.

Johnson, F. T. and Rubbert, P. E., "Advanced Panel-Type Influence Coefficient Methods Applied to Subsonic Flows," AIAA Paper 75-50, 1975.

Johnson, F. T., Tinoco, E. N., Lu, P., and Epton, M. A., "Recent Advances in the Solution of Three-Dimensional Flows over Wings with Leading Edge Vortex Separation," AIAA Paper 79-0282, 1979.

Johnston, R. L. and Fairweather, G., "The Method of Fundamental Solutions for Problems in Potential Flow," Appl. Math. Modelling, Vol.8, pp.265-270, August 1984

Jones, R. T., "The Unsteady Lift of a Finite Wing," NACA TN 682, Jan. 1939.

Kadlec, R. A. and Davis, S. S., "Visualization of Quasiperiodic Flows," AIAA J., Vol. 17, No. 11, Nov. 1979, pp.1164-1169.

Kalman, T. P., Rodden, W. P., and Giesing, J. P., "Application of Doublet-Lattice Method to Nonplanar Configurations in Subsonic Flow," J. Aircraft, Vol. 8, No. 6, June 1971, pp.406-413.

Kandil, O.A., Mook, D. T., and Nayfeh, A. H., "Nonlinear Prediction of Aerodynamic Loads on Lifting Surfaces," J. Aircraft, Vol. 13, Jan. 1976, pp.22-28.

Kandil, O.A., "Numerical Prediction of Vortex Cores from the Leading and Trailing Edges of Delta Wings," ICAS Paper 14-2, The 12th Congress of the International Council of the Aeronautical Sciences, Munich, FRG, Oct. 1980.

Kandil, O.A., "Computational Technique for Three-dimensional Compressible Flow Past Wings at High Angles of Attack," AIAA Paper No. 83-2078, AIAA Atmospheric Fleight Mechanics Conference, Gatlinsburg, TN, Aug. 1983.

Kandil, O.A. and Balakrishnan, L., "Recent Improvements in the Prediction of the Leading and Trailing Edge Vortex Cores of the Delta Wings," AIAA Paper 81-1263, 1981.

Kandil, O.A., Atta, E. H., and Nayfeh, A. H., "Three Dimensional Steady and Unsteady Asymmetric Flow Past Wings of Arbitrary Planforms," AGARD Paper No. 2, AGARD Fluid Dynamics Panel Symposium, Unsteady Aerodynamics, Ottawa, Canada, 1977.

Kandil, O.A., Chu, L., and Yates, E. C. Jr., "Hybrid Vortex-Method for Lifting Surfaces with Free Vortex Flow," AIAA Paper 80-0070, 1980.

Kandil, O.A., Chu, L., and Tureaud, T., "A Nonlinear Hybrid Vortex Method for Wings at Large Angle of Attack," AIAA Journal, Vol. 22, No. 3, March 1984, pp.329-336.

Karamcheti, K., Principles of Ideal-Fluid Aerodynamics, Robert E. Krieger Publishing Co., 1980.

von Karman, T. and Sears, W. R., "Airfoil Theory for Non-Uniform Motion," J. Aeronautical Sciences, Vol. 5, No. 10, Aug. 1938, pp.379-390.

Katz, J. and Weihs, D., "Behavior of Vortex Wakes from Oscillating Airfoils," J. Aircraft, Vol. 15, No. 12, Dec. 1978, pp.861.

Katz, J. and Weihs, D., "Wake Rollup and the Kutta Condition for Airfoils Oscillating at High Frequency," AIAA J., Vol. 19, No. 12, Dec. 1981, pp.1604-1606.

Kirchoff, G., Zur Theorie der Lichstranlen, Berl. Ber., pp.641, 1882.

Konstantinopoulos, P., "A Vortex-Lattice Method for General, Unsteady, Subsonic Aerodynamics," M.S. Thesis, Dept. of Engr. Sci. and Mech., Virginia Polytechnic Institute and State Univ., July 1981.

Korner, H. and Hirschel, E. H., "The Calculation of Flow Fields by Panel Methods: a Report on Euromech 75," J. Fluid Mech., Vol. 79, Part.1, 1977, pp.181-189.

Kuhlman, J., "Load Distributions on Slender Delta Wings Having Vortex Flow," J. Aircraft, Vol. 14, No. 7, July 1977, pp.699-702.

Kussner, H. G., "Das zweidimensionale Problem der beliebig bewegten Tragflache unter Berucksichtigung von Partialbewegungen der Flussigkeit," Luftfahrtforschung, Vol. 17, 1940, pp.355.

Lamar, J. E., "Prediction of Vortex Flow Characteristics of Wings at Subsonic and Supersonic Speeds," J. Aircraft, Vol. 13, No. 17, July 1976, pp.490-494.

Lamar, J. E., "Recent Studies of Subsonic Vortex Lift Including Parameters Affecting Stable Leading-Edge Vortex Flow," J. Aircraft, Vol. 14, No. 12, Dec. 1977, pp.1205-1211.

Lan, C. E., "A Quasi-Vortex-Lattice Method in Thin Wing Theory," J. Aircraft, Vol. 11, no. 9, Sep. 1974, pp.518-527.

Lavin, D. and Katz, J., "Vortex-Lattice Method for the Calculation of the Nonsteady Separated Flow over Delta Wings," J. Aircraft, Vol. 18, Dec. 1981, pp.1032-1037.

Lawrence, H. R. and Gerber, E. H., "The Aerodynamic Forces on Low Aspect Ratio Wings Oscillating in an Impulsively Flow," J. Aero. Sci., Nov. 1952, pp.768-781.

Mangler, K. W. and Smith, J. H. B., "A Theory of the Flow Past a Slender Delta Wing with Leading-Edge Separation," Proc. Royal Soc., London, A 251, 200-217, 1959.

Marsden, D. J., Simpson, R. W., and Rainbird, W. J., "An Investigation into the Flow over Delta Wings at Low Speeds with Leading-Edge Separation," Rept. No. 114, College of Aeronautics, Cranfield, 1957.

Maskell, E. C., "Some Recent Development in the Study of Edge Vortices," Proceedings of 3rd Conference of Int. Counc. Aero. Sci., 737-749, 1962, Sportan Books, Inc. Washington, 1964.

Maskew, B., "Subvortex Technique for the Close Approach to a Discretized Vortex Sheet," J. Aircraft, Vol. 14, No. 2, Feb. 1977, pp.188-193.

Maskew, B., "Prediction of Subsonic Aerodynamic Characteristics: A Case for Low-Order Panel methods," J. Aircraft, Vol. 19, No. 2, Feb. 1982, pp.157-163.

Mook, D. T. and Maddox, S. A., "Extention of a Vortex-Lattice Method to Include the Effects of Leading-Edge Separation," J. Aircraft, Vol.11, 1974, pp.127-128.

Moore, D. W., "A Numerical Study of the Roll-up of a Finite Vortex Sheet," J. Fluid Mechanics, Vol. 63, part 2, 1974, pp.225-235.

Nayfeh, A. H., Mook, D. T., and Yen, A., "The Aerodynamics of Small Harmonic Oscillations Around Large Angles of Attack," AIAA Paper No. 79-1520, 1979.

Oswatitsch, J., "Die Geschwindigkeitsuerteiling bei lokalen Uberschallgebieten an flachen Profilen," ZAMM, Vol. 30, 1950, pp.17-24.

Peckam, D. H., "Low-Speed Wind-Tunnel Tests on a Series of Uncambered Slender Pointed Wings with Sharp Edges," R/M 3186, British Aeronautical Research Council, 1958.

Polhamus, E. C., "A Concept of the Vortex Lift of Sharp-Edged Delta Wings based on a Leading-Edge-Suction Analogy," NACA TN-D 3767, 1966.

Prandtl, L. and Tietjens, O. G.(1931), Fundamentals of Hydro and Aerodynamics, Dover Publications, Inc. 1957, Ch. 12.

Proudman, J., "A theorem in tidal dynamics," Phil. Mag., Vol.49, pp.570-573, 1925.

Raj, P. and Gray, R.B., "Computation of Two-dimensional Potential Flow Using Elementary Vortex Distributions," J. Aircraft, Vol. 15, No. 10, Oct. 1978.

Raj, P. and Gray, R.B., "Computation of Three-dimensional Potential Flow Using Surface Vorticity Distribution," J. Aircraft, Vol.16, No.3, March 1979, pp.162-169.

Raj, P. and Iversen, J. D., "Inviscid Interaction of Trailing Vortex Sheets Approximated by Point Vortices," J. Aircraft, Vol. 15, No. 12, Dec. 1978, pp.857-859.

Rayleigh, Lord, Theory of Sound, Dover, NYC, New York (reprint), 1887.

Reddy, J. N., An Introduction To the Finite Element Method, McGraw-Hill Book Co., 1984

Rehbach, C., "Calculation of Flow Around Zero-Thickness Wings with Evolute Vortex Sheets," NASA TT F-15, 183, 1973

Rehbach, C., "Numerical Investigation of Vortex Sheets Issuing from Separation Line Near the Leading Edge," NASA TT F-15,530, 1974.

Rowe, W. S., Redman, M. C., Ehlers, F. E., and Sebastian, J. D., "Prediction of Unsteady Aerodynamic Loadings Caused by Leading Edge and Trailing Edge Control Surface Motion in Subsonic Compressible Flow - Analysis and Results," NASA CR-2543, 1975.

Rubbert, P. E. and Sarris, G. R., "A General Three-dimensional Potential-Flow Method Applied to V/STOL Aerodynamics," SAE Paper No. 680304, 1968.

Satyanarayana, B. and Davis, S., "Experimental Studies of Unsteady Trailing-Edge Conditions," AIAA J., Vol. 16, No. 2, Feb. 1978, pp.125-129.

Scholz, N., "Kraft-und Druckverteilungsmessungen an Tragflachen Kleiner Streckung," Forschung auf dem Gebiete des Ingenieurwesens, Part B, Vol. 16, No. 3, 1949-1950, pp.85-91.

Shen, C. C., Lopez, M. L., and Wasson, N. F., "Jet-Wing Lifting-Surface Theory Using Elementary Vortex Distributions," J. Aircraft, Vol. 12, No. 5, May 1975, pp.448-456.

Smith, J. H. B., "Improved Calculations of Leading-Edge Separation from Slender Delta Wings," Proc. Royal. Soc., Lond., A 306, 1968, RAE Tech. Rept. 66070, 1966.

Smith, A. M. O. and Hess, J. L., "Calculation of the Nonlifting Potential Flow about Arbitrary Three-dimensional Bodies," Douglas Rept. No. E.S.40622, 1962.

Strang, G. and Fix, G. J., An Analysis of the Finite Element Method, Prentice-Hall, Englewood Cliffs, NJ, 1973.

Summa, J. M., "Potential Flow about Three-Dimensional Lifting Configurations with Application to Wings and Rotors," AIAA Paper 75-126, 1975.

Summa, J. M., "A Numerical Method for the Exact Calculation of Airloads Associated with Impulsively Started Wings," AIAA Paper 77-002, 1977.

Symm, G. T., "Integral Equation Methods in Potential Theory,II," Proc. R. Soc. Lond., Vol. A275, pp.33-46, 1963.

Telionis, D. P. and Poling, D. R., "The Response of Airfoils to Periodic Disturbances - The Unsteady Kutta Condition," AIAA 84-0050, Aerospace Sciences Meeting, Reno NV, Jan. 1984.

Theodorsen, T. , "General Theory of Aerodynamic Instability and the Mechanism of Flutter," NACA TR No.496, 1935.

Thrasher, D. F., "Nonlinear Unsteady Aerodynamics with Application to Dynamic-Aerodynamic Interaction," M.S. Thesis, Dept. of Engr. Sci. and Mech., VPISU, Blacksburg, VA, May 1979.

Thrasher, D. F., Mook, D. T., and Nayfeh, A. H.,"A Computer-Based Method for Analyzing the Flow over Sails,"

Thrasher, D. F., Mook, D. T., Kandil, O. A., and Nayfeh, A. H., "Application of the Vortex-Lattice Concept to General, Unsteady Lifting-Surface Problems," AIAA Paper 77-1157, Aug. 1977.

Totsi, L. P., "Low-speed Static Stability and Damping-in-Roll Characteristics of Some Swept and Unswept Low-Aspect Ratio Wings," NACA TN 1468, 1974

Ueda, T. and Dowell, E. H., "A New Solution Method for Lifting Surfaces in Subsonic Flow," AIAA J., Vol. 20, No. 3, Mar. 1982, pp.348-355.

Wagner, H., "Dynamischer Auftrieb von Tragflugeln," Zeitschrift fuer Angewandte Mathematik und Mechanik, Vol. 5, Feb. 1925, pp.17-35.

Watkins, C. E., Woolston, D. S., and Cunningham, H. J., "A Systematic Kernel Function Procedure for Determining Aerodynamic Forces on Oscillating or Steady Finite Wings at Subsonic Speeds," NASA TR R-48, 1959.

Weber, J. A., Brune, G. W., Johnson, F. T., Lu, P., and Rubbert, P. E., "Three Dimensional Solution of Flows over Wings with Leading Edge Vortex Separation," AIAA J., Vol. 14, 1976, pp. 519-525.

Wenzinger, C. J., "Pressure Distribution over an N.A.C.A. 23012 Airfoil with an N.A.C.A. 23012 External-Airfoil Flap," NACA Rept. 614, July, 1937. pp. 38-48, Nov.-Dec., 1971,(in English).

Winter, H., "Flow Phenomena on Plates and Airfoils of Short Span," NACA Rept. 798, 1937.

Woodward, F. A., Tinoco, E. N., and Larsen, J. W., "Analysis and Design of Supersonic Wing-Body Combination, Including Properties in the Near-Field," NASA CR-73106, 1967.

Yen, A., "A Continuous Vorticity Panel Method for the Prediction of Steady Aerodynamic Loads on Lifting Surfaces," Dissertation, 1982, VPISU, Blacksburg, VA.

Yen, A., Mook, D. T., and Nayfeh, A. H., "Nonlinear Continuous-Vorticity Aerodynamic Model," AIAA Paper No. 80-0311, 18th Aerospace Sciences Meeting, Pasadena, CA, Jan. 1980.

APPENDIX A. TANGENCY CONDITION

Here we show the significance of setting div A = 0. We begin with the vector potential.

$$\bar{A}(P) = \frac{1}{4\pi} \int \int_{\tau} \int \frac{\bar{\Omega}(Q)}{r(P,Q)} \, d\tau(Q) \tag{A.1}$$

where the coordinate of point P is (x,y,z), that of point Q is (ξ,η,ζ), and

$$r(P,Q) = \sqrt{(x-\xi)^2+(y-\eta)^2+(z-\zeta)^2}$$

Let's take the divergence of the vector potential.

$$\nabla_P \bullet \bar{A}(P) = \frac{1}{4\pi} \nabla_P \bullet \left[\int \int_{\tau} \int \frac{\bar{\Omega}(Q)}{r(P,Q)} \, d\tau(Q) \right]$$

$$= \frac{1}{4\pi} \int \int_{\tau} \int \nabla_P \bullet \left\{ \frac{\bar{\Omega}(Q)}{r(P,Q)} \right\} d\tau(Q)$$

$$= \frac{1}{4\pi} \int \int_{\tau} \int \left[\nabla_P \left(\frac{1}{r}\right) \bullet \bar{\Omega}(Q) + \frac{1}{r} \nabla_P \bullet \bar{\Omega}(Q) \right] d\tau(Q)$$

$$= \frac{1}{4\pi} \int \int_{\tau} \int \left[\nabla_P \left(\frac{1}{r}\right) \bullet \bar{\Omega}(Q) \right] d\tau(Q)$$

$$= -\frac{1}{4\pi} \int \int_{\tau} \int \left[\nabla_Q \left(\frac{1}{r}\right) \bullet \bar{\Omega}(Q) \right] d\tau(Q)$$

$$= -\frac{1}{4\pi} \int \int_{\tau} \int \left[\nabla_Q \bullet \left\{ \frac{\bar{\Omega}(Q)}{r} \right\} - \frac{1}{r} \nabla_Q \bullet \bar{\Omega}(Q) \right] d\tau(Q)$$

$$= -\frac{1}{4\pi} \int_{\sigma} \int \left[\frac{\bar{\Omega}(Q)}{r} \bullet \bar{n} \right] d\sigma(Q) = 0 \tag{A.2}$$

In the last step the divergence theorem was used. During the derivation was used that $\nabla_P(1/r) = -\nabla_Q(1/r)$ as well as the divergenceless field of vorticity. Therefore, the vorticity must be tangent to the boundary of the region of vorticity (tangency condition). This is the sufficient and also necessary condition for div A = 0.

APPENDIX B. LEAST SQUARES SOLUTION

In the least squares principle, the aggregate squared error is minimized. Take an over-determined system, m linear equations for n unknowns ($m \geq n$). Now define [P]as the m x n matrix, {X} as the n x 1 unknown column vector, and {B} as the n x 1 column vector. Also assume that the rank of [P] equals n. Then, the error vector is given as:

$$\{E\} = [P]\{X\} - \{B\} \tag{B.1}$$

The sum of errors, thus, is:

$$\begin{aligned} S &= \{E\}^T\{E\} \\ &= \{X\}^T[P]^T[P]\{X\} - 2\{X\}^T[P]^T\{B\} + \{B\}^T\{B\} \end{aligned} \tag{B.2}$$

where the superscript T denotes the transpose. Setting $\nabla_X S = 0$, we obtain

$$[P]^T[P]\ \{X\} = [P]^T\{B\} \tag{B.3}$$

which has the solution

$$\{x\} = ([P]^T[P])^{-1}([P]^T\{B\}) \tag{B.4}$$

The solution is unique because the rank of m x n matrix [P] equals n.

Even though it is correct to assume that the normal equations (i.e., $[P]^T[P]$) provide the way to compute a solution to the least squares problem, one should avoid actually computing the normal equations. The actual computation of normal equations may cause difficulties not inherent in the original least squares problem itself. One good way around the difficulty is to use the QR decomposition (see Friedberg, et al[1979] and Edelen, et al[1976]). If $[P] = [Q][R]$ is the decomposition, so that $[Q]$ is m x n and has real orthonormal columns while $[R]$ is n x n and upper triangular, then the normal equations from (B.3) can be written

$$([Q][R])^T([Q][R])\{X\} = ([Q][R])^T\{B\} \tag{B.5}$$

and become

$$[R]^T[R]\{X\} = [R]^T[Q]^T\{B\} \tag{B.6}$$

since $[Q]^T[Q] = [I]$. Because the rank of $[P]$ equals n, the rank of $[R]$ equals n and hence $[R]$ and $[R]^T$ are nonsingular. Therefore we conclude from (B.6) that

$$[R]\{X\} = [Q]^T\{B\} \tag{B.7}$$

which is simply a triangular system of equations to be solved for the least squares solution $\{X\}$.

APPENDIX C. TWO-DIMENSIONAL STREAMLINES

The two dimensional analysis may not be restricted only to find the loads acting on the body. The analysis can be easily extended to find streamlines and potential lines. In the following the direct method of computing the streamlines will be developed based on the stream function. In two dimension, the potential-lines are perpendicular to the stream-lines. Thus this method can be used to compute the potential-lines too.

With the use of Taylor series, the stream function is expanded about a point(x,y).

$$\psi(x+dx,y+dy) = \psi(x,y) + \frac{\partial\psi}{\partial x}\,dx + \frac{\partial\psi}{\partial y}\,dy + \frac{1}{2}\left\{\frac{\partial^2\psi}{\partial x^2}\,dx^2 + 2\frac{\partial^2\psi}{\partial x\partial y}\,dxdy + \frac{\partial^2\psi}{\partial y^2}\,dy^2\right\} + O(ds^3) \qquad (C.1)$$

where

$$ds = \sqrt{dx^2 + dy^2}$$

The simple scheme with first order accuracy can be obtained by considering the only the first three terms on the right-hand side of the Equation C.1. Noting the fact that $\psi(x+dx,y+dy) = \psi(x,y)$ and $\partial\psi/\partial x = -v$, $\partial\psi/\partial y = u$, we obtain that

$$-u\,dx + v\,dy = O(ds^2) \qquad (C.2)$$

where u and v are the x and y-components of the velocity. Using Equation C.2, the dx and dy can be expressed in terms of ds and velocity components.

$$dx = sgn(dx)\ ds\ /\ \sqrt{1 + (v/u)^2} = u\ ds\ /\ \sqrt{u^2 + v^2} \qquad (C.3)$$
$$dy = sgn(dy)\ ds\ /\ \sqrt{1 + (u/v)^2} = v\ ds\ /\ \sqrt{u^2 + v^2}$$

Equation C.3 is of first order accuracy.

For the second order accuracy, the second order terms in Equation C.1 must be included.

$$-u\ dx + v\ dy + \frac{1}{2}\{\frac{\partial v}{\partial x}\ dx^2 + 2\ \frac{\partial u}{\partial y}\ dxdy + \frac{\partial u}{\partial y}\ dy^2\} + O(ds^3) = 0 \qquad (C.4)$$

There are two choices to compute dx and dy. The reason is simply to avoid the singular case when dx or dy approaches zero. This choice in the following also helps the accuracy of the results. We introduce the following notations:

$$s = \frac{dy}{dx} \quad \text{and} \quad r = \frac{dx}{dy} \qquad (C.5)$$

Then depending on the ratio of dx and dy, we compute s($v/u < 1$) or r($v/u \geq 1$). From Equation C.4 we obtain the following two equations depending on the case.

(Case 1). $v/u < 1$

$$as^2 + 2bs + c = O(ds^2) \tag{C.6}$$

where

$$a = \frac{1}{2}\frac{\partial u}{\partial x}\,dx,\quad b = \frac{1}{2}\left(u + \frac{\partial u}{\partial x}\,dx\right),\quad \text{and}\quad c = -\left(v + \frac{1}{2}\frac{\partial v}{\partial x}\,dx\right)$$

(Case 2). $v/u \geq 1$

$$ar^2 + 2br + c = O(ds^2) \tag{C.7}$$

where

$$a = -\frac{1}{2}\frac{\partial v}{\partial y}\,dy,\quad b = \frac{1}{2}\left(-v + \frac{\partial u}{\partial x}\,dy\right),\quad \text{and}\quad c = \left(u + \frac{1}{2}\frac{\partial u}{\partial y}\,dy\right)$$

Solving the equations above, we obtain s and r, respectively.

$$s = \{-b + \mathrm{sgn}(b)\sqrt{(b^2 - ac)}\} / a \quad \text{for } v/u < 1 \tag{C.8}$$

$$r = \{-b + \mathrm{sgn}(b)\sqrt{(b^2 - ac)}\} / a \quad \text{for } v/u \geq 1 \tag{C.9}$$

In the equations above the sign of b is determined so that the expansion for $b/a \gg 1$ be consistent with the first-order approximation. Therefore, depending on the case, for given dx(or dy) we obtain dy = s dx(or dx = r dy). Then the new position is determined by adding the dx and dy to the old position.

APPENDIX D. WEAKLY NONLINEAR GEOMETRY

Here we develop the potential formula for weakly nonlinear geometry. First, the real surface is simulated by a paraboloidal surface. Secondly, the simulated surface is determined under some restrictions. Thirdly, the implications of the assumptions are shown. Finally, the potential formula for the simulated surface is expanded to give an explicit formula with respect to planar surface.

D.1 APPROXIMATION OF CURVED SURFACE

The potential formula for a curved surface is expanded and expressed for planar surface under some assumptions. We begin with the potential formula referring to Figure 48.

$$\phi = \int_\sigma \int \frac{S\, d\sigma}{r} = \int_\Sigma \int \frac{S \sec\gamma\, d\Sigma}{r} \tag{D.1}$$

where

$$r = \sqrt{(x-\xi)^2+(y-\eta)^2+(z-\zeta)^2}$$

and

$$\cos\gamma = \bar{n} \cdot \bar{k}$$

Here the paraboloidal surface is represented as follows:

$$\varepsilon D_0 - \zeta = \varepsilon\{(\xi-A_0)^2+k(\eta-B_0)^2\} \tag{D.2}$$

From the above equation, the unit normal vector to the surface is obtained.

$$\bar{n} = \{2\varepsilon(\xi-A_0)\bar{i}+2\varepsilon k(\eta-B_0)\bar{j}+\bar{k}\}/[1+4\varepsilon^2\{(\xi-A_0)^2+k^2(\eta-B_0)^2\}] \qquad (D.3)$$

Here, we make the assumption (Assumption 1) that

$$4\varepsilon^2\{(\xi-A_0)^2 + k^2(\eta-B_0)^2\} << 1 \qquad (D.4)$$

The implication of Equation D.4 will be shown in the following section. Then, the normal unit vector to the surface is approximated as

$$\bar{n} \simeq 2\varepsilon(\xi-A_0)\bar{i} + 2\varepsilon k(\eta-B_0)\bar{j} + \bar{k} \qquad (D.5)$$

With the arguments above, we obtain

$$\cos\gamma = \bar{n} \cdot \bar{k} \simeq 1 \qquad (D.6)$$

Since the geometric nonlinearity is assumed to be weak and the ζ is a function of ξ and η, we expand the term $1/r$ in Equation D.1 as follows: For convenience, some notation are introduced as follows.

$$R = \sqrt{(x-\xi)^2+(y-\eta)^2}$$

$$z_p = z - z_0 \qquad (D.7)$$

and

$$\rho = \sqrt{R^2 + z_p^2}$$

Then, it follows that

$$1/r = 1/\rho \cdot 1/\sqrt{1+\{2z_p(z_0-\zeta)+(z_0-\zeta)^2\}/\rho^2} \tag{D.8}$$

Now we make another assumption (Assumption 2) that

$$\max(z_0-\zeta)/\rho^2 << 1 \tag{D.9}$$

We obtain

$$1/r \simeq 1/\rho - z_p(z_0-\zeta)/\rho^3 + \text{H.O.T.} \tag{D.10}$$

Therefore, Equation D.1 becomes

$$\phi \simeq \int_\Sigma \frac{S d\Sigma}{r} = \int_\Sigma S\{1/\rho - z_p(z_0-\zeta)/\rho^3\}d\Sigma \tag{D.11}$$

This equation may be integrated explicitly. In the following section, we determine the coefficients in Equation D.2

D.2 DETERMINATION OF SIMULATED SURFACE

Referring to Figure 49, we force the surface σ to pass through the three nodes of the element. This will give three equations from Equation D.2 as follows:

$$D_0 = A_0^2 + kB_0^2 \tag{D.12}$$

$$D_0 = (b-A_0)^2 + k(c-B_0)^2 \tag{D.13}$$

$$D_0 = (a-A_0)^2 + kB_0^2 \tag{D.14}$$

From these three equations, we obtain that

$$A_0 = a/2 \tag{D.15}$$

$$B_0 = \{c^2 - b(a-b)/k\}/2c \tag{D.16}$$

$$D_0 = A_0^2 + kB_0^2 \tag{D.17}$$

In order to determine k, we force the center of the surface σ to be closest to the centroid of the triangular element. In other words, we use a least-squares optimization to minimize the distance between two points. The sum of squared errors is given as

$$\begin{aligned} E &= (A_0-x_c)^2 + (B_0-y_c)^2 \\ &= \{\frac{a}{2} - \frac{a+b}{3}\}^2 + [\frac{1}{2c}\{c^2 - \frac{b(a-b)}{k}\} - \frac{c}{3}]^2 \end{aligned} \tag{D.18}$$

Minimizing this error, we obtain

$$k = \frac{3b(a-b)}{c^2} \tag{D.19}$$

In order to determine ε, we dictate that the normal unit vectors of the surface σ at three nodes be closest to those of the real surface of the body. From Equation D.2 we obtain three normal unit vectors at nodes.

$$\bar{n}_{1\sigma} = -2\varepsilon A_0 \bar{i} - 2\varepsilon k B_0 \bar{j} + \bar{k}$$

$$\bar{n}_{2\sigma} = 2\varepsilon(b-A_0)\bar{i} + 2\varepsilon k(c-B_0)\bar{j} + \bar{k} \tag{D.20}$$

$$\bar{n}_{3\sigma} = 2\varepsilon(a-A_0)\bar{i} - 2\varepsilon kB_0\bar{j} + \bar{k}$$

Then, the sum of squared errors becomes

$$E = (\bar{n}_1 - \bar{n}_{1\sigma})^2 + (\bar{n}_2 - \bar{n}_{2\sigma})^2 + (\bar{n}_3 - \bar{n}_{3\sigma})^2 \tag{D.21}$$

where n_1, n_2, and n_3 are the normal unit vectors of the actual surface at the three nodes. Minimizing the error, we obtain

$$\varepsilon = \{-A_0(n_{1x}+n_{2x}+n_{3x}) - kB_0(n_{1y}+n_{2y}+n_{3y}) + (bn_{2x}+kcn_{2y}+an_{3x})\}/$$

$$2\{A_0^2+2k^2B_0^2+(b-A_0)^2+k^2(c-B_0)^2+(a-A_0)^2\} \tag{D.22}$$

D.3 JUSTIFICATION OF ASSUMPTIONS

The implications of the assumptions which were made in the foregoing discussion will be shown here. Let

$$\omega = \max_{\Sigma} |\zeta(\xi,\eta)| = \varepsilon D_0 = \varepsilon(A_0^2+kB_0^2) \tag{D.23}$$

$$D = 2 \max \sqrt{(\xi-A_0)^2+(\eta-B_0)^2} \tag{D.24}$$

and

$$\delta = \max_{\Sigma} \left[\sqrt{\varepsilon^2(\xi-A_0)^2+\varepsilon^2k^2(\eta-B_0)^2} \right] / 2 \tag{D.25}$$

Then, we can show that

$$w/D \leq \delta \tag{D.26}$$

D.3.1 JUSTIFICATION OF ASSUMPTION 1

The assumption is in terms of δ

$$4\varepsilon^2\{(\xi-A_0)^2 + k^2(\eta-B_0)^2\} \leq (4\delta)^2 << 1 \tag{D.27}$$

D.3.2 JUSTIFICATION OF ASSUMPTION 2

Let

$$\varepsilon_m = \max \{|z_0-\zeta|/R\} \tag{D.28}$$

Then,

$$|\{2z_p(z_0-\zeta)+(z_0-\zeta)^2\}/\rho^2| \leq \{2z_p\varepsilon_m/R+\varepsilon_m^2\} \tag{D.29}$$

But,

$$\begin{aligned} R\varepsilon_m &= \max\ [\zeta(x_0,y_0)-\zeta(\xi,\eta)] \\ &= \max\ [\varepsilon(x_0-A_0)^2+\varepsilon k(y_0-B_0)^2-\varepsilon(\xi-A_0)^2-\varepsilon k(\eta-B_0)^2] \\ &= \max\ [\varepsilon(x_0+\xi-2A_0)(x_0-\xi)+\varepsilon k(y_0+y-2B_0)(y_0-\eta)] \end{aligned}$$

Using the Holder inequality, we obtain

$$
\begin{aligned}
R\varepsilon_m &\le \max \left| [\varepsilon^2\{(x_0-A_0)+(\xi-A_0)\}^2+\varepsilon^2k^2\{(y_0-B_0)+(\eta-B_0)\}^2]^{1/2} \right. \\
&\quad \left. \cdot \; [(x_0-A_0)^2+(y_0-\eta)^2]^{1/2} \right| \\
&\le 2 \max \, [\varepsilon^2(\xi-A_0)^2+\varepsilon^2k^2(\eta_0-B_0)^2]^{1/2} \\
&= 4\delta
\end{aligned}
\tag{D.30}
$$

From the discussion above, the weakly nonlinear geometry means that the ratio of max height to the diameter of the element is relatively small. The relatively small nonlinear effect of curved surface is controlled by making δ small. As a rule of thumb, we take, in our approach

$$
\delta \simeq 0.079 \qquad \text{or} \quad (4\delta)^2 \simeq 1 \tag{D.31}
$$

APENDIX E. VELOCITY FORMULA

E.1 DEVELOPMENT

We begin with Equation 4.1. First, the surface singularity is approximated by linear function over a typical triangular element. Using the interpolation functions for an triangular element, we write

$$S = S_i\psi_i \equiv S_i(a_i + b_i\xi + c_i\eta) \tag{E.1}$$

where

$$a_i=(\xi_j\eta_k - \eta_j\xi_k)/2\Delta$$
$$b_i=(\eta_j - \eta_k)/2\Delta$$
$$c_i=(\xi_k - \xi_j)/2\Delta$$

and

$$2\Delta = -ac$$

Here, (ξ_i,η_i) are the local coordinates of the three nodes. Also the summation convention was used on indices and (i,j,k) is of cyclic order. Before we procede, we introduce some notation as follows:

$$H(M,N,K) = \int_\Sigma\int \{(x-\xi)^M(y-\eta)^N/\ \rho^K\}d\Sigma$$
$$\alpha = x-A_0 \tag{E.2}$$
$$\beta = y-B_0$$
$$K = \varepsilon(D_0-\alpha^2-k\beta^2)-z_0$$

Then, the scalar potential can be written as

$$\phi = \{a_i\tilde{\phi}_1 + b_i(x\tilde{\phi}_1-\tilde{\phi}_2) + c_i(y\tilde{\phi}_1-\tilde{\phi}_3)\}S_i$$
$$\equiv \{a_i\phi_1 + b_i\phi_2 + c_i\phi_3\}S_i \qquad (E.3)$$

where

$$\tilde{\phi}_1 = H(0,0,1)+z_pKH(0,0,3)+z_p\varepsilon\{2\alpha H(1,0,3)+2\beta kH(0,1,3) - H(2,0,3)-kH(0,2,3)\}$$

$$\tilde{\phi}_2 = H(1,0,1)+z_pKH(1,0,3)+z_p\varepsilon\{2\alpha H(2,0,3)+2\beta kH(1,1,3) - H(3,0,3)-kH(1,2,3)\}$$

and

$$\tilde{\phi}_3 = H(0,1,1)+z_pKH(0,1,3)+z_p\varepsilon\{2\alpha H(1,1,3)+2\beta kH(0,2,3) - H(2,1,3)-kH(0,3,3)\}$$

Then velocity formula is obtained by taking derivatives of Equation E.3 as

$$V_x = S_k\{a_k\,\partial\phi_1/\partial x + b_k\partial\phi_2/\partial x + c_k\partial\phi_3/\partial x\}$$
$$V_y = S_k\{a_k\,\partial\phi_1/\partial y + b_k\partial\phi_2/\partial y + c_k\partial\phi_3/\partial y\} \qquad (E.4)$$
$$V_z = S_k\{a_k\,\partial\phi_1/\partial z + b_k\partial\phi_2/\partial z + c_k\partial\phi_3/\partial z\}$$

where

$$\partial\phi_1/\partial x = \underline{-H(1,0,3)} - 3z_p\varepsilon[\{H(3,0,5)-2\alpha H(2,0,5)\} + k\{H(3,0,5)-2\beta H(2,0,5)\}] \qquad (E.5)$$

$$\partial\phi_1/\partial y = \underline{-H(0,1,3)} - 3z_p\varepsilon[\{H(2,1,5)-2\alpha H(1,1,5)\} + k\{H(0,3,5)-2\beta H(0,2,5)\}] - 3z_pKH(0,1,5) \qquad (E.6)$$

$$\partial\phi_1/\partial z = -z_p\underline{H(0,0,3)} - 3z_p^2\varepsilon[\{H(2,0,5)-2\alpha H(1,0,5)\} + k\{H(0,2,5)-2\beta H(0,1,5)\}] - 3z_p^2 KH(0,0,5) + KH(0,0,3) - \varepsilon[\{H(2,0,3)-2\alpha H(1,0,3)\} + k\{H(0,2,3)-2\beta H(0,1,3)\}] \quad (E.7)$$

$$\partial\phi_2/\partial x = \underline{-xH(1,0,3) + H(2,0,3)} + 3z_p K\{H(2,0,5) -xH(1,0,5)\} + 3z_p[\Sigma 2\alpha\{H(3,0,5)-xH(2,0,5)\} +2\beta k\{H(2,1,5)-xH(1,1,5)\}-\{H(4,0,5)-xH(3,0,5)\} -k\{H(2,2,5)-xH(1,2,5)\}] \quad (E.8)$$

$$\partial\phi_2/\partial y = \underline{-xH(0,1,3) + H(1,1,3)} + 3z_p K\{H(1,1,5) -xH(0,1,5)\} + 3z_p\varepsilon[2\alpha\{H(2,1,5)-xH(1,1,5)\} +2\beta k\{H(1,2,5)-xH(0,2,5)\}-\{H(3,1,5)-xH(2,1,5)\} -k\{H(1,3,5)-xH(0,3,5)\}] \quad (E.9)$$

$$\partial\phi_2/\partial z = z_p\underline{\{-xH(0,0,3)+H(1,0,3)\}} + 3z_p^2 K\{H(1,0,5) -xH(0,0,5)\} + 3z_p^2\varepsilon[2\alpha\{H(2,0,5)-xH(1,0,5)\} +2\beta k\{H(1,1,5)-xH(0,1,5)\}-\{H(3,0,5)-xH(2,0,5)\} -k\{H(1,2,5)-xH(0,2,5)\}] + 3z_p^2 K\{H(1,0,5)-xH(0,0,5)\} - K\{H(1,0,3)-xH(0,0,3)\} - \varepsilon[2\alpha\{H(2,0,3)-xH(1,0,3)\} + 2\beta k\{H(1,1,3\}-xH(0,1,3)\} - \{H(3,0,3)-xH(2,0,3)\} - k\{H(1,2,3)-xH(0,2,3)\}] \quad (E.10)$$

$$\partial\phi_3/\partial x = \underline{-yH(1,0,3) + H(1,1,3)} + 3z_p K\{H(1,1,5) -yH(1,0,5)\} + 3z_p\varepsilon[2\alpha\{H(2,1,5)-yH(2,0,5)\} +2\beta k\{H(1,2,5)-yH(1,1,5)\}-\{H(3,1,5)-yH(3,0,5)\} -k\{H(1,3,5)-yH(1,2,5)\}] \quad (E.11)$$

$$\partial\phi_3/\partial y = \underline{-yH(0,1,3) + H(0,2,3)} + 3z_p K\{H(0,2,5) -yH(0,1,5)\} + 3z_p\varepsilon[2\alpha\{H(1,2,5)-yH(1,1,5)\} +2\beta k\{H(0,3,5)-yH(0,2,5)\}-\{H(2,2,5)-yH(2,1,5)\} \quad (E.12)$$

$$
\begin{aligned}
&\quad -k\{H(0,4,5)-yH(0,3,5)\}] \\
\partial\phi_3/\partial z &= z_p\underline{\{-yH(0,0,3)+H(0,1,3)\}} + 3z_p^2K\{H(0,1,5) \\
&\quad -yH(0,0,5)\} + 3z_p^2\varepsilon[2\alpha\{H(1,1,5)-yH(1,0,5)\} \\
&\quad +2\beta k\{H(0,2,5)-yH(0,1,5)\}-\{H(2,1,5)-yH(2,0,5)\} \\
&\quad -k\{H(0,3,5)-yH(0,2,5)\}] \\
&\quad - K\{H(0,1,3)-yH(0,0,3)\} - \varepsilon[2\alpha\{H(1,1,3)-yH(1,0,3)\} \\
&\quad + 2\beta k\{H(0,2,3\}-yH(0,1,3)\} - \{H(2,1,3)-yH(2,0,3)\} \\
&\quad - k\{H(0,3,3)-yH(0,2,3)\}]
\end{aligned}
\tag{E.13}
$$

In the equations above the underlined parts are the formulas for the planar element when ε is equal to zero.

E.2 GEOMETRIC RELATIONSHIPS

We give some relationships among variables in the formula referring to Figure 50 as follows:

$$d_{12} = \sqrt{(\xi_2-\xi_1)^2+(\eta_2-\eta_1)^2}$$

$$S_{12}= (\eta_2- \eta_1)/d_{12}$$

$$C_{12}= (\xi_2- \xi_1)/d_{12}$$

$$S_{12}= -u_{\xi 12}= \cos\theta_P \ , \ C_{12}= u_{\eta 12}= \sin\theta_P$$

$$x-\xi = h\cos\theta_P - \lambda\sin\theta_P$$

$$y-\eta =-h\sin\theta_P - \lambda\cos\theta_P$$

or

$$h = (x-\xi)\cos\theta_P - (y-\eta)\sin\theta_P$$

$$\lambda =-(x-\xi)\sin\theta_P - (y-\eta)\cos\theta_P$$

E.3 FORMULA, H(M,N,K)

We define some formula in the following way.

$$F(M,N,K) = \int_1^2 \{(x-\xi)^M (y-\eta)^N / \rho^K\} ds \tag{E.14}$$

$$E(M,N,K) = \{(x-\xi)^M (y-\eta)^N / \rho^K\}\Big|_1^2 \tag{E.15}$$

With the use of Equation E.14, the following can be shown.

$$\frac{\partial H(M,N,K)}{\partial x} = MH(M-1,N,K) - KH(M+1,N,K+2) \tag{E.16}$$

$$\frac{\partial H(M,N,K)}{\partial y} = NH(M,N-1,K) - KH(M,N+1,K+2) \tag{E.17}$$

$$\frac{\partial H(M,N,K)}{\partial z} = -Kz_p H(M,N,K+2) \tag{E.18}$$

$$H(M+2,N,K) + H(M,N+2,K) + z_p^2 H(M,N,K) = H(M,N,K-2) \tag{E.19}$$

$$(K-2)H(M,N,K) = (M-1)H(M-2,N,K-2) + \Sigma\nu_\xi F(M-1,N,K-2) \tag{E.20}$$

$$(K-2)H(M,N,K) = (N-1)H(M,N-2,K-2) + \Sigma\nu_\eta F(M,N-1,K-2) \tag{E.21}$$

$$F(M+2,N,K) + F(M,N+2,K) + z_p^2 F(M,N,K) = F(M,N,K-2) \tag{E.22}$$

$$\nu_\xi F(M+1,N,K) + \nu_\eta F(M,N+1,K) = -hF(M,N,K) \tag{E.23}$$

$$(K-2)\nu_\xi F(M,N+1,K) - (K-2)\nu_\eta F(M+1,N,K) = N\nu_\xi F(M,N-1,K-2)$$
$$-M\nu_\eta F(M-1,N,K-2) - E(M,N,K-2) \tag{E.24}$$

In these equations, (K-2) may be negative, and M and N may be unity. We may obtain some other relationships by using the above equations as follows:

$$F(M,N+1,K) = -\nu_\eta hF(M,N,K) + \{N\nu_\xi F(M,N-1,K-2)$$
$$-M\nu_\eta F(M-1,N,K-2) - E(M,N,K-2)\}\nu_\xi/(K-2) \tag{E.25}$$

$$F(M+1,N,K) = \{(K-2)\nu_{\xi}F(M,N+1,K) - N\nu_{\eta}F(M,N-1,K-2) + M\nu_{\eta}F(M-1,N,K-2) + E(M,N,K-2)\}/\{(K-2)\nu_{\eta}\} \quad (E.26)$$

and

$$(K-2)z_p^2H(M,N,K) = (K-4-M-N)H(M,N,K-2) + \Sigma hF(M,N,K-2) \quad (E.27)$$

It must be noted that in the discussion above, the formulas F(M,N,K) and E(M,N,K) have three components. In other words, they depend upon the nodal indices even though they do not show up explicitly in the expression. The other notations may be referred to Figure 50.

APENDIX F. MULTIPOLE EXPANSION

Here we develop the velocity formula by expanding the exact velocity formula for the far-field. We begin with the potential formula, expanding the integrand first. Let

$$f(\xi,\eta,\zeta:x,y,z) = \frac{1}{r} \tag{F.1}$$

where

$$r = \sqrt{(x-\xi)^2+(y-\eta)^2+(z-\zeta)^2}$$

By Taylor series,

$$f(\xi,\eta:x,y,z) = f|_0 + \frac{\partial f}{\partial \xi}|_0 \tilde{\xi} + \frac{\partial f}{\partial \eta}|_0 \tilde{\eta} + \frac{1}{2}\{\frac{\partial^2 f}{\partial \xi^2}|_0 \tilde{\xi}^2 + 2\frac{\partial^2 f}{\partial \xi \partial \eta}|_0 \tilde{\xi}\tilde{\eta} + \frac{\partial^2 f}{\partial \eta^2}|_0 \tilde{\eta}^2\} + \text{higher order terms} \tag{F.2}$$

where

$$\tilde{\xi} = \xi - \xi_0, \quad \tilde{\eta} = \eta - \eta_0$$

$$\frac{\partial f}{\partial \xi} = -\frac{(\xi-x)+(\zeta-z)\partial\zeta/\partial\xi}{r^3}$$

$$\frac{\partial f}{\partial \eta} = -\frac{(\eta-y)+(\zeta-z)\partial\zeta/\partial\eta}{r^3}$$

$$\frac{\partial^2 f}{\partial \xi^2} = -\frac{1+(\partial\zeta/\partial\xi)^2+(\zeta-z)\partial^2\zeta/\partial\xi^2}{r^3} + 3\frac{\{(\xi-x)+(\zeta-z)\partial\zeta/\partial\xi\}^2}{r^5}$$

$$\frac{\partial^2 f}{\partial \xi \partial \eta} = -\frac{(\partial\zeta/\partial\xi)(\partial\zeta/\partial\eta)}{r^3} + \frac{3\{(\xi-x)+(\zeta-z)\partial\zeta/\partial\xi\}\{(\eta-y)+(\zeta-z)\partial\zeta/\partial\eta\}}{r^5}$$

and

$$\frac{\partial^2 f}{\partial \eta^2} = -\frac{1+(\partial\zeta/\partial\eta)^2+(\zeta-z)\partial^2\zeta/\partial\eta^2}{r^3} + 3\frac{\{(\eta-y)+(\zeta-z)\partial\zeta/\partial\eta\}^2}{r^5}$$

In Equation F.2 the subscript '0' stands for 'evaluated at a point "0" on the element(center of expansion). Since the function f depends upon x,y,and z as well as ξ and η, the derivatives of function f with respect to ξ,η can also be expressed in terms of those with respect to x,y,and z. The relationships are given in the following. Let us define

$$W = f \ , \ \frac{\partial f}{\partial x} \equiv W_x \ , \ \frac{\partial f}{\partial y} \equiv W_y, \text{ etc.}$$

Then,

$$\frac{\partial f}{\partial \xi} = -(W_x + \frac{\partial \zeta}{\partial x}W_z)$$

$$\frac{\partial f}{\partial \eta} = -(W_y + \frac{\partial \zeta}{\partial \eta}W_z)$$

$$\frac{\partial^2 f}{\partial \xi^2} = W_{xx}+(\frac{\partial \zeta}{\partial \xi})^2 W_{zz} - \frac{\partial^2 \zeta}{\partial \xi^2}W_z + 2\frac{\partial \zeta}{\partial \xi}W_{xz}$$

$$\frac{\partial^2 f}{\partial \xi \partial \eta} = W_{xy}+ (\frac{\partial \zeta \partial \zeta}{\partial \xi \partial \eta})W_{zz} + \frac{\partial \zeta}{\partial \xi}W_{yz} + \frac{\partial \zeta}{\partial \eta}W_{xz}$$

$$\frac{\partial^2 f}{\partial \eta^2} = W_{yy}+ (\frac{\partial \zeta}{\partial \eta})^2 W_{zz} - \frac{\partial^2 \zeta}{\partial \eta^2}W_z + 2\frac{\partial \zeta}{\partial \eta}W_{yz}$$

Thus, the potential becomes by substituting Equation F.2 into the potential formula and evaluating the integral

$$\phi = S_i(a_i\phi_1 + b_i\phi_2 + c_i\phi_3) \tag{F.3}$$

where

$$\begin{aligned}\phi_1 = {} & WI_{00} - \{(W_x + \frac{\partial\zeta}{\partial\xi}W_z)I_{10} + (W_y + \frac{\partial\zeta}{\partial\eta}W_z)I_{01}\} \\ & + \frac{1}{2}[\{W_{xx} + (\frac{\partial\zeta}{\partial\xi})^2 W_{zz} - \frac{\partial^2\zeta}{\partial\xi^2}W_z + 2\frac{\partial\zeta}{\partial\xi}W_{xz}\}I_{20} \\ & + 2\{W_{xy} + (\frac{\partial\zeta}{\partial\xi}\frac{\partial\zeta}{\partial\eta})W_{zz} + \frac{\partial\zeta}{\partial\xi}W_{yz} + \frac{\partial\zeta}{\partial\eta}W_{xz}\}I_{11} \\ & + \{W_{yy} + (\frac{\partial\zeta}{\partial\eta})^2 W_{zz} - \frac{\partial^2\zeta}{\partial\eta^2}W_z + 2\frac{\partial\zeta}{\partial\eta}W_{yz}\}I_{02}]\end{aligned}$$

$$\begin{aligned}\phi_2 = {} & \xi_0\phi_1 + WI_{10} - \{(W_x + \frac{\partial\zeta}{\partial\xi}W_z)I_{20} + (W_y + \frac{\partial\zeta}{\partial\eta}W_z)I_{11}\} \\ & + \frac{1}{2}[\{W_{xx} + (\frac{\partial\zeta}{\partial\xi})^2 W_{zz} - \frac{\partial^2\zeta}{\partial\xi^2}W_z + 2\frac{\partial\zeta}{\partial\xi}W_{xz}\}I_{30} \\ & + 2\{W_{xy} + (\frac{\partial\zeta}{\partial\xi}\frac{\partial\zeta}{\partial\eta})W_{zz} + \frac{\partial\zeta}{\partial\xi}W_{yz} + \frac{\partial\zeta}{\partial\eta}W_{xz}\}I_{21} \\ & + \{W_{yy} + (\frac{\partial\zeta}{\partial\eta})^2 W_{zz} - \frac{\partial^2\zeta}{\partial\eta^2}W_z + 2\frac{\partial\zeta}{\partial\eta}W_{yz}\}I_{12}]\end{aligned}$$

$$\begin{aligned}\phi_3 = {} & \eta_0\phi_1 + WI_{01} - \{(W_x + \frac{\partial\zeta}{\partial\xi}W_z)I_{11} + (W_y + \frac{\partial\zeta}{\partial\eta}W_z)I_{02}\} \\ & + \frac{1}{2}[\{W_{xx} + (\frac{\partial\zeta}{\partial\xi})^2 W_{zz} - \frac{\partial^2\zeta}{\partial\xi^2}W_z + 2\frac{\partial\zeta}{\partial\xi}W_{xz}\}I_{21} \\ & + 2\{W_{xy} + (\frac{\partial\zeta}{\partial\xi}\frac{\partial\zeta}{\partial\eta})W_{zz} + \frac{\partial\zeta}{\partial\xi}W_{yz} + \frac{\partial\zeta}{\partial\eta}W_{xz}\}I_{12} \\ & + \{W_{yy} + (\frac{\partial\zeta}{\partial\eta})^2 W_{zz} - \frac{\partial^2\zeta}{\partial\eta^2}W_z + 2\frac{\partial\zeta}{\partial\eta}W_{yz}\}I_{03}]\end{aligned}$$

and

$$I_{MN} \equiv \int_\Sigma \int \tilde{\xi}^M \tilde{\eta}^N \, d\Sigma \tag{F.4}$$

Then the components of potential derivatives are obtained in the following.

$$\partial\phi_1/\partial x = W_x I_{00} - \{(W_{xx} + \frac{\partial\zeta}{\partial\xi}W_{xz})I_{10} + (W_{xy} + \frac{\partial\zeta}{\partial\eta}W_{xz})I_{01}\}$$
$$+ \frac{1}{2}[\{W_{xxx} + (\frac{\partial\zeta}{\partial\xi})^2 W_{xzz} - \frac{\partial^2\zeta}{\partial\xi^2}W_{xz} + 2\frac{\partial\zeta}{\partial\xi}W_{xxz}\}I_{20}$$
$$+ 2\{W_{xxy} + (\frac{\partial\zeta\partial\zeta}{\partial\xi\partial\eta})W_{xzz} + \frac{\partial\zeta}{\partial\xi}W_{xyz} + \frac{\partial\zeta}{\partial\eta}W_{xxz}\}I_{11}$$
$$+ \{W_{xyy} + (\frac{\partial\zeta}{\partial\eta})^2 W_{xzz} - \frac{\partial^2\zeta}{\partial\eta^2}W_{xz} + 2\frac{\partial\zeta}{\partial\eta}W_{xyz}\}I_{02}]$$

$$\partial\phi_2/\partial x = \xi_0\partial\phi_1/\partial x + W_x I_{10} - \{(W_{xx} + \frac{\partial\zeta}{\partial\xi}W_{xz})I_{20} + (W_{xy} + \frac{\partial\zeta}{\partial\eta}W_{xz})I_{11}\}$$
$$+ \frac{1}{2}[\{W_{xxx} + (\frac{\partial\zeta}{\partial\xi})^2 W_{xzz} - \frac{\partial^2\zeta}{\partial\xi^2}W_{xz} + 2\frac{\partial\zeta}{\partial\xi}W_{xxz}\}I_{30}$$
$$+ 2\{W_{xxy} + (\frac{\partial\zeta\partial\zeta}{\partial\xi\partial\eta})W_{xzz} + \frac{\partial\zeta}{\partial\xi}W_{xyz} + \frac{\partial\zeta}{\partial\eta}W_{xxz}\}I_{21}$$
$$+ \{W_{xyy} + (\frac{\partial\zeta}{\partial\eta})^2 W_{xzz} - \frac{\partial^2\zeta}{\partial\eta^2}W_{xz} + 2\frac{\partial\zeta}{\partial\eta}W_{xyz}\}I_{12}]$$

$$\partial\phi_3/\partial x = \eta_0\partial\phi_1/\partial x + W_x I_{01} - \{(W_{xx} + \frac{\partial\zeta}{\partial\xi}W_{xz})I_{11} + (W_{xy} + \frac{\partial\zeta}{\partial\eta}W_{xz})\ I_{02}\}$$
$$+ \frac{1}{2}[\{W_{xxx} + (\frac{\partial\zeta}{\partial\xi})^2 W_{xzz} - \frac{\partial^2\zeta}{\partial\xi^2}W_{xz} + 2\frac{\partial\zeta}{\partial\xi}W_{xxz}\}I_{21}$$
$$+ 2\{W_{xxy} + (\frac{\partial\zeta\partial\zeta}{\partial\xi\partial\eta})W_{xzz} + \frac{\partial\zeta}{\partial\xi}W_{xyz} + \frac{\partial\zeta}{\partial\eta}W_{xxz}\}I_{12}$$
$$+ \{W_{xyy} + (\frac{\partial\zeta}{\partial\eta})^2 W_{xzz} - \frac{\partial^2\zeta}{\partial\eta^2}W_{xz} + 2\frac{\partial\zeta}{\partial\eta}W_{xyz}\}I_{03}]$$

$$\partial\phi_1/\partial y = W_y I_{00} - \{(W_{xy} + \frac{\partial\zeta}{\partial\xi}W_{yz})I_{10} + (W_{yy} + \frac{\partial\zeta}{\partial\eta}W_{yz})I_{01}\}$$
$$+ \frac{1}{2}[\{W_{xxy} + (\frac{\partial\zeta}{\partial\xi})^2 W_{yzz} - \frac{\partial^2\zeta}{\partial\xi^2}W_{yz} + 2\frac{\partial\zeta}{\partial\xi}W_{xyz}\}I_{20}$$
$$+ 2\{W_{xyy} + (\frac{\partial\zeta\partial\zeta}{\partial\xi\partial\eta})W_{yzz} + \frac{\partial\zeta}{\partial\xi}W_{yyz} + \frac{\partial\zeta}{\partial\eta}W_{xyz}\}I_{11}$$
$$+ \{W_{yyy} + (\frac{\partial\zeta}{\partial\eta})^2 W_{yzz} - \frac{\partial^2\zeta}{\partial\eta^2}W_{yz} + 2\frac{\partial\zeta}{\partial\eta}W_{yyz}\}I_{02}]$$

$$\partial\phi_2/\partial y = \xi_0\partial\phi_1/\partial y + W_y I_{10} - \{(W_{xy} + \frac{\partial\zeta}{\partial\xi}W_{yz})I_{20} + (W_{yy} + \frac{\partial\zeta}{\partial\eta}W_{yz})I_{11}\}$$
$$+ \frac{1}{2}[\{W_{xxy} + (\frac{\partial\zeta}{\partial\xi})^2 W_{yzz} - \frac{\partial^2\zeta}{\partial\xi^2}W_{yz} + 2\frac{\partial\zeta}{\partial\xi}W_{xyz}\}I_{30}$$

$$+ 2\{W_{xyy} + (\frac{\partial\zeta\partial\zeta}{\partial\xi\partial\eta})W_{yzz} + \frac{\partial\zeta}{\partial\xi}W_{yyz} + \frac{\partial\zeta}{\partial\eta}W_{xyz}\}I_{21}$$
$$+ \{W_{yyy} + (\frac{\partial\zeta}{\partial\eta})^2 W_{yzz} - \frac{\partial^2\zeta}{\partial\eta^2}W_{yz} + 2\frac{\partial\zeta}{\partial\eta}W_{yyz}\}I_{12}]$$

$$\partial\phi_3/\partial y = \eta_0\partial\phi_1/\partial y + W_y I_{01} - \{(W_{xy} + \frac{\partial\zeta}{\partial\xi}W_{yz})I_{11} + (W_{yy} + \frac{\partial\zeta}{\partial\eta}W_{yz})I_{02}\}$$
$$+ \frac{1}{2}[\{W_{xxy} + (\frac{\partial\zeta}{\partial\xi})^2 W_{yzz} - \frac{\partial^2\zeta}{\partial\xi^2}W_{yz} + 2\frac{\partial\zeta}{\partial\xi}W_{xyz}\}I_{21}$$
$$+ 2\{W_{xyy} + (\frac{\partial\zeta\partial\zeta}{\partial\xi\partial\eta})W_{yzz} + \frac{\partial\zeta}{\partial\xi}W_{yyz} + \frac{\partial\zeta}{\partial\eta}W_{xyz}\}I_{12}$$
$$+ \{W_{yyy} + (\frac{\partial\zeta}{\partial\eta})^2 W_{yzz} - \frac{\partial^2\zeta}{\partial\eta^2}W_{yz} + 2\frac{\partial\zeta}{\partial\eta}W_{yyz}\}I_{03}]$$

$$\partial\phi_1/\partial z = W_z I_{00} - \{(W_{xz} + \frac{\partial\zeta}{\partial\xi}W_{zz})I_{10} + (W_{yz} + \frac{\partial\zeta}{\partial\eta}W_{zz})I_{01}\}$$
$$+ \frac{1}{2}[\{W_{xxz} + (\frac{\partial\zeta}{\partial\xi})^2 W_{zzz} - \frac{\partial^2\zeta}{\partial\xi^2}W_{zz} + 2\frac{\partial\zeta}{\partial\xi}W_{xzz}\}I_{20}$$
$$+ 2\{W_{xyz} + (\frac{\partial\zeta\partial\zeta}{\partial\xi\partial\eta})W_{zzz} + \frac{\partial\zeta}{\partial\xi}W_{yzz} + \frac{\partial\zeta}{\partial\eta}W_{xzz}\}I_{11}$$
$$+ \{W_{yyz} + (\frac{\partial\zeta}{\partial\eta})^2 W_{zzz} - \frac{\partial^2\zeta}{\partial\eta^2}W_{zz} + 2\frac{\partial\zeta}{\partial\eta}W_{yzz}\}I_{02}]$$

$$\partial\phi_2/\partial z = \xi_0\partial\phi_1/\partial z + W_z I_{10} - \{(W_{xz} + \frac{\partial\zeta}{\partial\xi}W_{zz})I_{20} + (W_{yz} + \frac{\partial\zeta}{\partial\eta}W_{zz})I_{11}\}$$
$$+ \frac{1}{2}[\{W_{xxz} + (\frac{\partial\zeta}{\partial\xi})^2 W_{zzz} - \frac{\partial^2\zeta}{\partial\xi^2}W_{zz} + 2\frac{\partial\zeta}{\partial\xi}W_{xzz}\}I_{30}$$
$$+ 2\{W_{xyz} + (\frac{\partial\zeta\partial\zeta}{\partial\xi\partial\eta})W_{zzz} + \frac{\partial\zeta}{\partial\xi}W_{yzz} + \frac{\partial\zeta}{\partial\eta}W_{xzz}\}I_{21}$$
$$+ \{W_{yyz} + (\frac{\partial\zeta}{\partial\eta})^2 W_{zzz} - \frac{\partial^2\zeta}{\partial\eta^2}W_{zz} + 2\frac{\partial\zeta}{\partial\eta}W_{yzz}\}I_{12}]$$

$$\partial\phi_3/\partial z = \eta_0\partial\phi_1/\partial z + W_z I_{01} - \{(W_{xz} + \frac{\partial\zeta}{\partial\xi}W_{zz})I_{11} + (W_{yz} + \frac{\partial\zeta}{\partial\eta}W_{zz})I_{02}\}$$
$$+ \frac{1}{2}[\{W_{xxz} + (\frac{\partial\zeta}{\partial\xi})^2 W_{zzz} - \frac{\partial^2\zeta}{\partial\xi^2}W_{zz} + 2\frac{\partial\zeta}{\partial\xi}W_{xzz}\}I_{21}$$
$$+ 2\{W_{xyz} + (\frac{\partial\zeta\partial\zeta}{\partial\xi\partial\eta})W_{zzz} + \frac{\partial\zeta}{\partial\xi}W_{yzz} + \frac{\partial\zeta}{\partial\eta}W_{xzz}\}I_{12}$$
$$+ \{W_{yyz} + (\frac{\partial\zeta}{\partial\eta})^2 W_{zzz} - \frac{\partial^2\zeta}{\partial\eta^2}W_{zz} + 2\frac{\partial\zeta}{\partial\eta}W_{yzz}\}I_{03}]$$

In Equation F.2, the zeroth order, first order, and second order derivative terms stand for point sources, point dipoles, and point quadrupoles, respectively. Note that when we use the centroid of the element as the center of the expansion the dipole terms become identically zero. In the above development of multipole expansion of velocity components we did not drop any terms up to second derivatives. But in order to be consistent with our assumptions (small curvature effect) the products of derivatives may be neglected.

Table 3-1

Surface Velocity at Trailing Edge		
Number of elements	Top	Bottom
20	+0.02954	-0.02954
40	-0.27155	+0.27155
80	-0.52643	+0.52643
160	-0.59926	+0.59926

* n = 1.95

Table 3-2

Surface Velocity at Trailing Edge		
Number of elements	Top	Bottom
20	-2.78794	+2.78794
40	-20.55102	+20.55102
80	-122.39677	+122.39677
160	-488.51154	+488.51154

* n = 2.0 (cusp trailing edge)

Table 3-3

SURFACE VELOCITY DISTRIBUTIONS ON A SYMMETRIC KARMAN-TREFFTZ AIRFOIL

X/C	EXACT	NEM=8	NEM=16	NEM=32	NEM=64	NEM=128
1.00000	0.00000	0.00000	0.00000	0.00000	0.00000	0.00000
0.98776	-0.85193			-0.82148	-0.84392	-0.84983
0.95352	-0.87771		-0.84549	-0.86932	-0.87552	-0.87710
0.90021	-0.89492			-0.89134	-0.89398	-0.89466
0.83110	-0.90852	-0.88256	-0.90096	-0.90689	-0.90811	-0.90840
0.74975	-0.91863			-0.91808	-0.91850	-0.91858
0.65986	-0.92397		-0.92259	-0.92410	-0.92400	-0.92397
0.56512	-0.92254			-0.92312	-0.92267	-0.92256
0.46910	-0.91163	-0.91066	-0.91369	-0.91258	-0.91185	-0.91168
0.37515	-0.88766			-0.88896	-0.88795	-0.88772
0.28639	-0.84540		-0.85101	-0.84720	-0.84580	-0.84549
0.20567	-0.77646			-0.77912	-0.77706	-0.77659
0.13552	-0.66530	-0.71267	-0.68381	-0.66980	-0.66634	-0.66554
0.07817	-0.47810			-0.48722	-0.48027	-0.47861
0.03549	-0.12380		-0.19211	-0.14919	-0.12970	-0.12525
0.00902	0.71897			0.66937	0.69867	0.71350
0.00000	2.64943	1.37148	2.07512	2.51221	2.63221	2.64818
0.00902	2.53850			2.52700	2.52841	2.53555
0.03549	2.05681		2.02857	2.03533	2.05164	2.05549
0.07817	1.80548			1.79649	1.80318	1.80490
0.13552	1.65157	1.60271	1.62888	1.64709	1.65042	1.65127
0.20567	1.54093			1.53854	1.54030	1.54076
0.28639	1.45154		1.44475	1.45021	1.45118	1.45144
0.37515	1.37347			1.37269	1.37325	1.37341
0.46910	1.30195	1.27635	1.29807	1.30144	1.30180	1.30190
0.56512	1.23471			1.23424	1.23458	1.23467
0.65986	1.17077		1.16628	1.17012	1.17061	1.17072
0.74975	1.10981			1.10867	1.10953	1.10972
0.83110	1.05168	1.01832	1.04230	1.04960	1.05116	1.05154
0.90021	0.99606			0.99211	0.99503	0.99578
0.95352	0.94152		0.90781	0.93279	0.93925	0.94089
0.98776	0.88204			0.85112	0.87393	0.87991
1.00000	0.00000	0.00000	0.00000	0.00000	0.00000	0.00000
* CIRCULATION	1.19521	1.14893	1.18036	1.19101	1.19412	1.19494

* NEM = NO. OF ELEMENTS
* ANGLE OF ATTACK = 10.0 DEG.
* PARAMETERS FOR KARMAN-TREFFTZ AIRFOIL : A=1.0, N=1.95, M=0.0688, DELTA=PI
* THE POINTS WHERE THE VELOCITIES ARE COMPUTED START FROM THE TRAILING-EDGE CLOCKWISE(FROM LOWER SURFACE).

Table 3-4

SURFACE VELOCITY DISTRUBUTIONS OVER A SYMMETRIC JOUKOWSKI AIRFOIL

X/C	EXACT	NEM=8	NEM=16	NEM=32	NEM=64	NEM=128
1.00000	-.91705	.00000	.00000	.00000	.00000	.00000
.98899	-.90385			-.89489	-.90350	-.90402
.95659	-.89548		-.88071	-.89485	-.89560	-.89540
.90463	-.89099			-.89117	-.89088	-.89081
.83590	-.88917	-.87232	-.88873	-.88939	-.88901	-.88904
.75393	-.88851			-.88884	-.88846	-.88845
.66262	-.88718		-.88862	-.88780	-.88727	-.88717
.56603	-.88291			-.88389	-.88311	-.88294
.46812	-.87283	-.87610	-.87625	-.87419	-.87313	-.87289
.37258	-.85311			-.85487	-.85350	-.85319
.28280	-.81818		-.82509	-.82048	-.81869	-.81829
.20173	-.75901			-.76226	-.75974	-.75917
.13191	-.65894	-.70260	-.68032	-.66421	-.66015	-.65922
.07543	-.48152			-.49189	-.48398	-.48210
.03392	-.12741		-.20197	-.15602	-.13404	-.12903
.00854	.76196			.70460	.73877	.75574
.00000	2.88320	1.41327	2.21204	2.72160	2.86226	2.88141
.00854	2.69031			2.67301	2.67777	2.68670
.03392	2.11682		2.07962	2.09165	2.11075	2.11527
.07543	1.81839			1.80837	1.81580	1.81773
.13191	1.63579	1.57863	1.61188	1.63111	1.63456	1.63547
.20173	1.50630			1.50405	1.50568	1.50613
.28280	1.40480		1.39868	1.40375	1.40449	1.40471
.37258	1.32002			1.31958	1.31987	1.31997
.46812	1.24654	1.22393	1.24383	1.24638	1.24646	1.24650
.56603	1.18167			1.18158	1.18161	1.18163
.66262	1.12415		1.12237	1.12398	1.12404	1.12409
.75393	1.07342			1.07315	1.07322	1.07332
.83590	1.02929	1.00429	1.02687	1.02902	1.02901	1.02913
.90463	.99169			.99145	.99148	.99148
.95659	.96058		.94408	.95956	.96059	.96047
.98899	.93580			.92624	.93531	.93593
1.00000	.91705	.00000	.00000	.00000	.00000	.00000
* CIRCUL	2.18213	2.09735	2.15463	2.17426	2.18006	2.18160

Table 3-5

Potential Difference			
	Number of elements		
	20	40	80
Computed by integration	-0.54099	-0.27155	-0.13555
Computed from surface velocity	-0.54281	-0.27237	-0.13587
Exact analytic solution	-0.54351	-0.27240	-0.13588
Circulation around an airfoil	1.62649	1.63648	1.63927

* Circulations computed by integration are same as those computed by the use of surface vorticities.
* Exact circulation around the airfoil is 1.64024.

Table 4-1 (a)

Surface Velocity Distributions on a Sphere

Angle	Exact	Basic/Source			Advanced/Source			Basic/Vorticity		
		N=48	N=120	N=224	N=48	N=120	N=224	N=48	N=120	N=224
0.00	0.0000	0.0000	0.0000	0.0000	0.0000	0.0000	0.0000	0.0000	0.0000	0.0000
22.5	0.5740			0.6109			0.6099			0.5912
30.0	0.7500		0.8048			0.8043			0.7817	
45.0	1.0607	1.1263		1.0693	1.1211		1.0790	1.1205		1.0702
60.0	1.2990		1.3026			1.2973			1.3073	
67.5	1.3858			1.4105			1.3783			1.3873
90.0	1.5000	1.4610	1.5301	1.5171	1.4265	1.4793	1.4872	1.4838	1.4933	1.4955

* N = No. of Elements, ** The elements distributed in equal spacings.

(b)

Surface Velocity Distributions on a Sphere

Angle	Exact	Basic/Vorticity		
		N=48	N=120	N=224
0.00	0.0000	0.0000	0.0000	0.0000
22.5	0.5740			0.5910
30.0	0.7500		0.7813	
45.0	1.0607	1.1214		1.0702
60.0	1.2990		1.3085	
67.5	1.3858			1.3880
90.0	1.5000	1.4947	1.4961	1.4966

* N = No. of Elements.

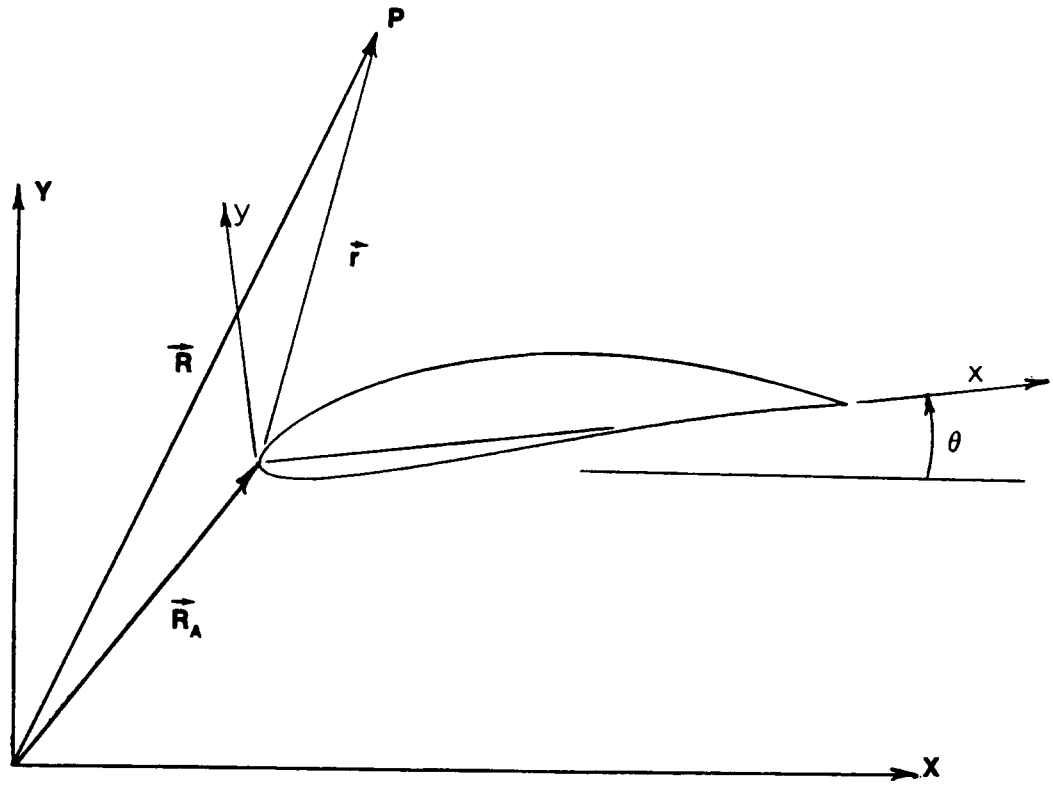

Figure 1. Fixed and moving reference frames.

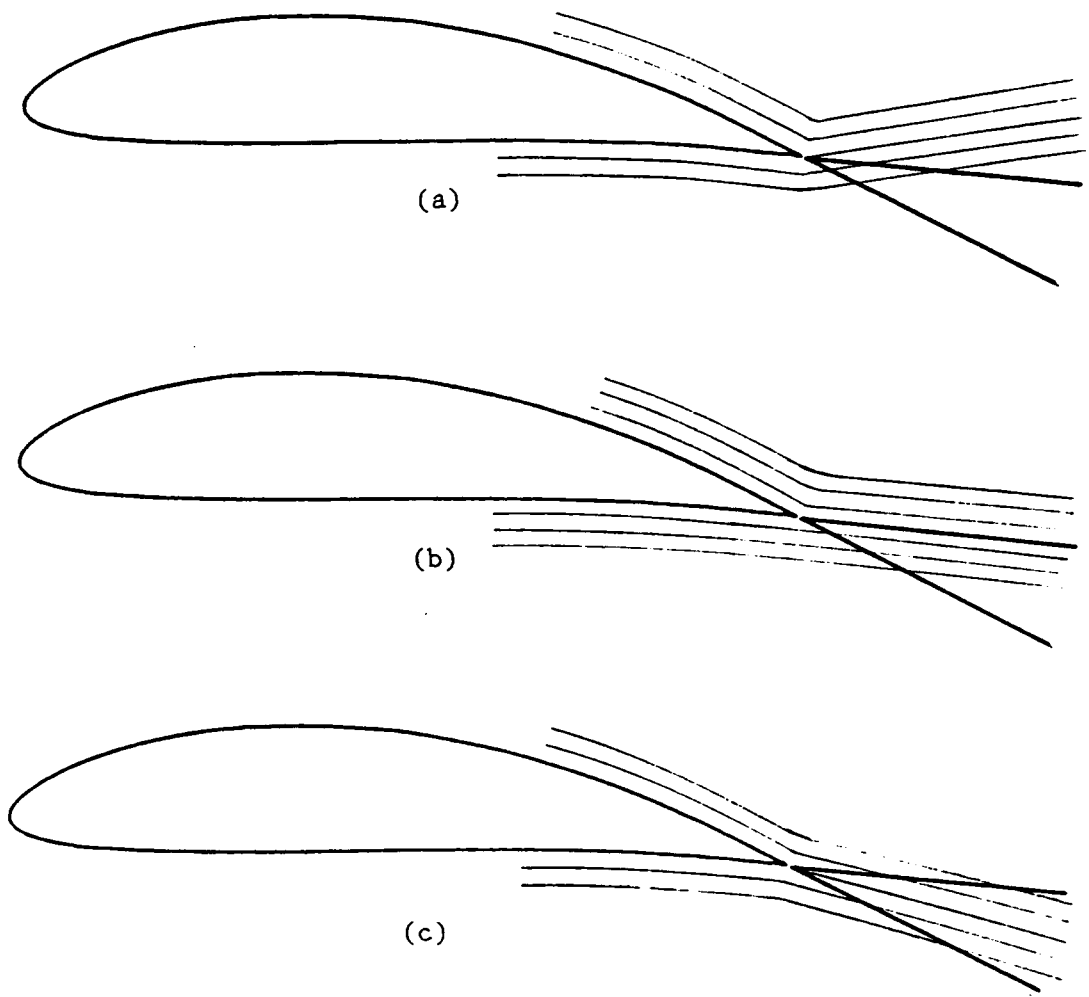

Figure 2. Conditions at the trailing-edge.

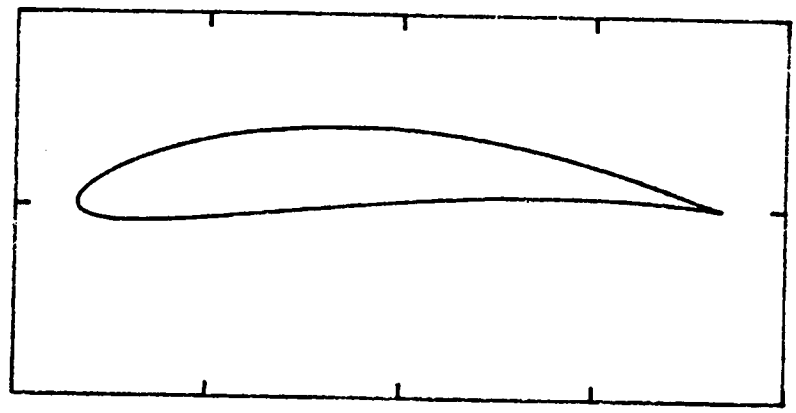

(a)

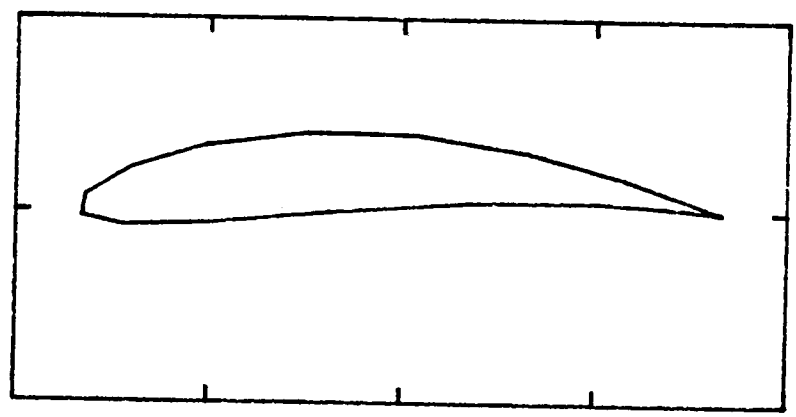

(b)

Figure 3. Discretization: (a) the actual airfoil profile (b) the airfoil after discretization.

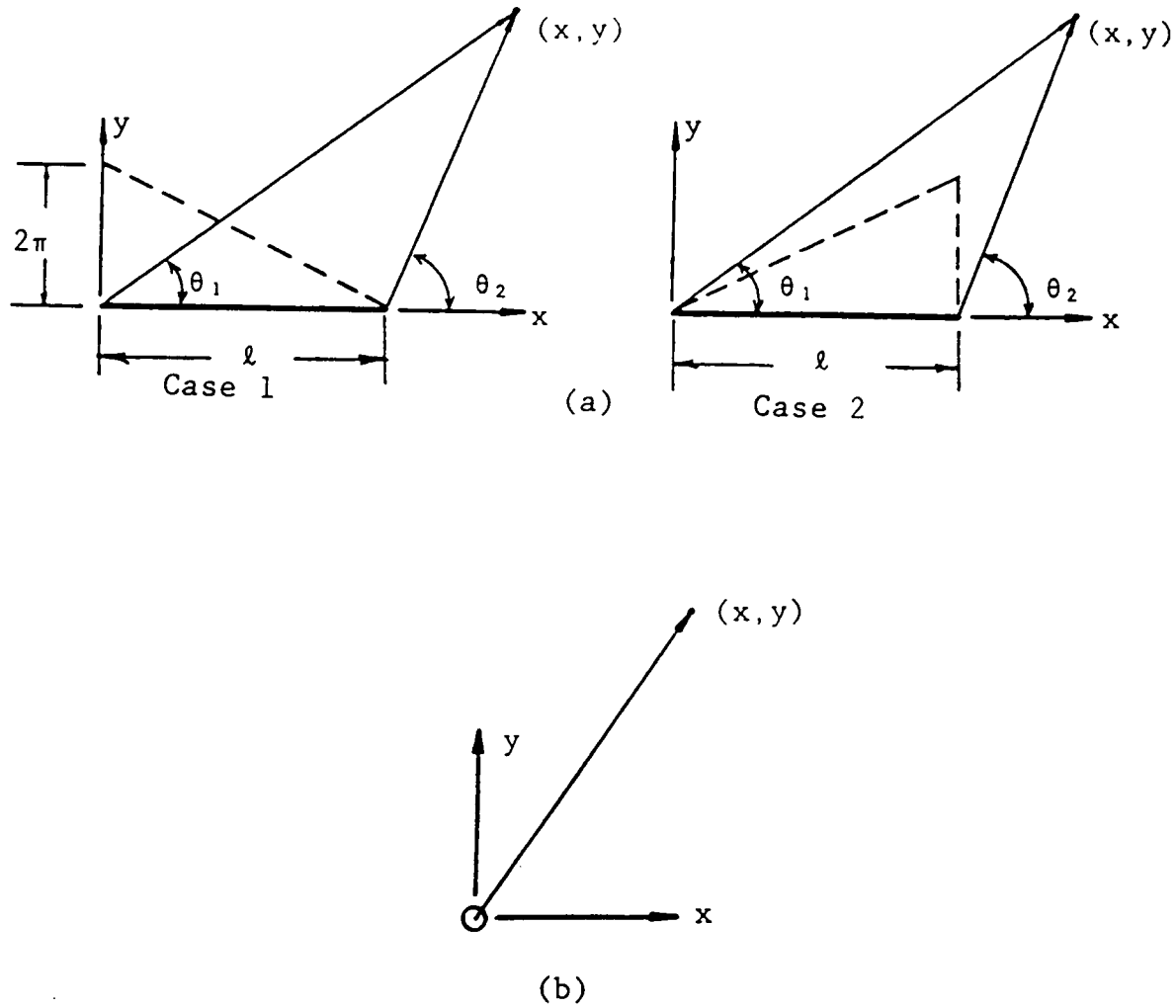

Figure 4. Nomenclature for Equations 3.17 - 3.20.

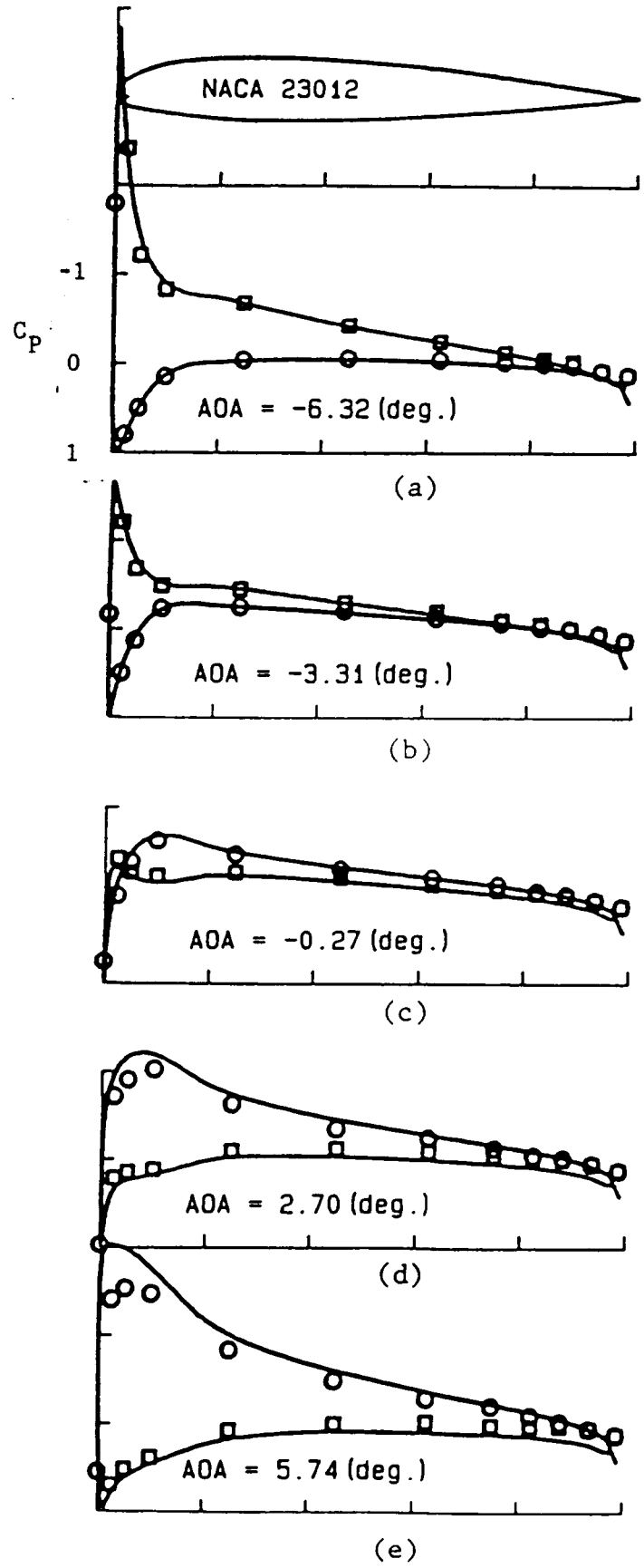

Figure 5. Pressure distribution over NACA 23012 airfoil: comparison of the predicted pressure distribution (——) with the experimental data of Wenzinger (O,□) for a NACA 23012 airfoil at various angles of attack (AOA).

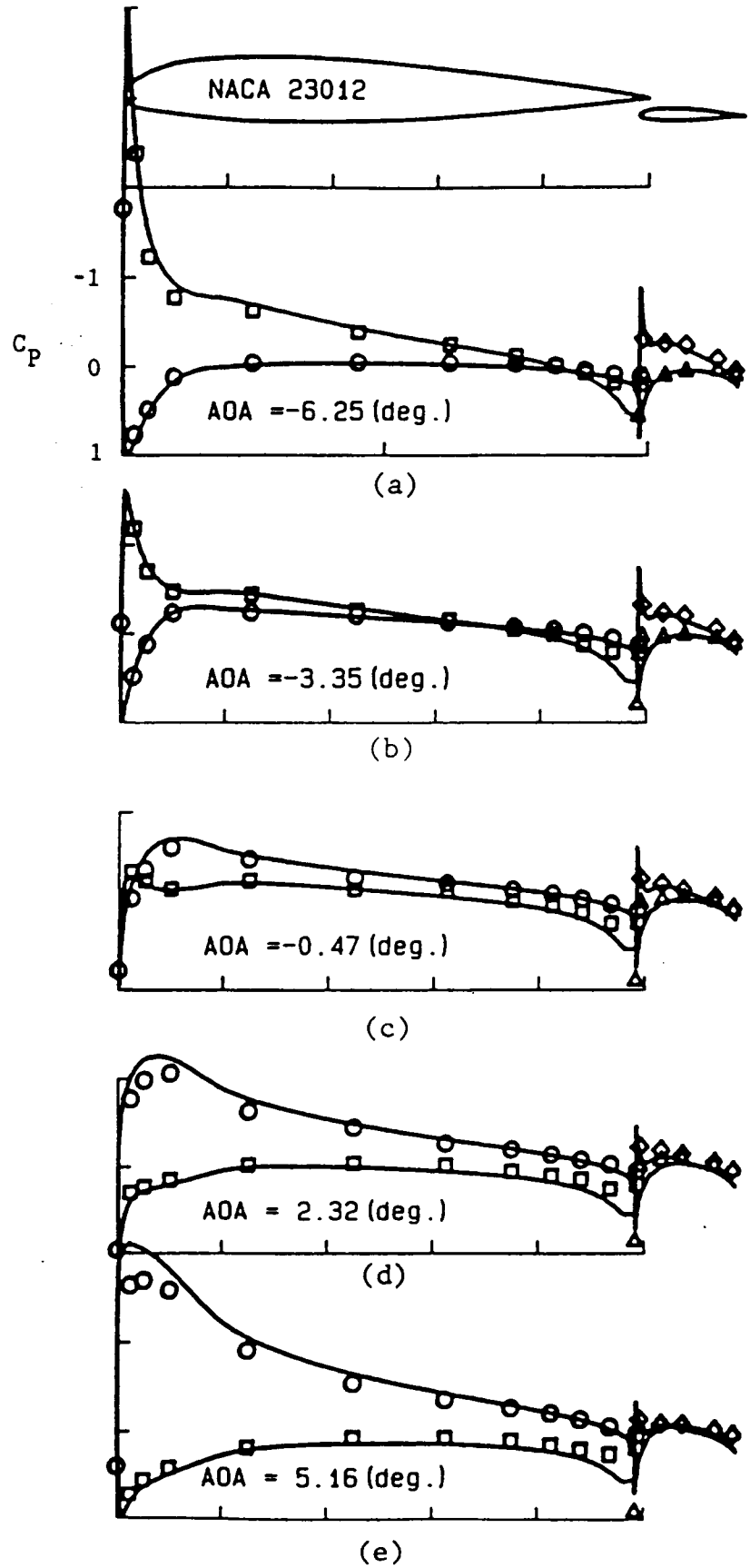

Figure 6. Pressure distribution over NACA 23012 airfoil with a flap: comparison of the predicted pressure distribution (——) with the experimental data of Wenzinger (O, □) for a NACA 23012 airfoil and flap at various angles of attack (AOA).

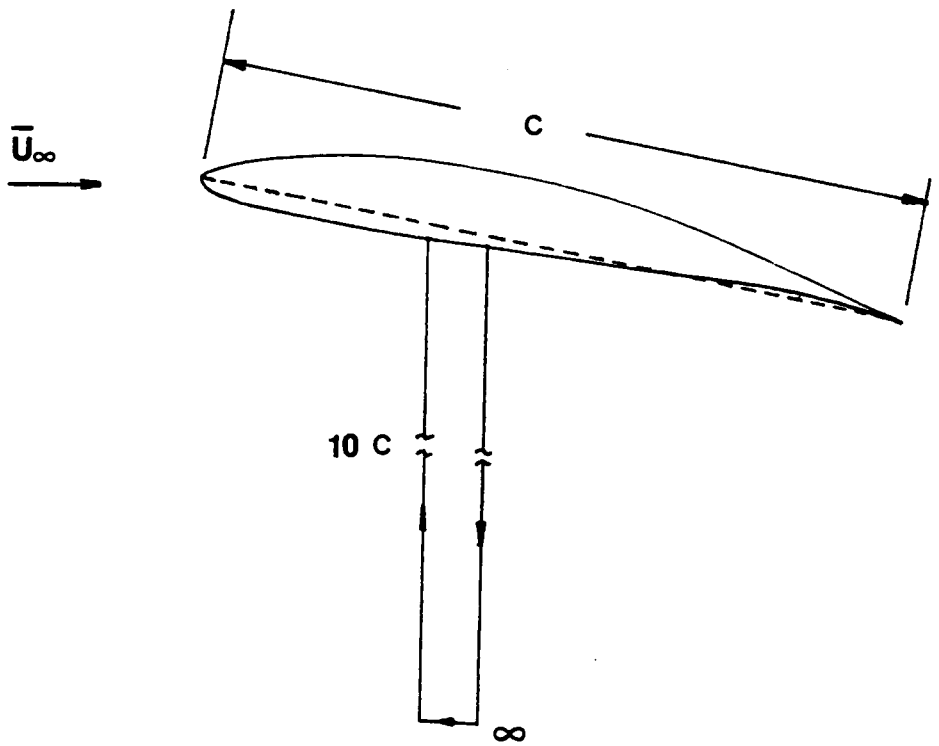

Figure 7. Position of infinity in numerical scheme.

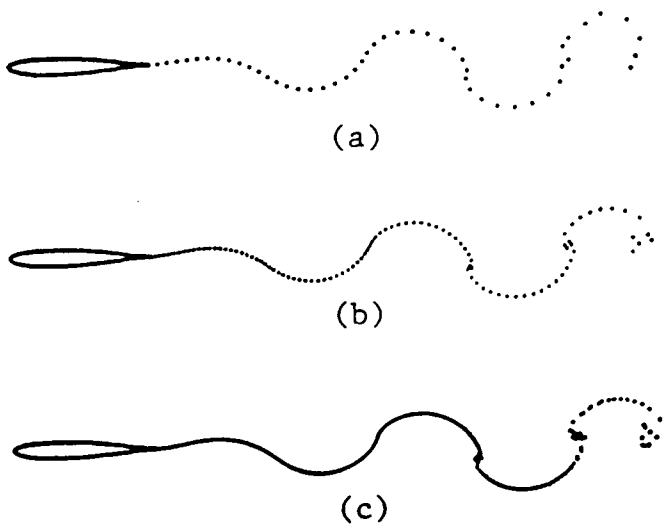

Figure 8. Wake shapes behind an oscillating airfoil: positions of vortex cores in the wake behind a sinusoidally (ω =4.3) heaving airfoil. (a) 20 elements, (b) 40 elements, and (c) 80 elements.

Figure 9. Wake shapes behind an oscillating airfoil: Positions of vortex cores behind a sinusoidally (ω =17) heaving airfoil.

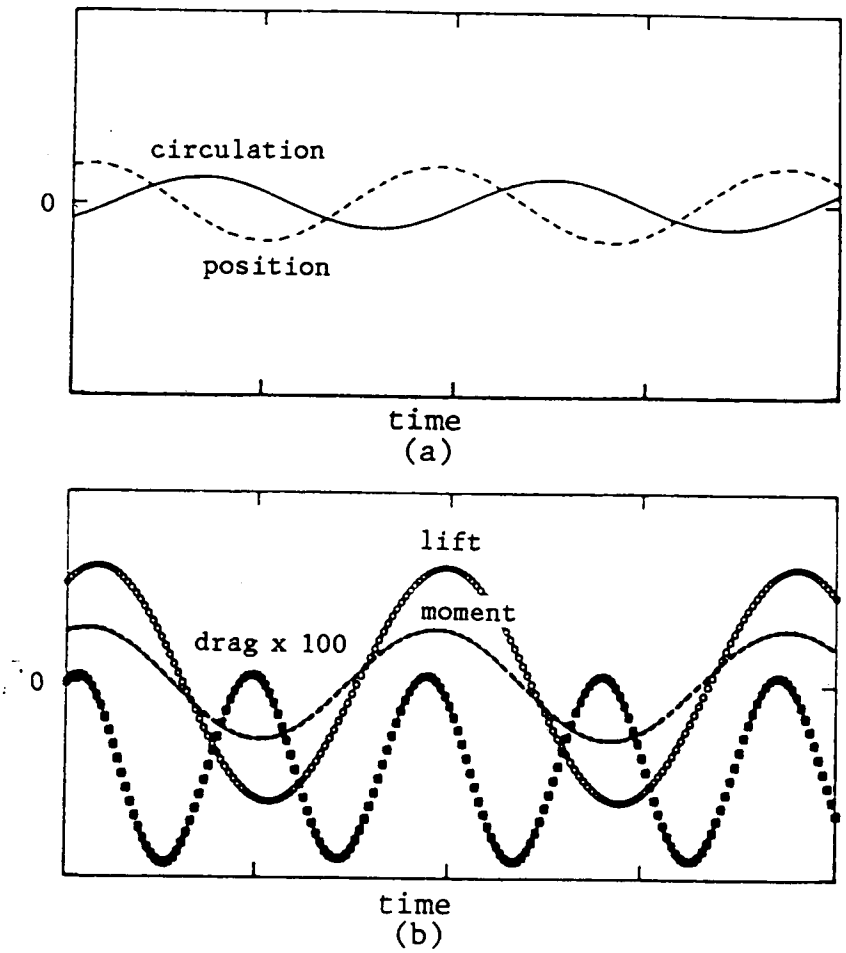

Figure 10. Aerodynamic forces with time: for the sinusoidally (ω = 4.3) heaving airfoil as functions of time.

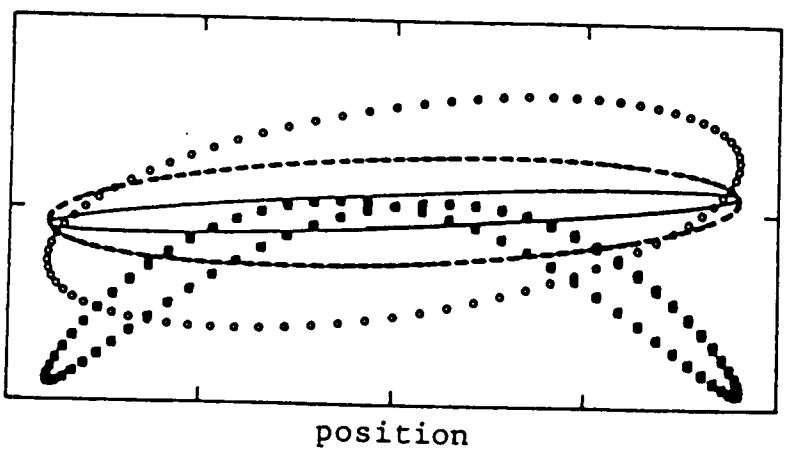

Figure 11. Hysteresis of aerodynamic forces: O lift, --- moment, □ drag x 100, and —— circulation as functions of position for the sinusoidally ($\omega = 4.3$) heaving airfoil.

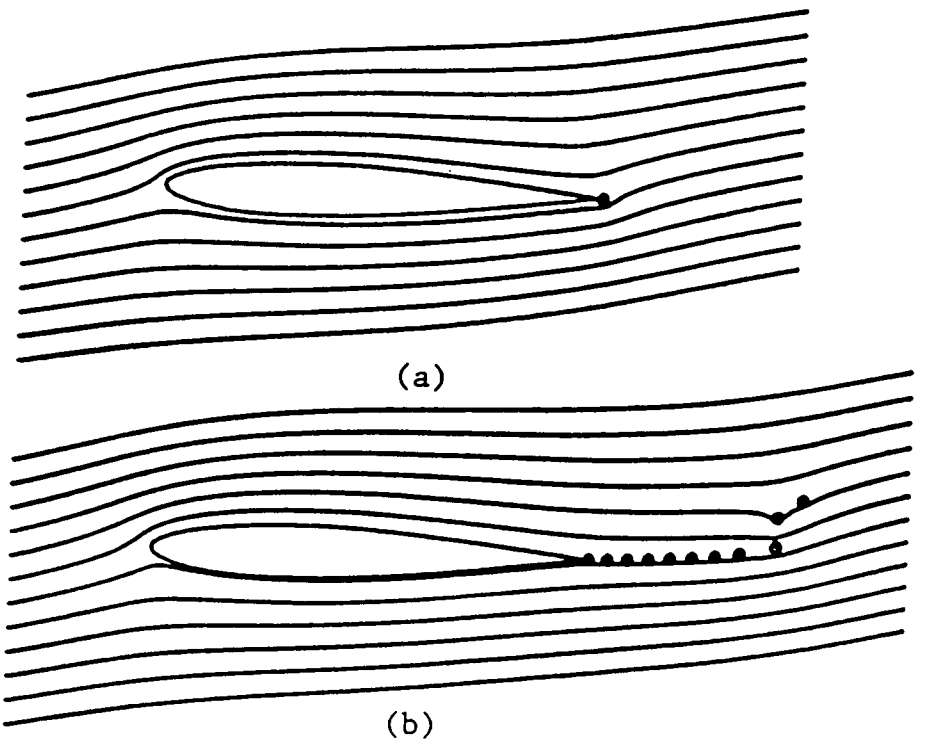

Figure 12. Streamlines around an impulsively started airfoil: streamlines and positions of cores in the wake. (a) just after the start and (b) after several time steps.

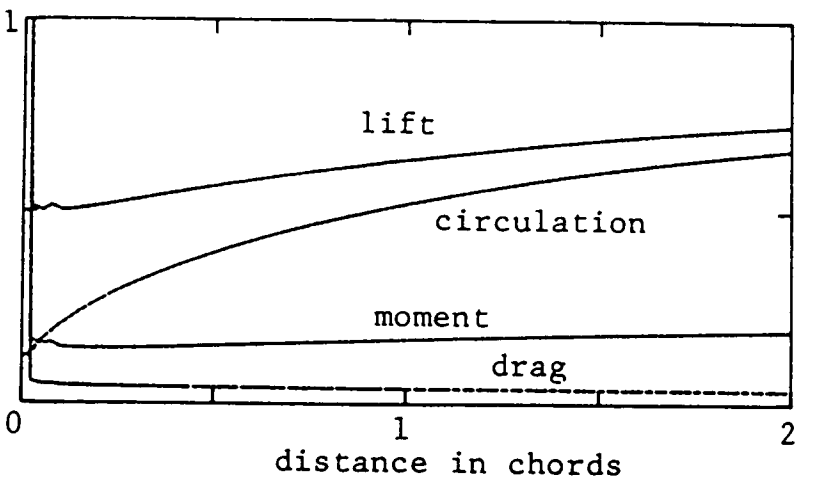

Figure 13. Aerodynamic forces with distance travelled: lift, circulation, moment, and drag x 100 as a function of distance travelled for an impulsively started airfoil.

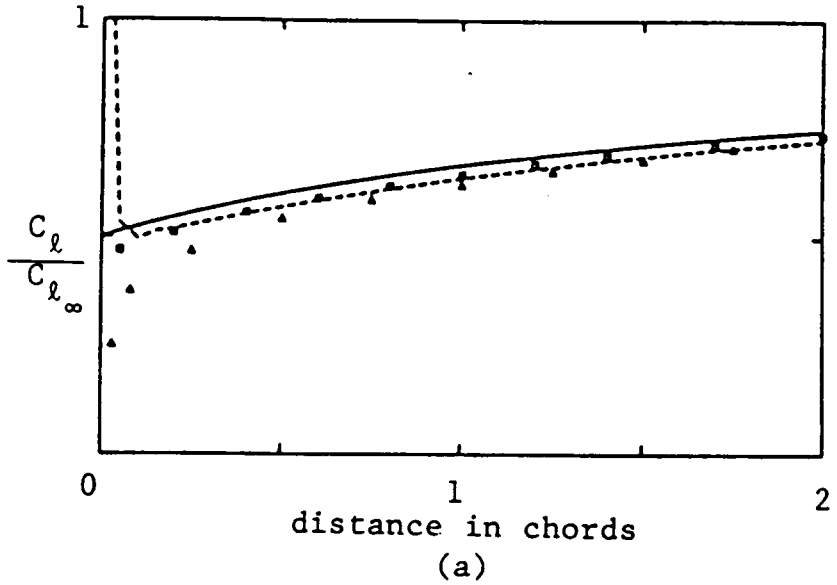

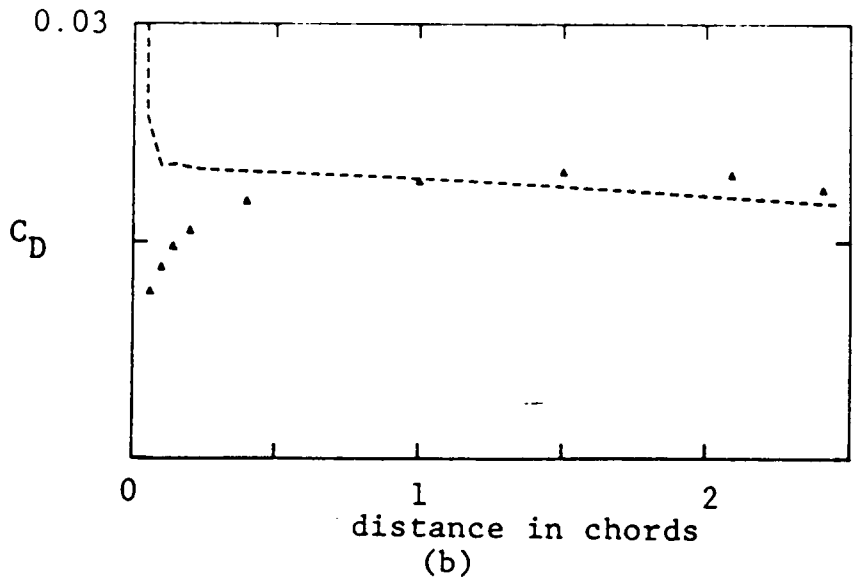

Figure 14. Comparison of aerodynamic forces: (a) lift and (b) drag as functions of distance travelled for an impulsively started airfoil; — Wagner(1925), □ Giesing (1968), △ Basu and Hancock(1978), and --- present results.

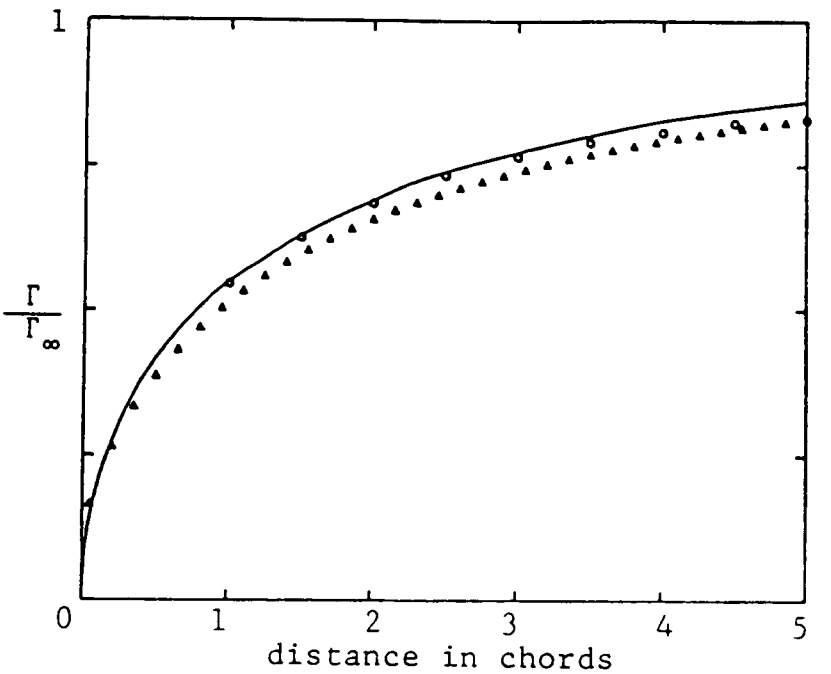

Figure 15. Comparison of build-up of circulation: circulation as a function of distance travelled for impulsively started airfoils. — Wagner, O Walker (see Goldstein), and Δ present results.

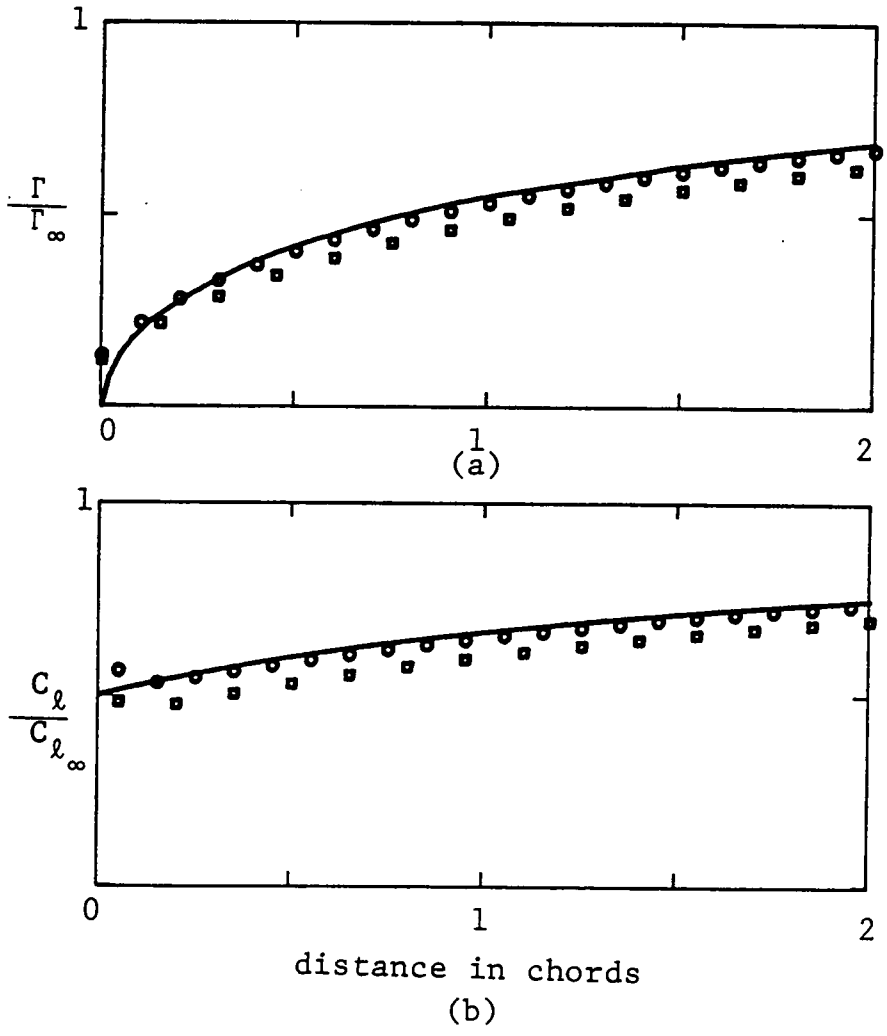

Figure 16. Effect of thickness: (a) circulation and (b) lift around a Joukowski airfoil that started impulsively. o 8.5 %, □ 25.5 % thick, — Wagner.

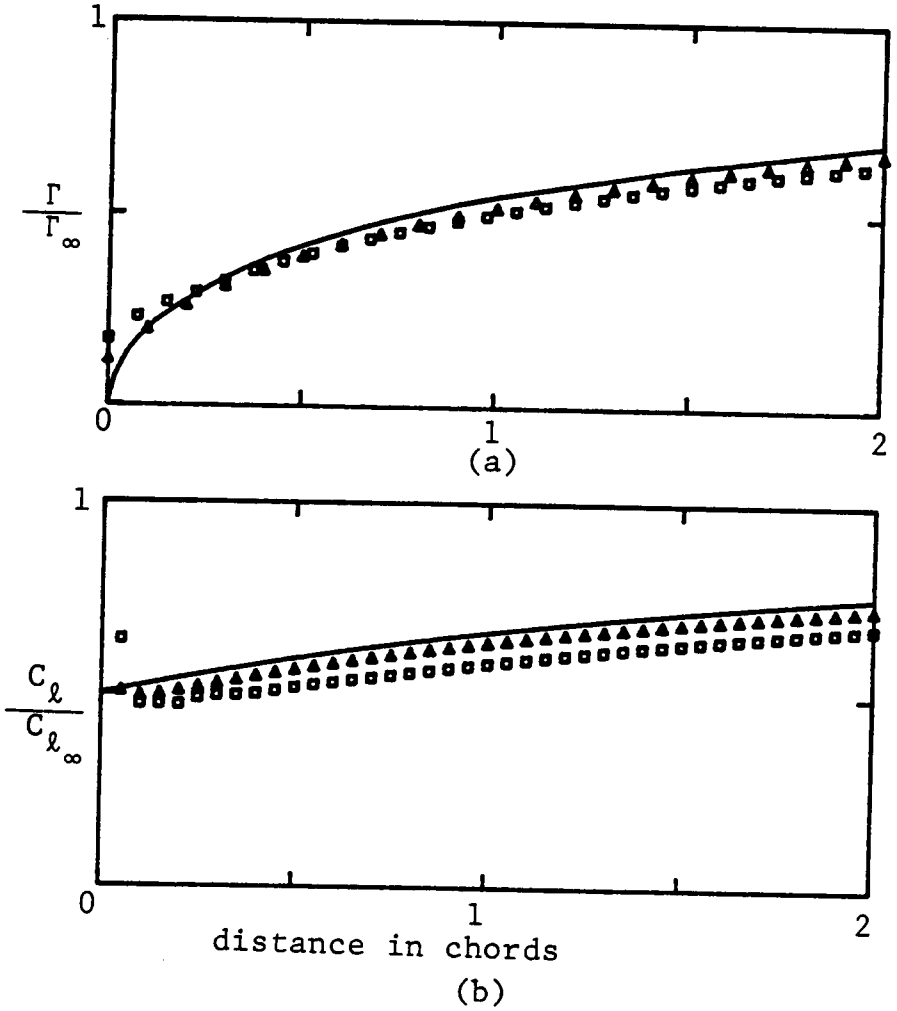

Figure 17. Effect of angle of attack: Δ angle of attack = 0.01 radians, □ angle of attacks = 0.8 radians. Karman-Trefftz airfoil, 12 % thickness.

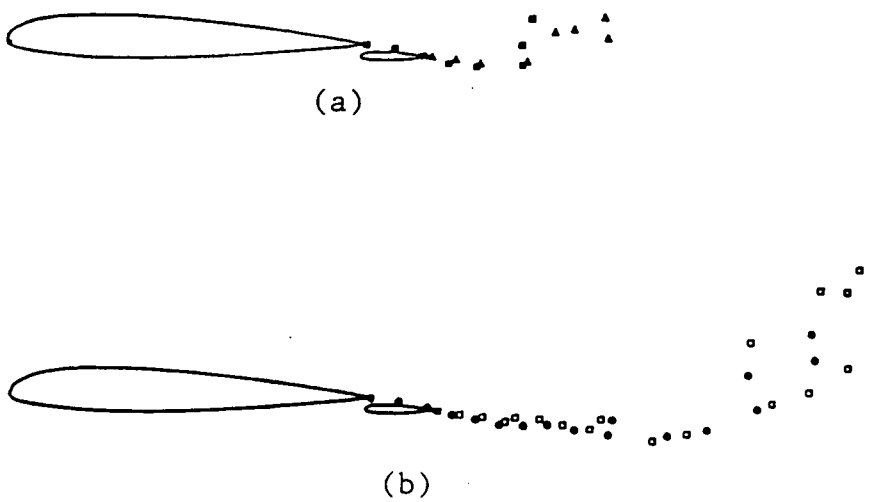

Figure 18. Positions of vortex cores in the wake behind an impulsively started airfoil airfoil and flap: (a) after several time steps and (b) after many time steps.

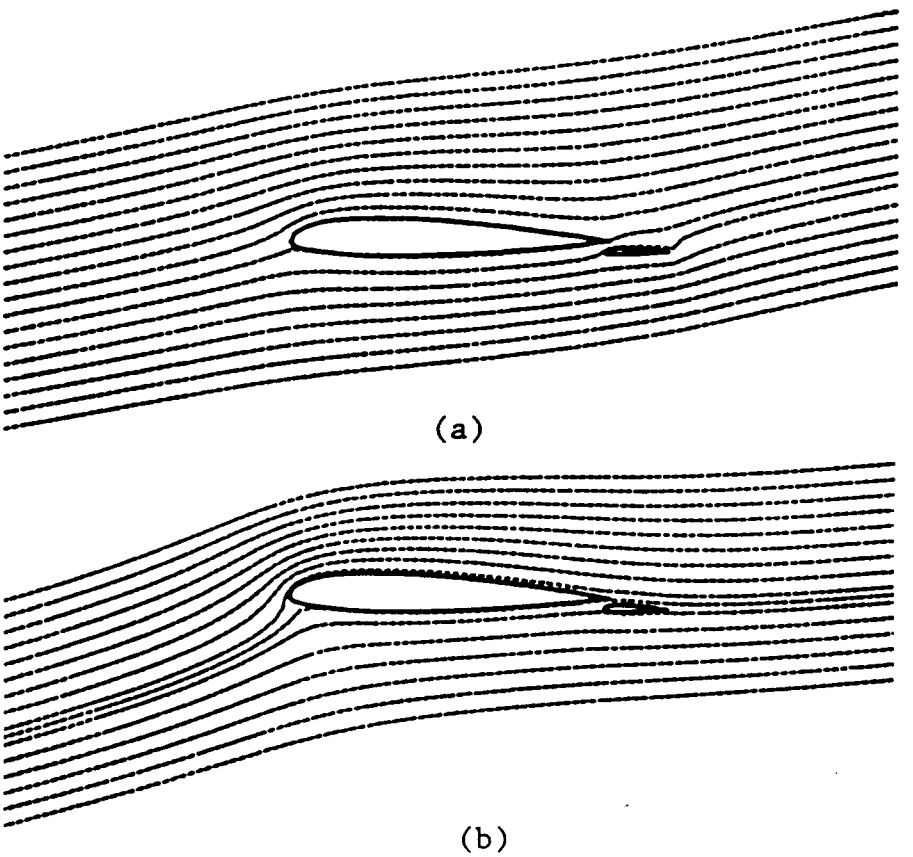

Figure 19. Streamlines around an impulsively started airfoil and flap: (a) just after the start and (b) steady state.

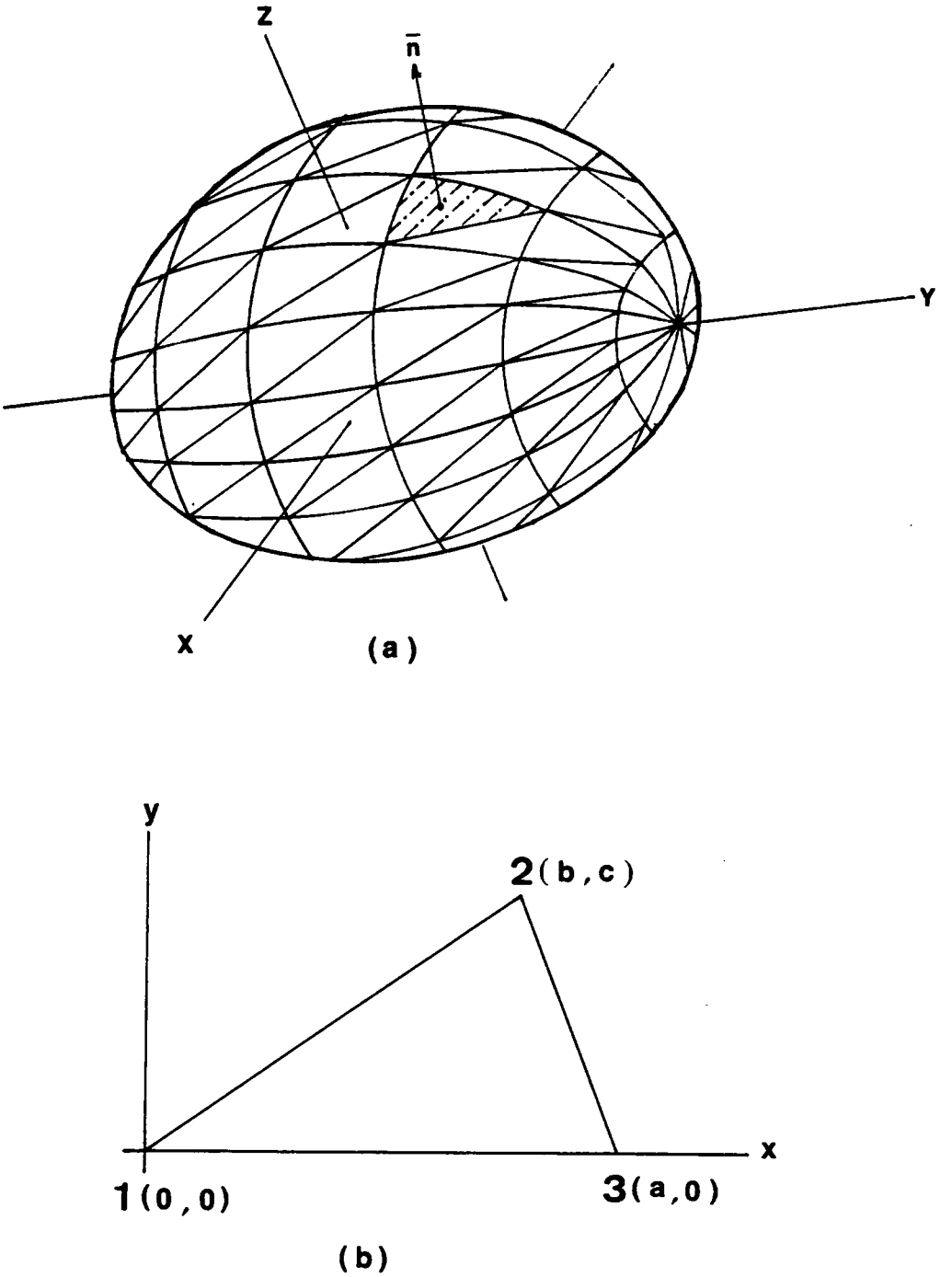

Figure 20. Discretization of the surface of a three-dimensional body: (a) the approximate representation of the body surface and (b) a plane triangular element and local coordinates.

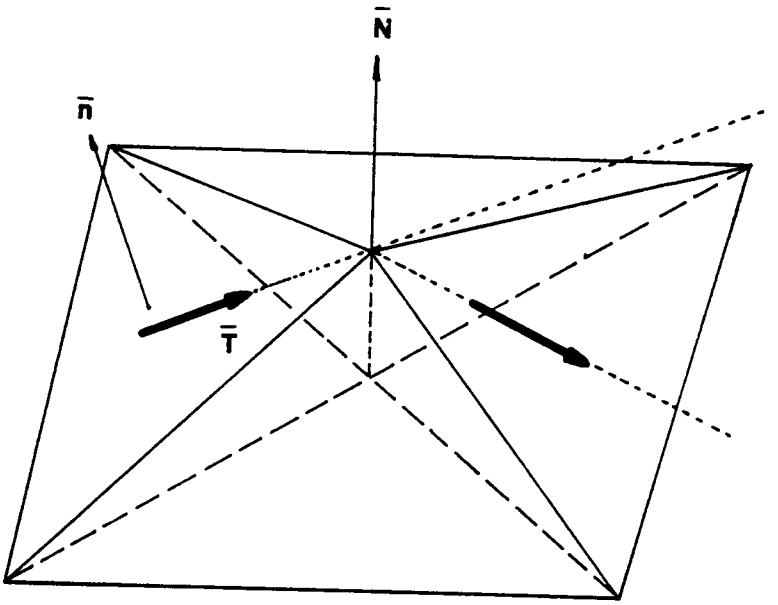

Figure 21. Violation of continuity of a vorticity at a node.

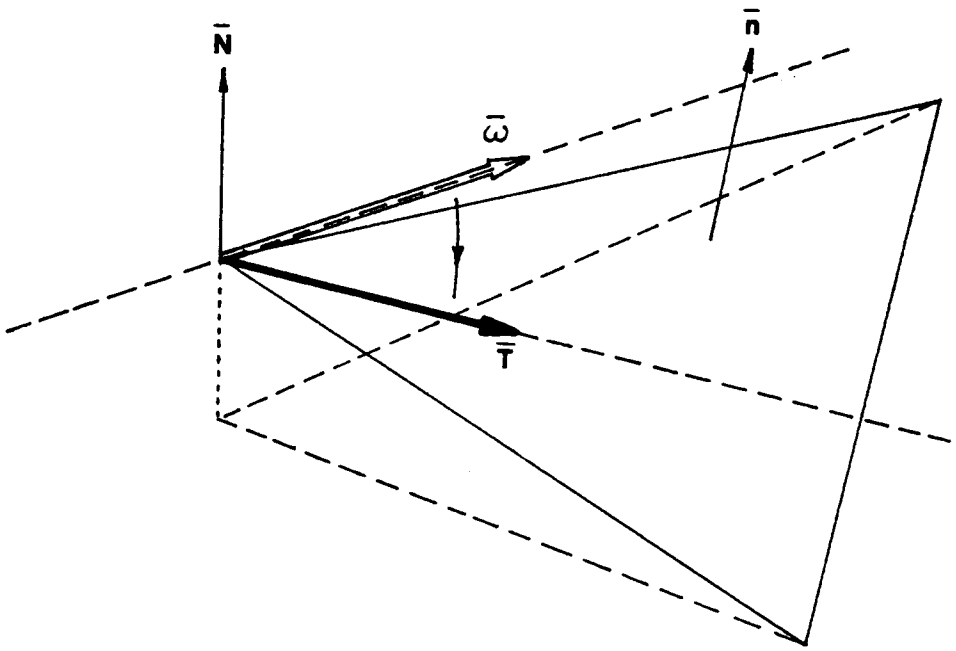

Figure 22. Rotation of ε vorticity at a node.

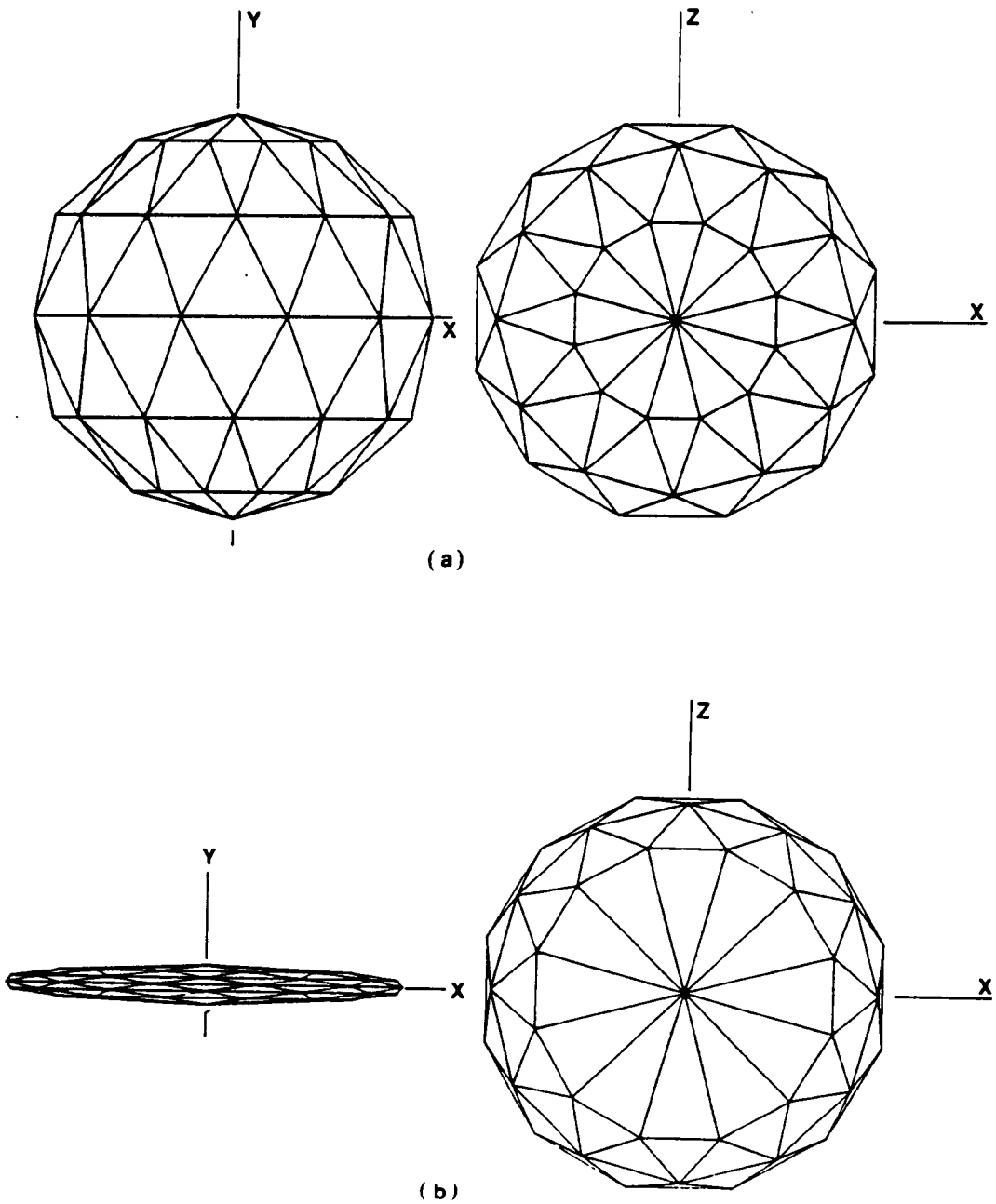

Figure 23. Discretization of typical axisymmetric bodies: (a) a sphere and (b) an oblate spheroid of finess ratio 10:1.

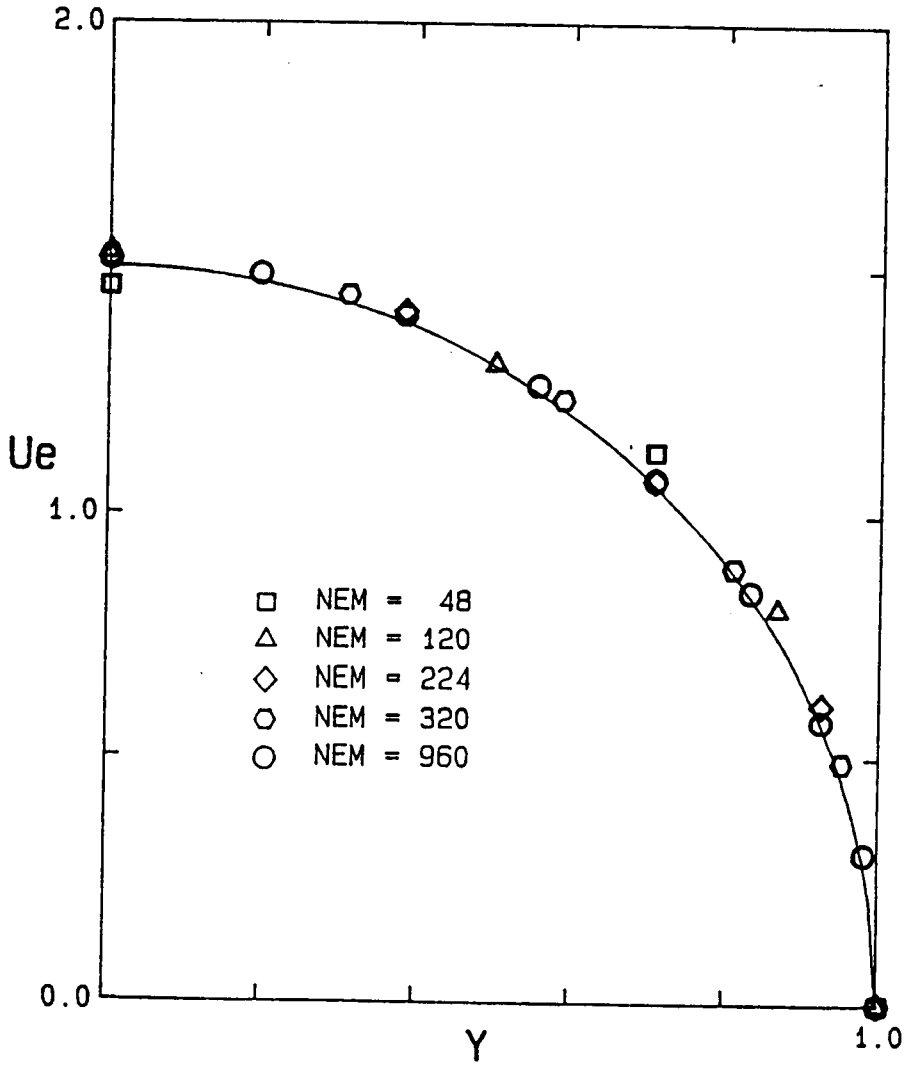

Figure 24. Convergence with number of elements (NEM): the results predicted by the present flat source panel method as the number of elements used increases. — analytic solution

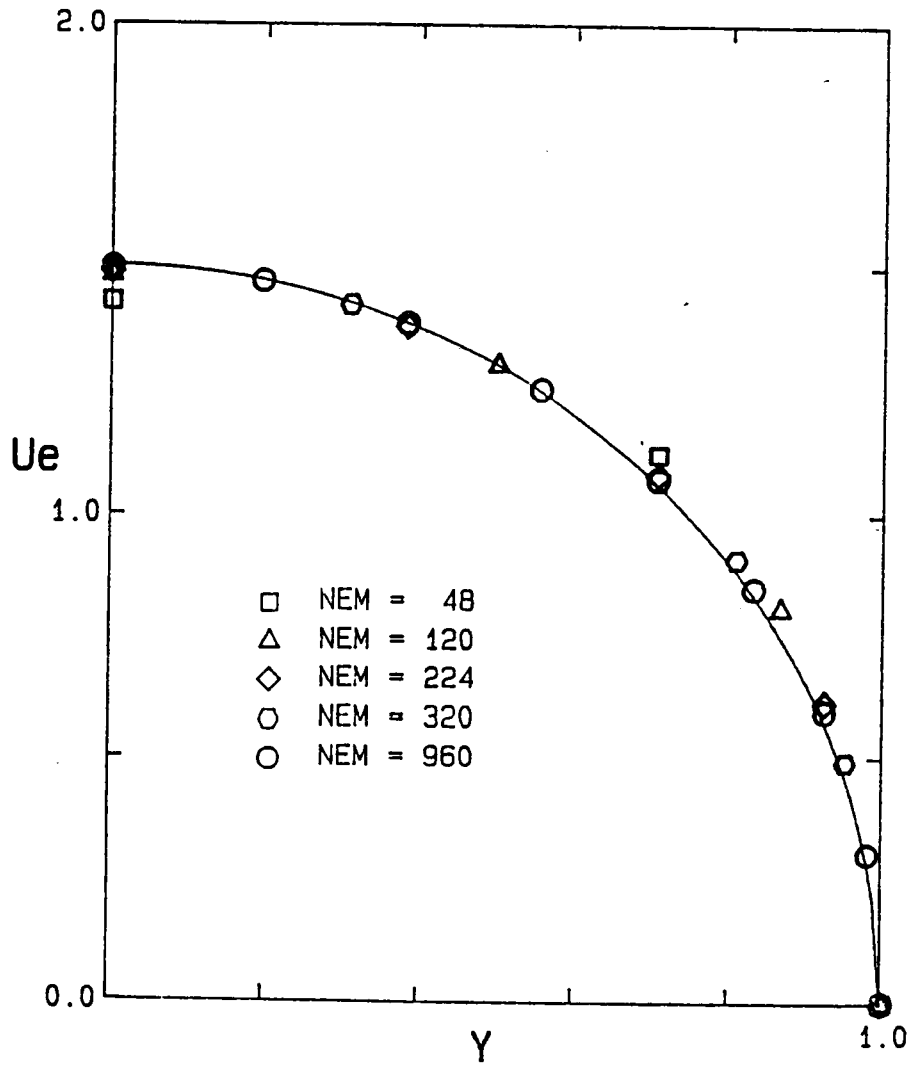

Figure 25. Convergence with number of elements (NEM): the results predicted by the present curved source panel method as the number of elements used increases. — exact solution

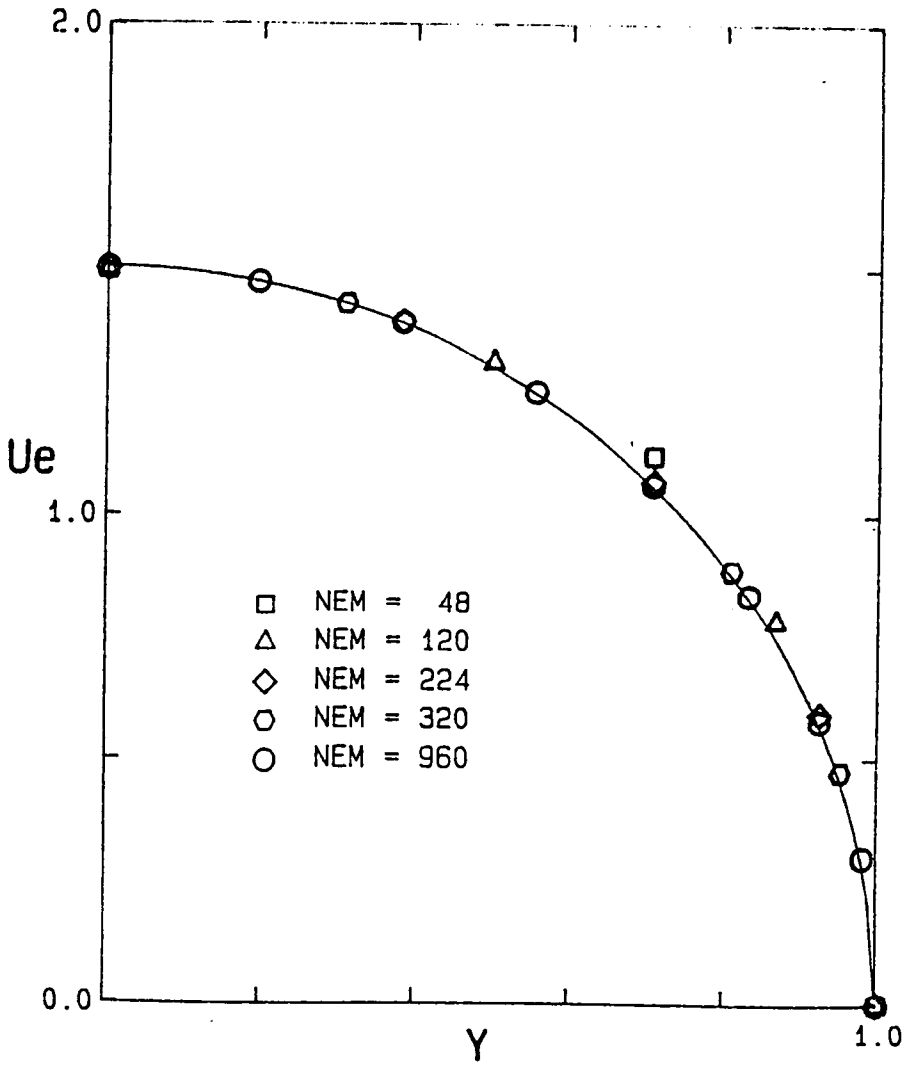

Figure 26. Convergence with number of elements (NEM): the results predicted by the present vorticity panel method as the number of elements used increases. — exact solution

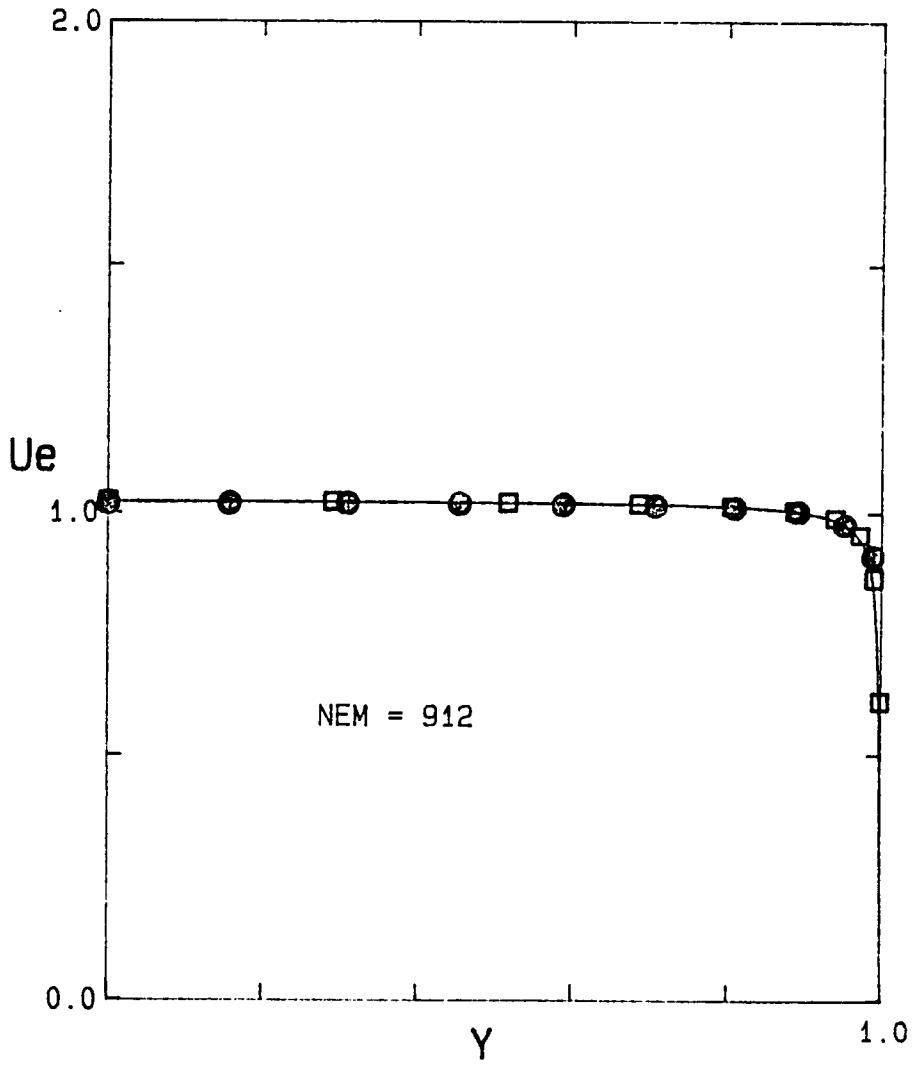

Figure 27. Effects of element distributions: (a) ● equal spacings and (b) □ more elements near the high-velocity-gradient region. — exact solution

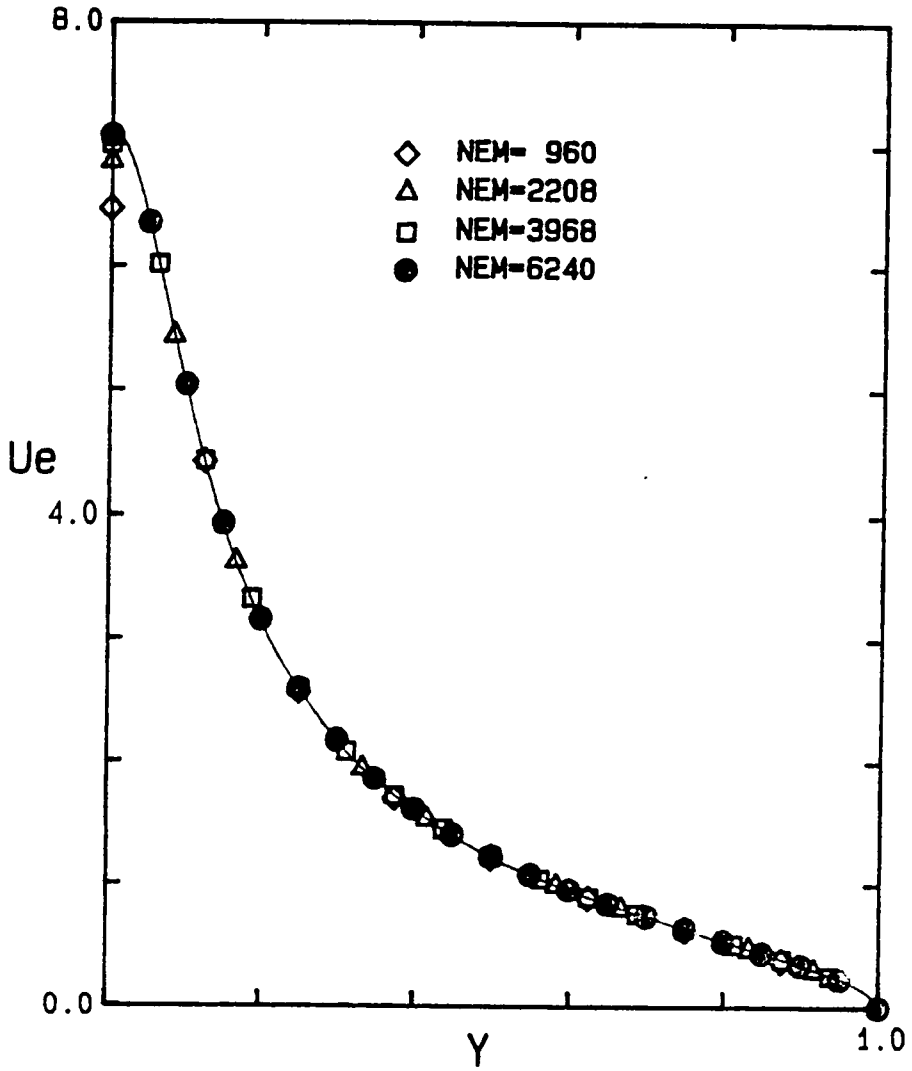

Figure 28. Stability of the vorticity panel method with respect to the number of elements (NEM): the results computed by the present vorticity panel method converge to exact solution as the number of elements increases for an oblate spheroid of finess ratio 10:1.

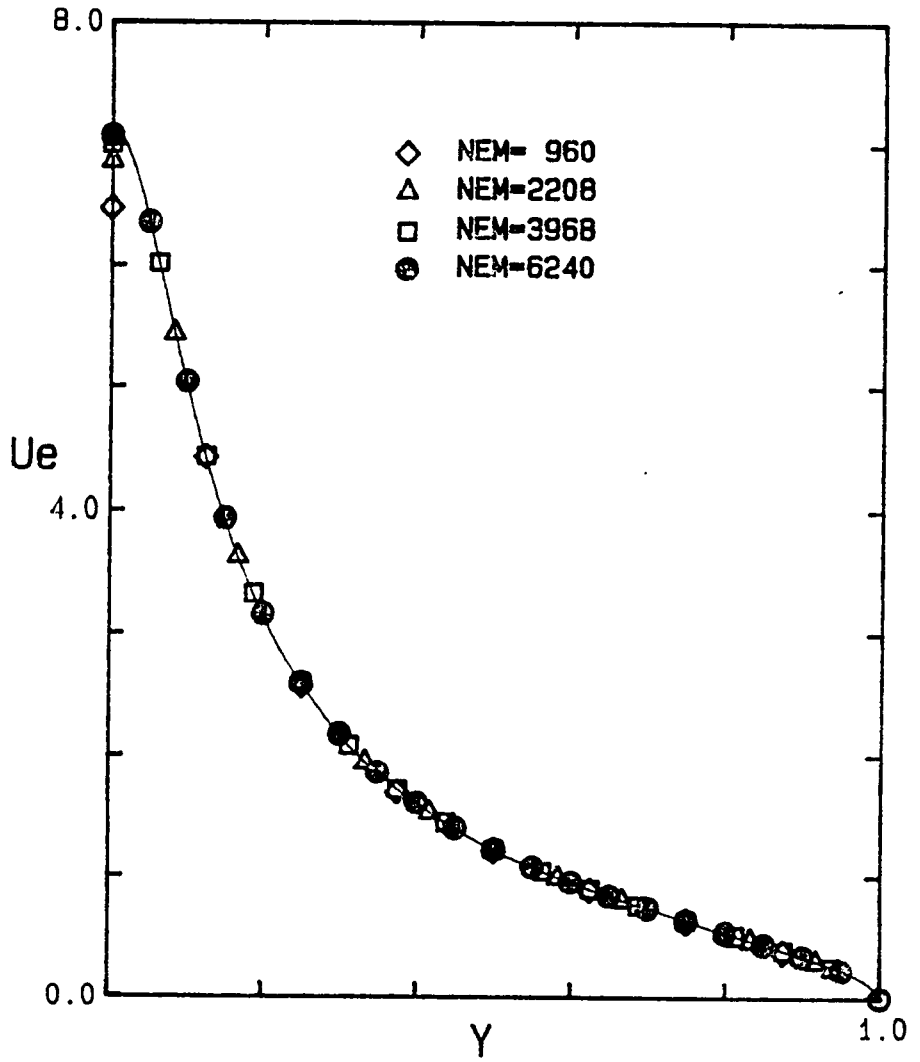

Figure 28. Stability of the vorticity panel method with respect to the number of elements (NEM): the results computed by the present vorticity panel method converge to exact solution as the number of elements increases for an oblate spheroid of finess ratio 10:1.

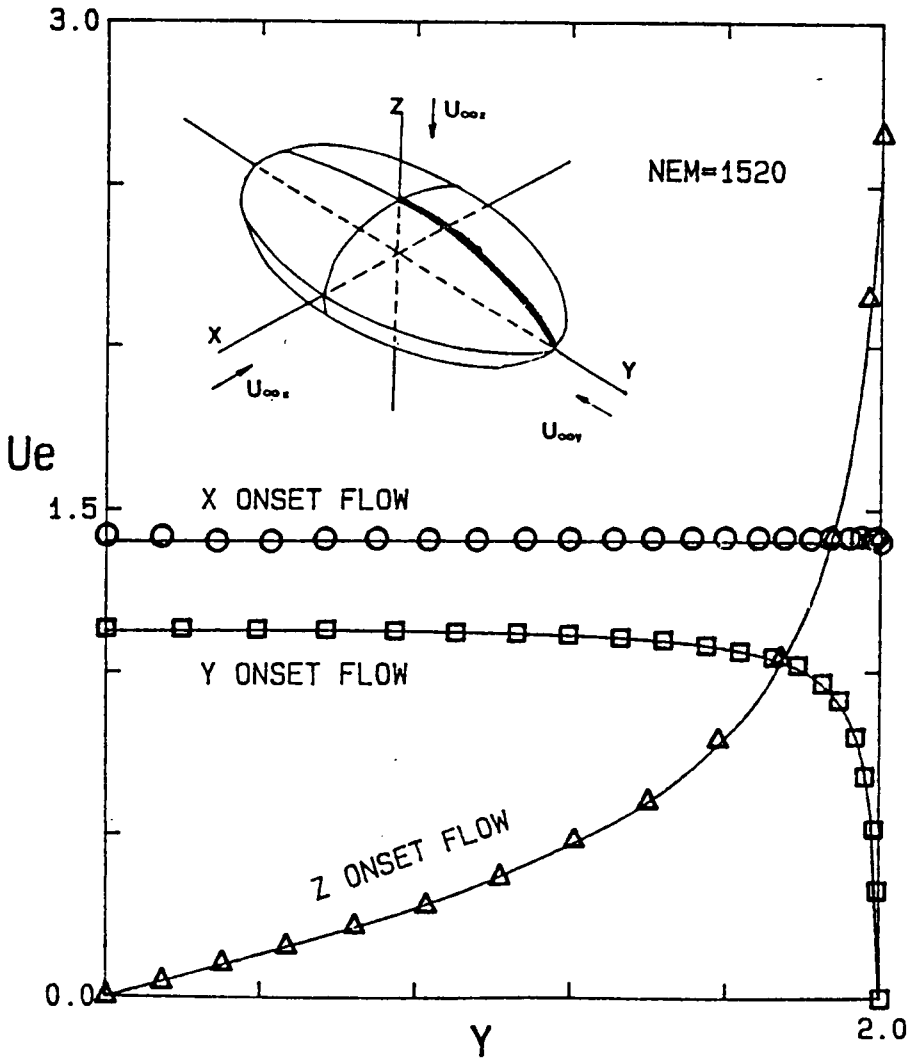

Figure 29. Velocities over an ellipsoid: comparison of analytic and computed velocity distributions over an ellipsoid with axes ratios 1:2:0.5. flat source panel method □ Δ ○ numerical, —— analytical (a)velocities in the y-z plane.

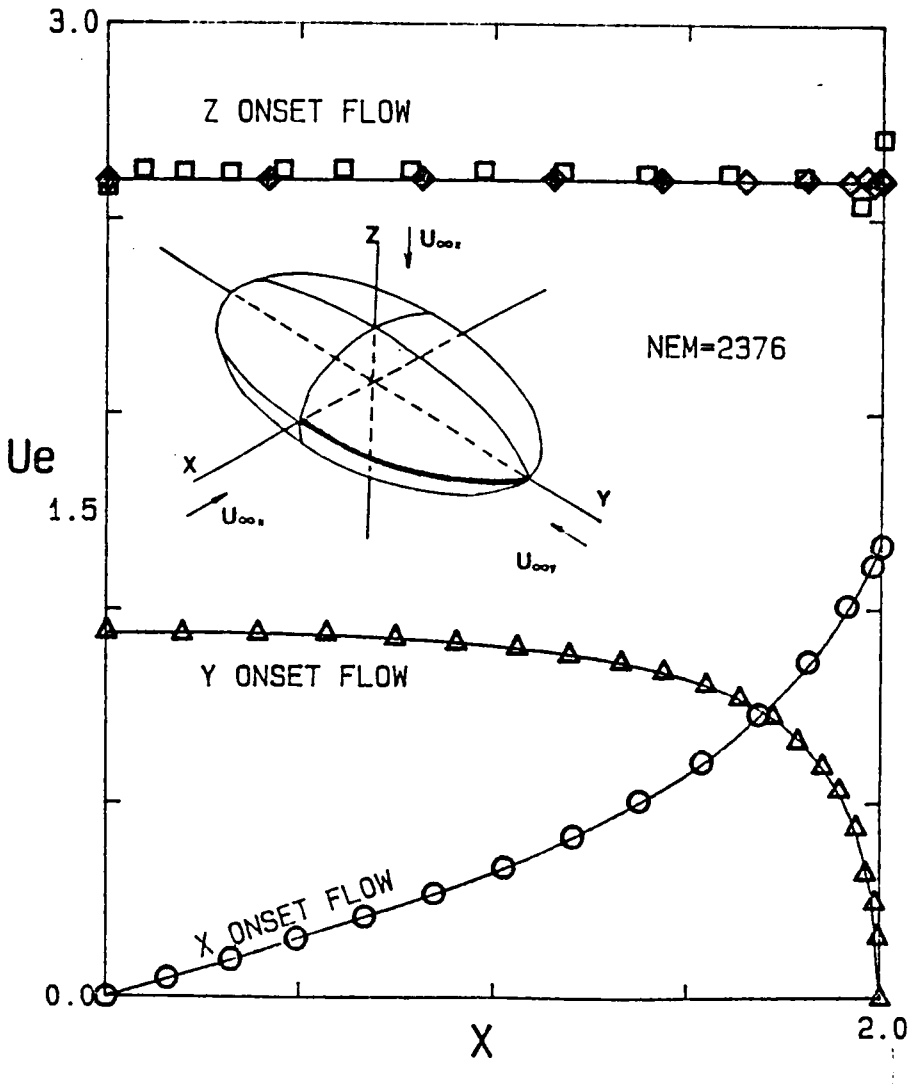

Figure 29. (b) velocities in the x-y plane.

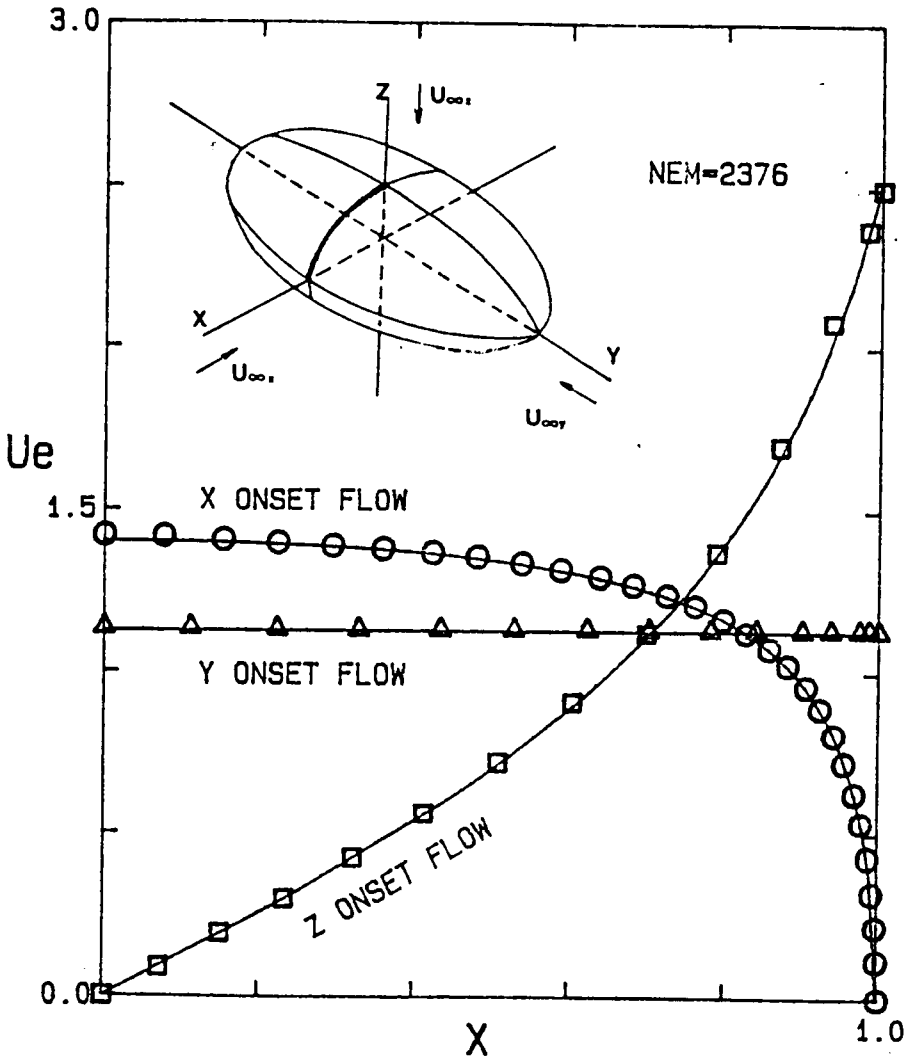

Figure 29. (c) velocities in the x-z plane.

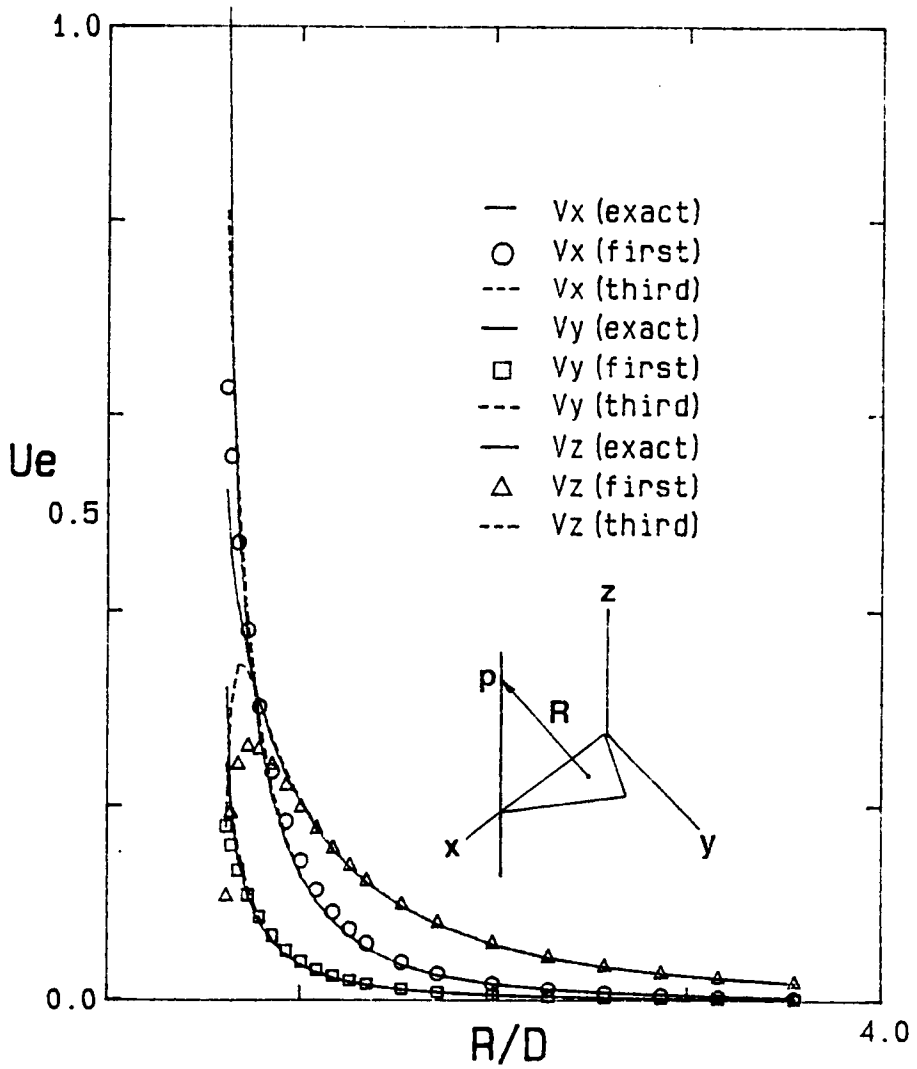

Figure 30. Multipole expansion: (a)the velocities calculated by exact and approximate formulas are compared over a flat triangular element.

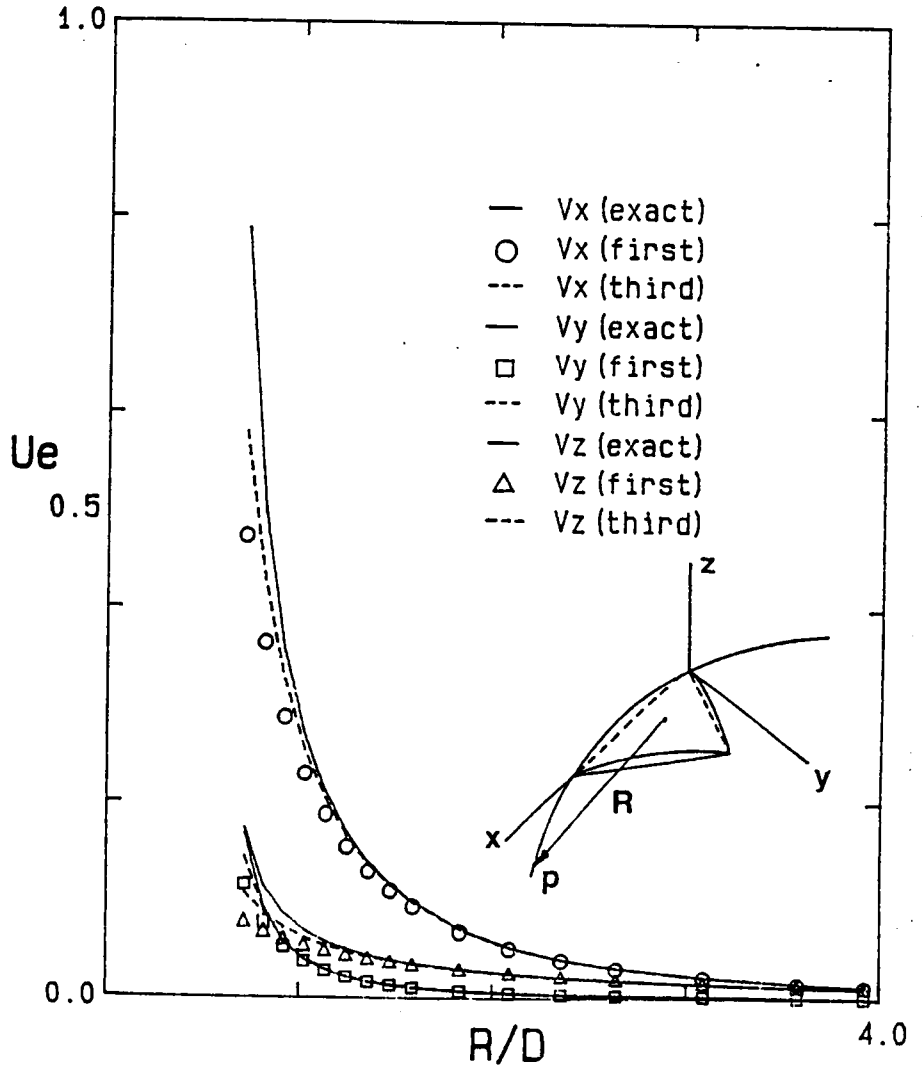

Figure 30. (b) the velocities calculated by exact and approximate formulas are compared over a curved triangular element.

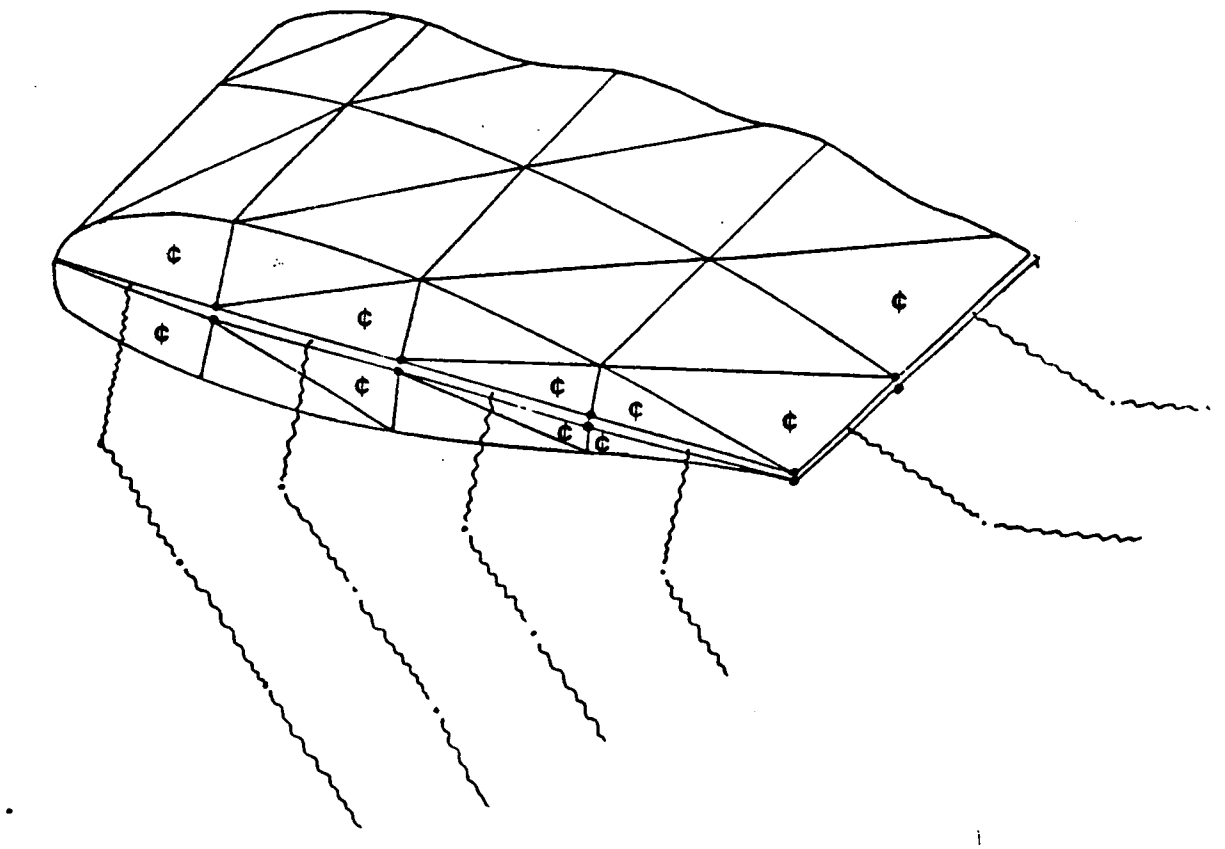

Figure 31. Discretization of the surface of a lifting body: the upper and lower surfaces join along the separation lines where two nodes exist at a point. ¢ denotes elements having an edge along a separation line.

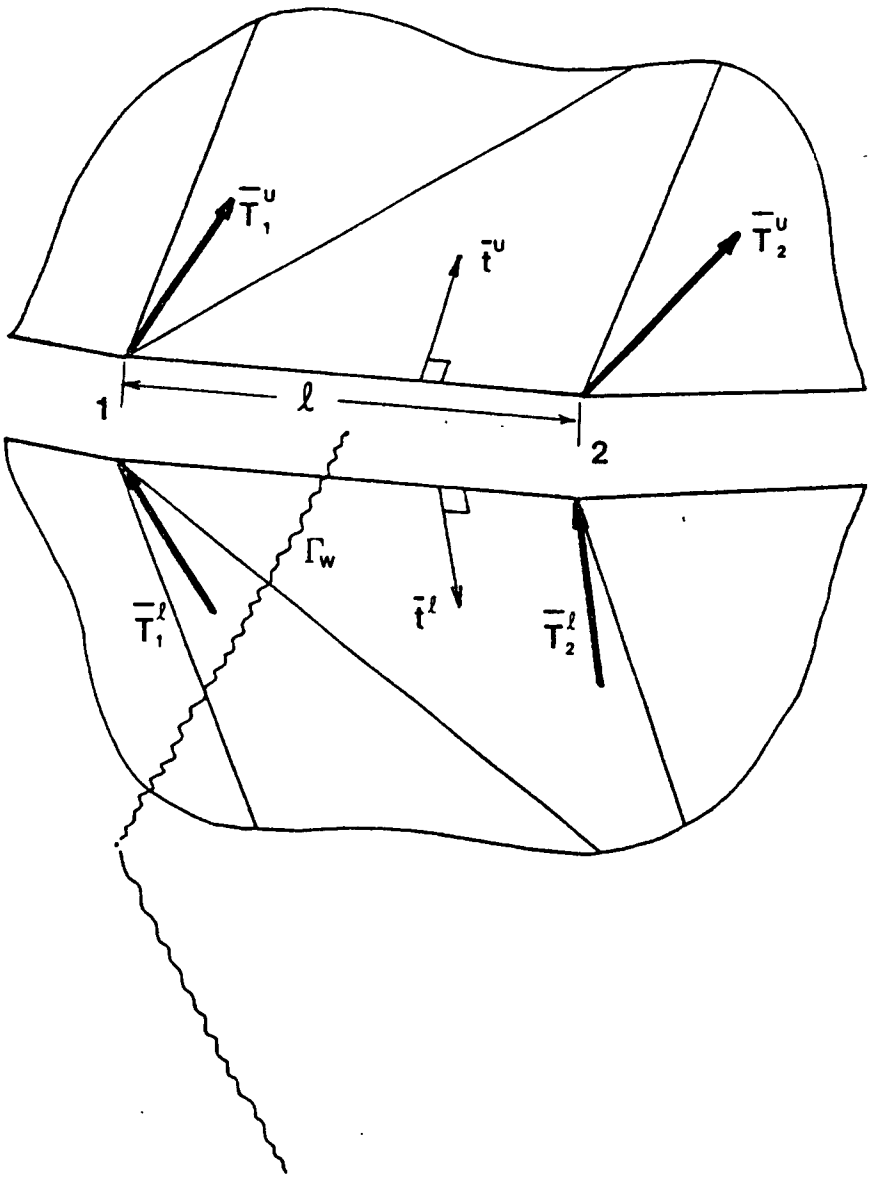

Figure 32. Shedding vorticity (or circulation) into the wake: the amount of shedding vorticity into the wake is related to the vorticities on both surfaces.

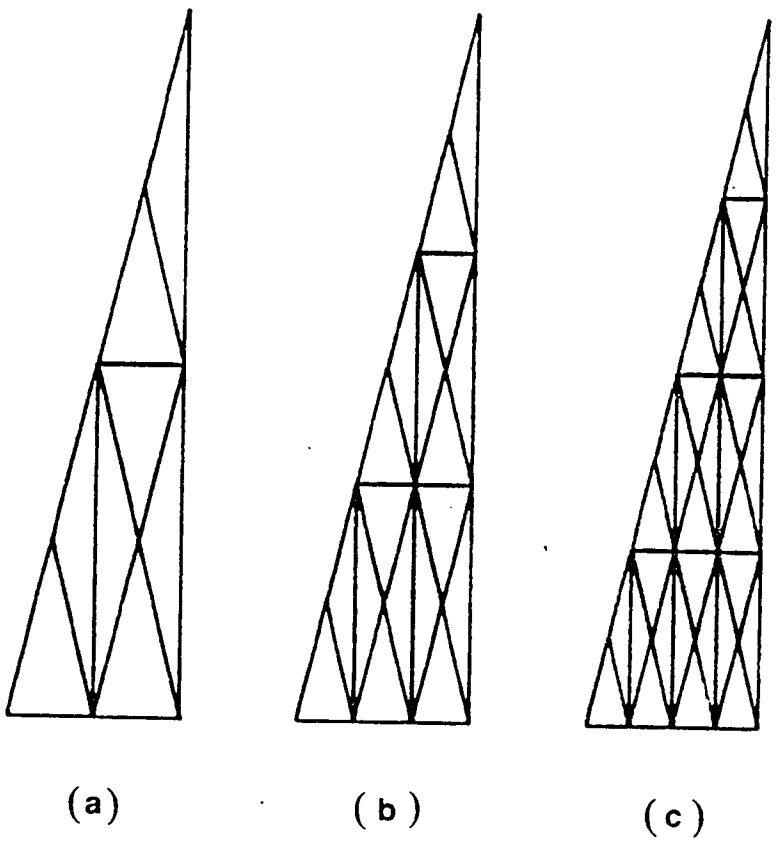

Figure 33. Discretization of flat delta wings: (a) 2 rows, (b) 3 rows, and (c) 4 rows.

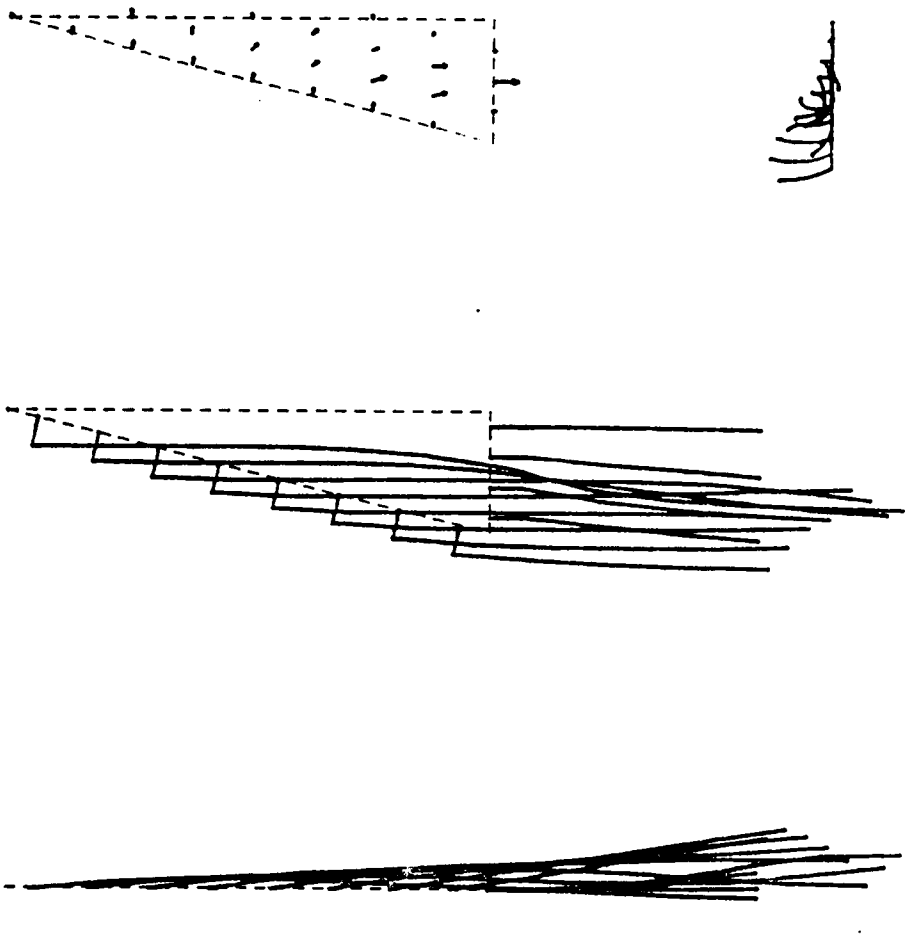

Figure 34. Wake shapes and vorticity distributions over a delta wing: unit aspect ratio flat wing, the number of rows = 4 (a)5 degree angle of attack

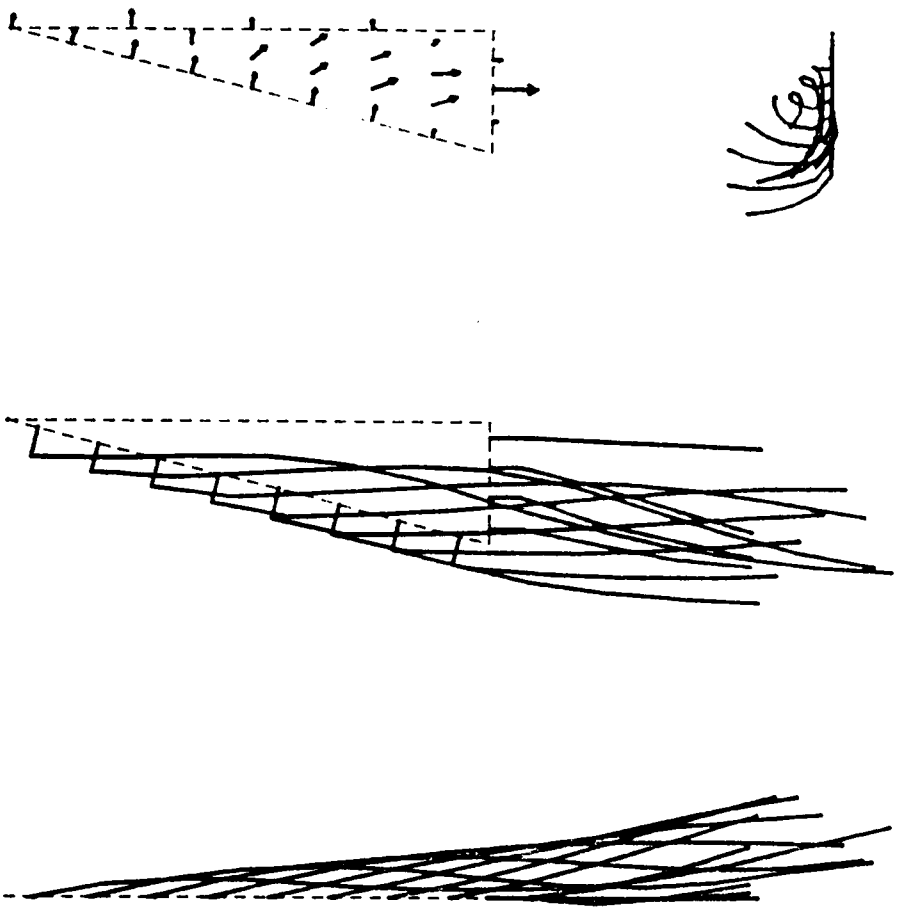

Figure 34. (b) 10 degree angle of attack.

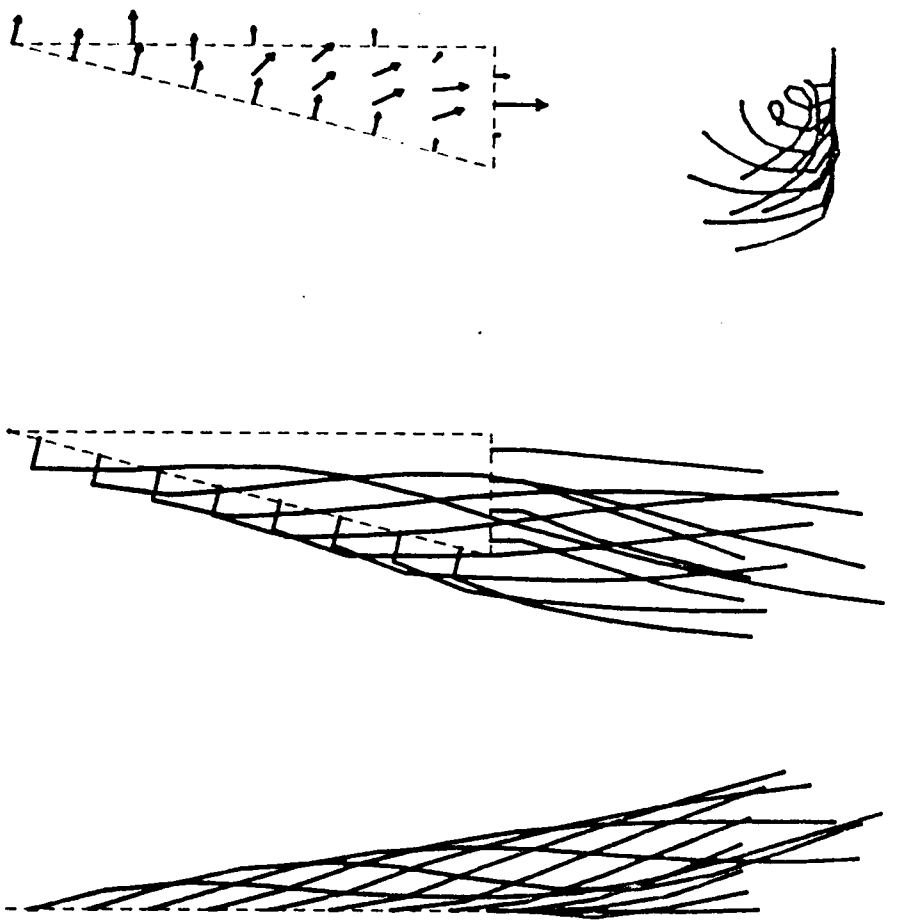

Figure 34. (c) 15 degree angle of attack.

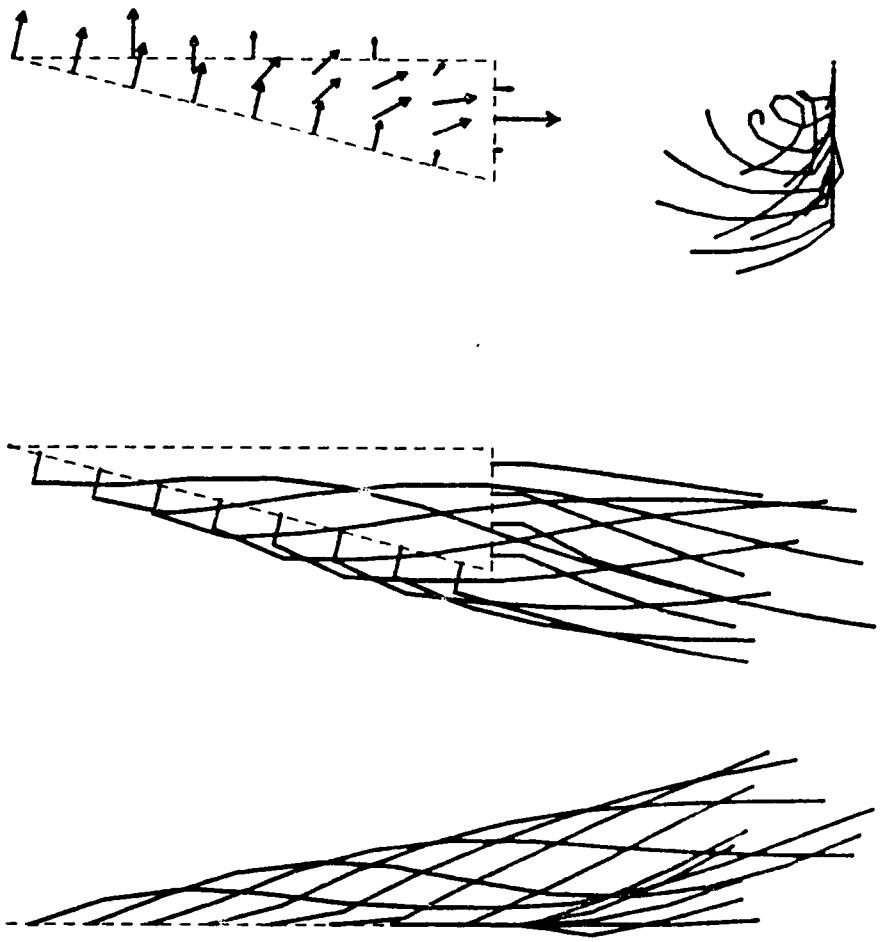

Figure 34. (d) 20 degree angle of attack.

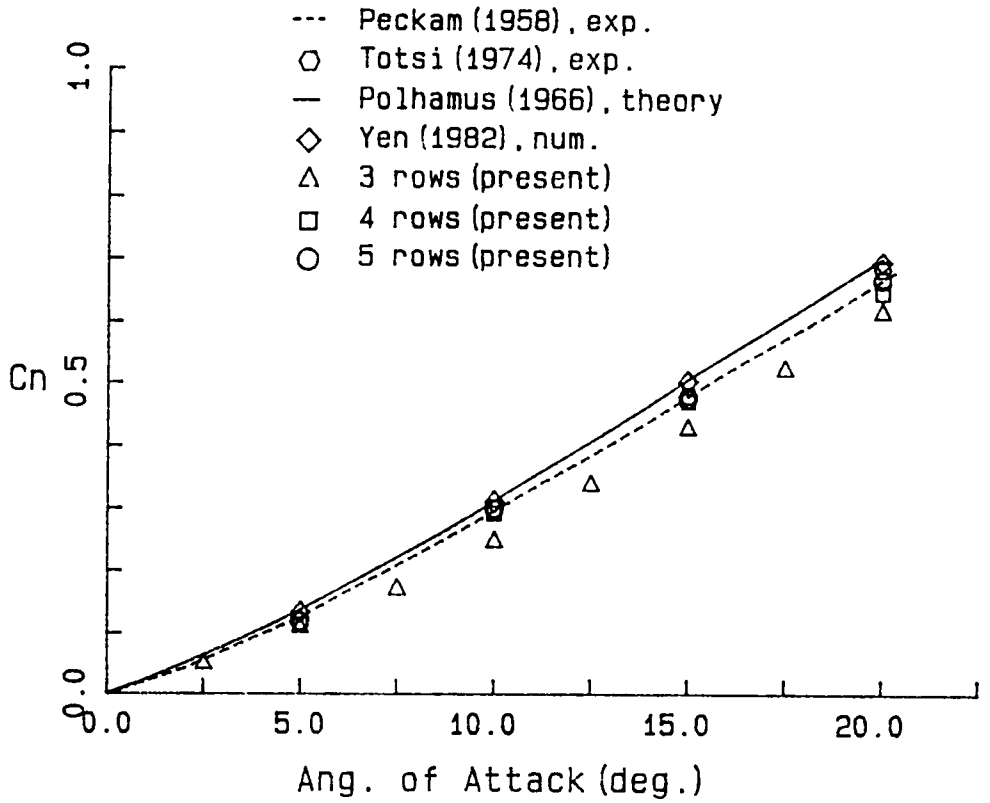

Figure 35. The normal-force coefficients for a flat delta wing of unit aspect ratio computed by the present method are compared with others.

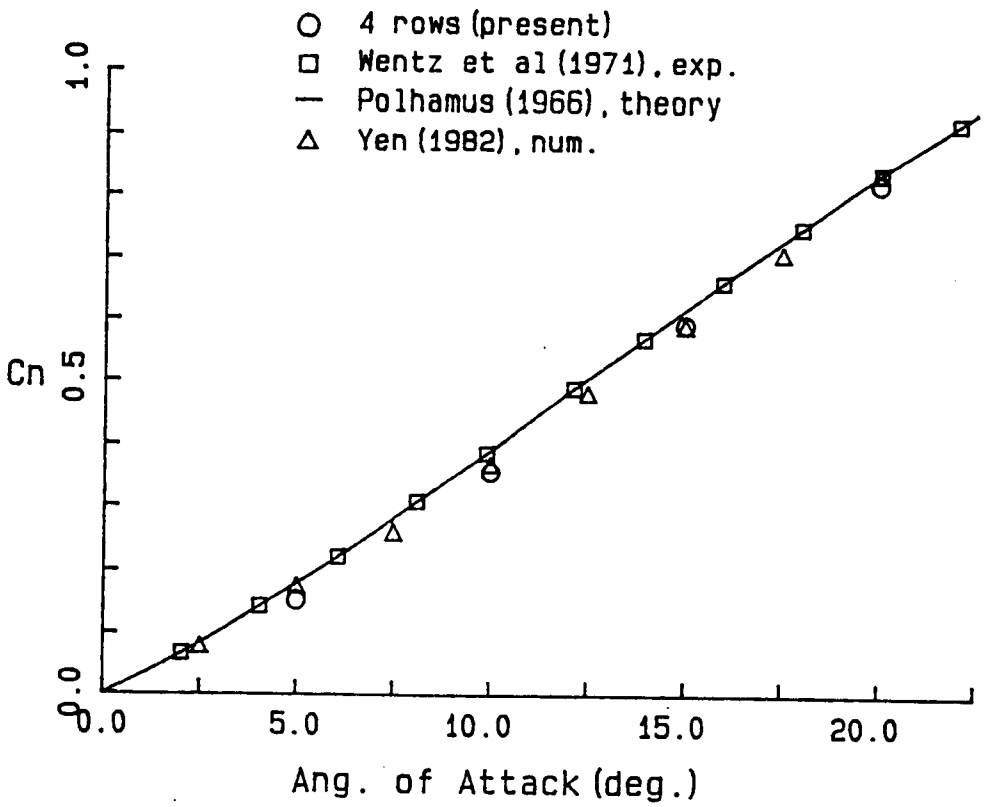

Figure 36. The normal-force coefficients for a flat delta wing of 1.46 aspect ratio computed by the present method are compared with others.

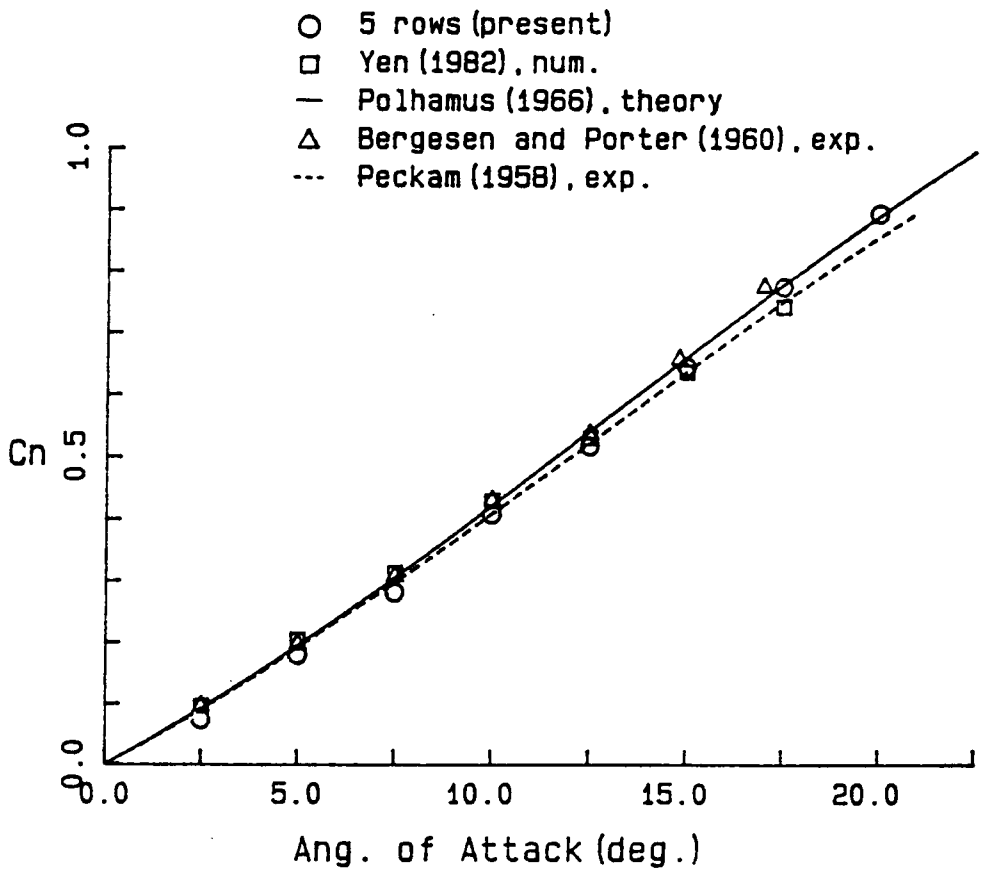

Figure 37. The normal-force coefficients for a flat delta wing of 1.67 aspect ratio computed by the present method are compared with others.

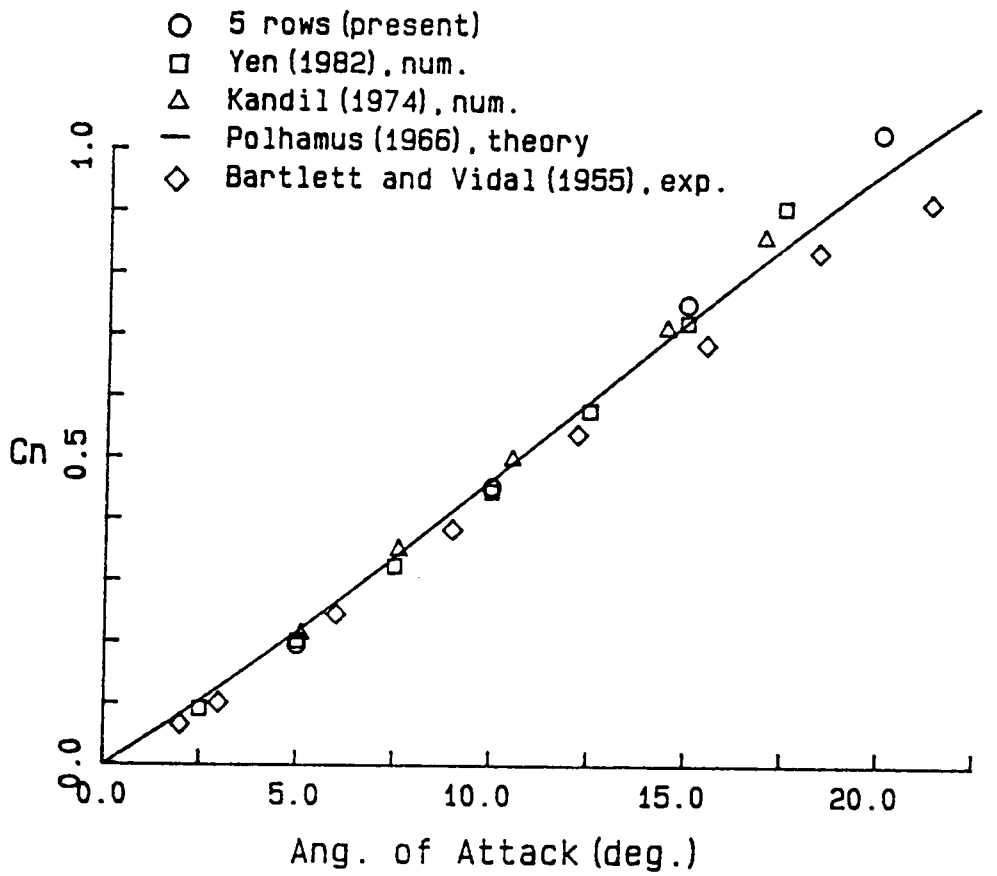

Figure 38. The normal-force coefficients for a flat delta wing of 2 aspect ratio computed by the present method are compared with others.

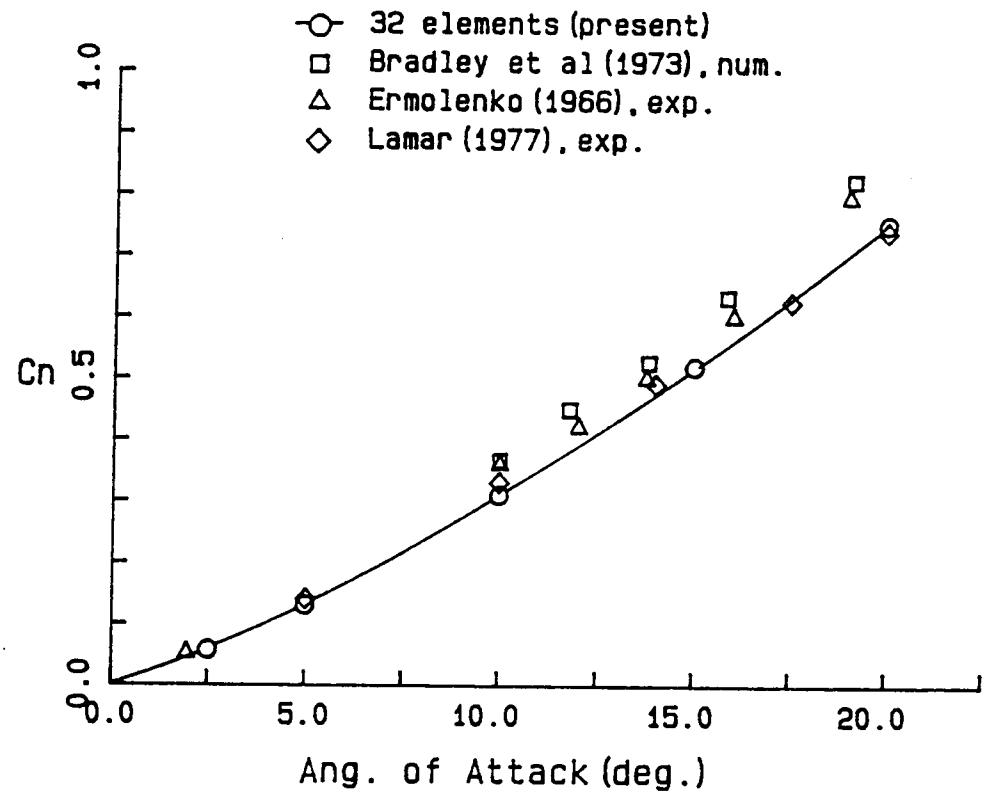

Figure 39. The normal-force coefficients for a flat rectangular wing of unit aspect ratio computed by the present method are compared with others.

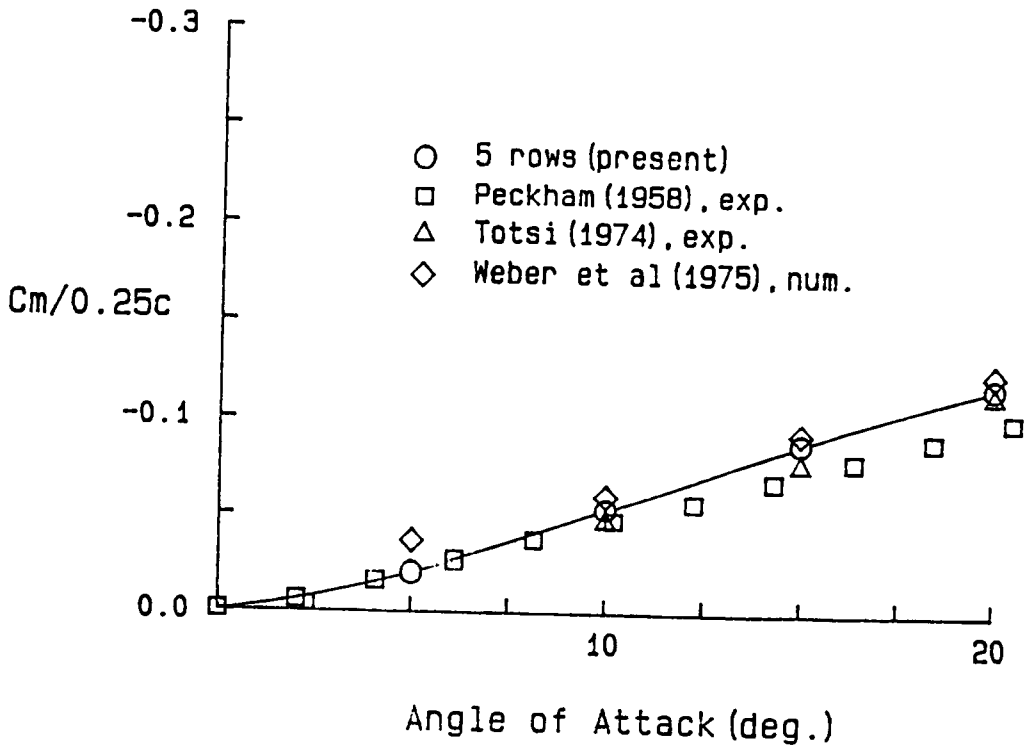

Figure 40. The pitching moment coefficients for a flat delta wing of unit aspect ratio computed by the present method are compared with others.

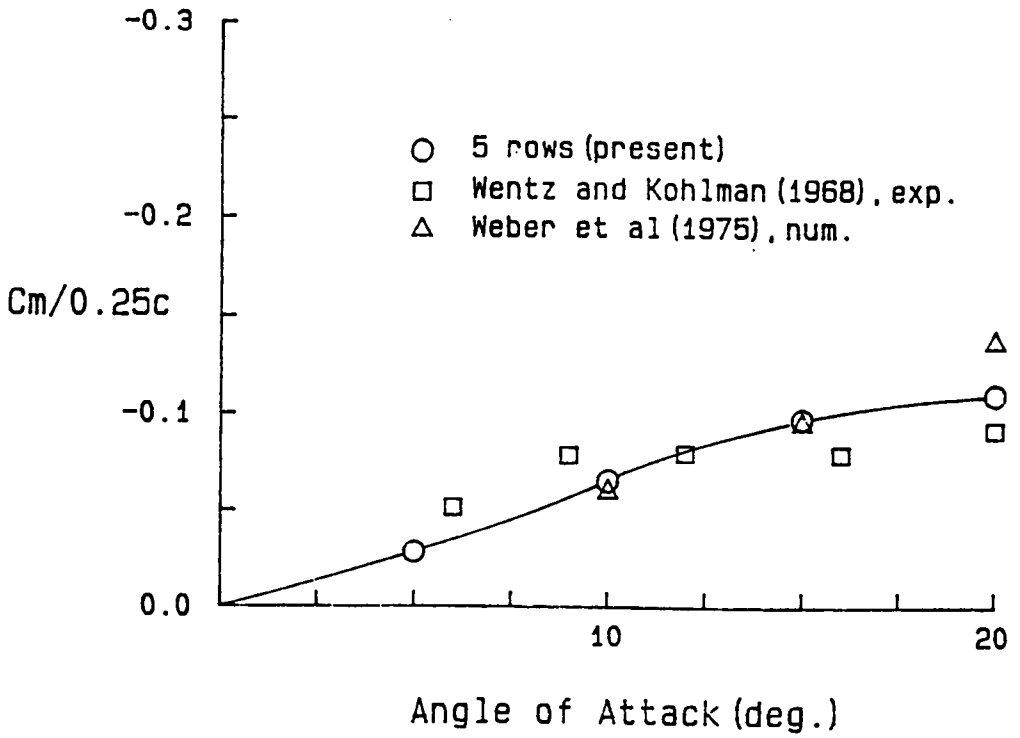

Figure 41. The pitching moment coefficients for a flat delta wing of 1.46 aspect ratio computed by the present method are compared with others.

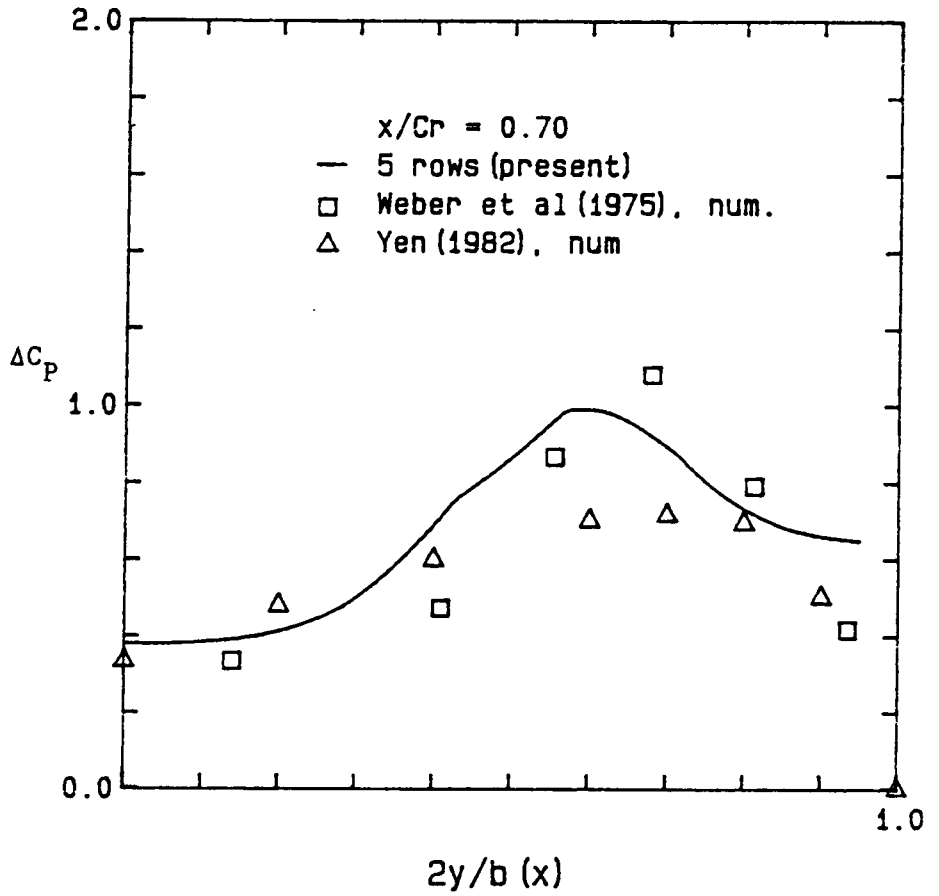

Figure 42. (a) pressure jumps across a flat delta wing of unit aspect ratio as a function of spanwise position at 0.70 chord distance computed by the present method are compared with others.

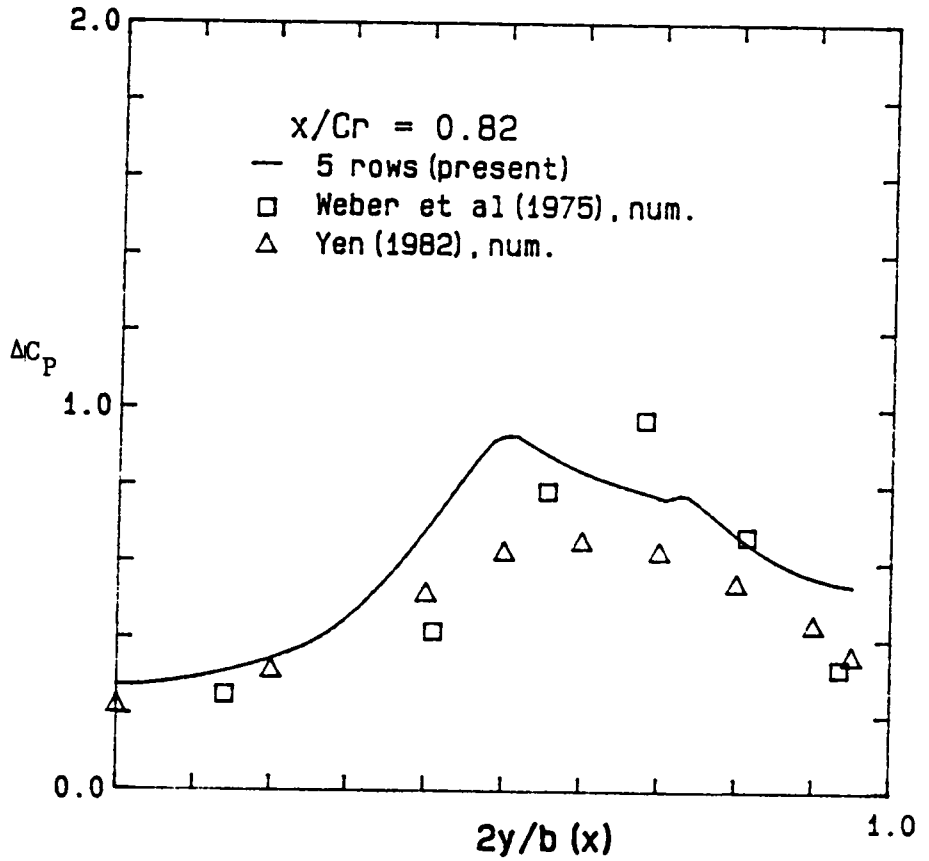

Figure 42. (b) pressure jumps across a flat delta wing of unit aspect ratio as a function of spanwise position at 0.82 chord distance computed by the present method are compared with others.

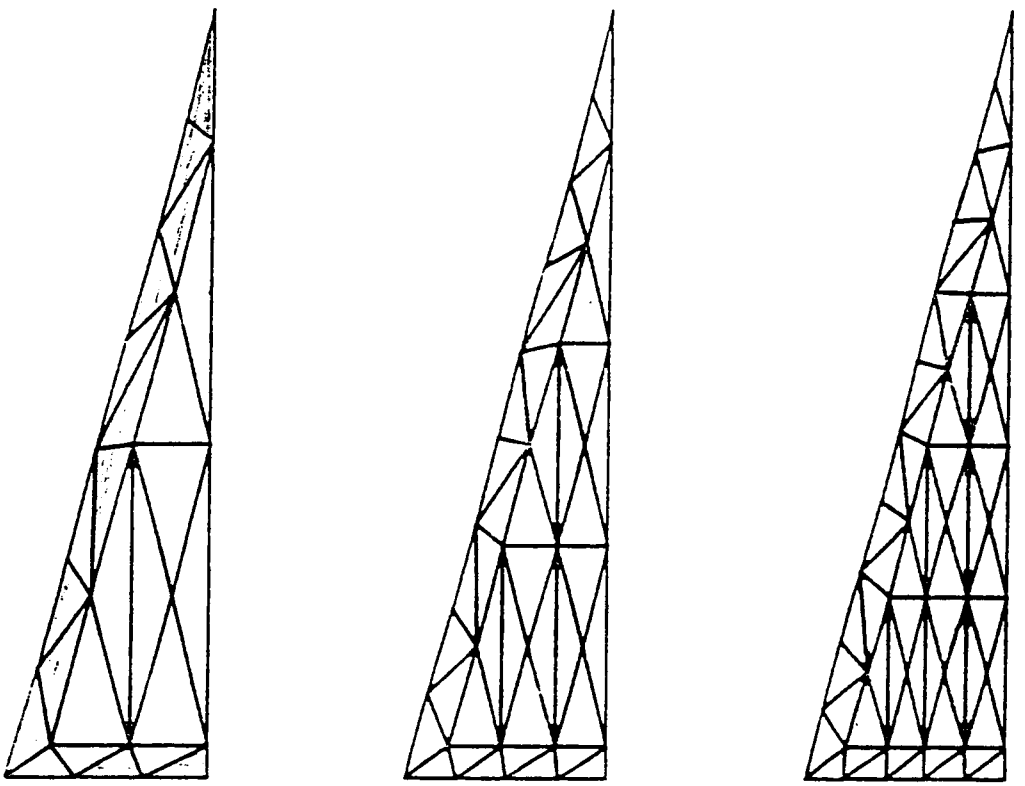

Figure 43. Discretization of a thick delta wing: (a) 4 rows, (b) 5 rows, and (c) 6 rows.

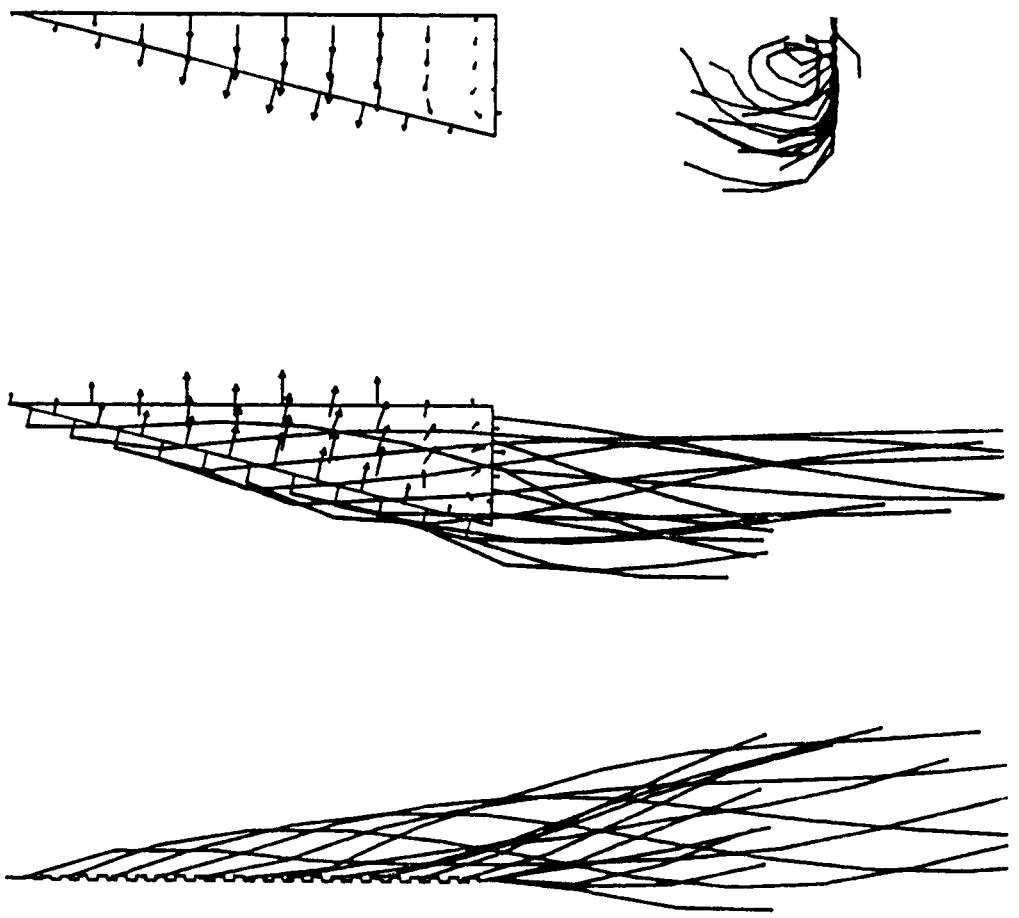

Figure 44. Wakes and vorticity distributions on a thick delta wing: 15 degrees angle of attack, unit aspect ratio, and 1 % thickness.

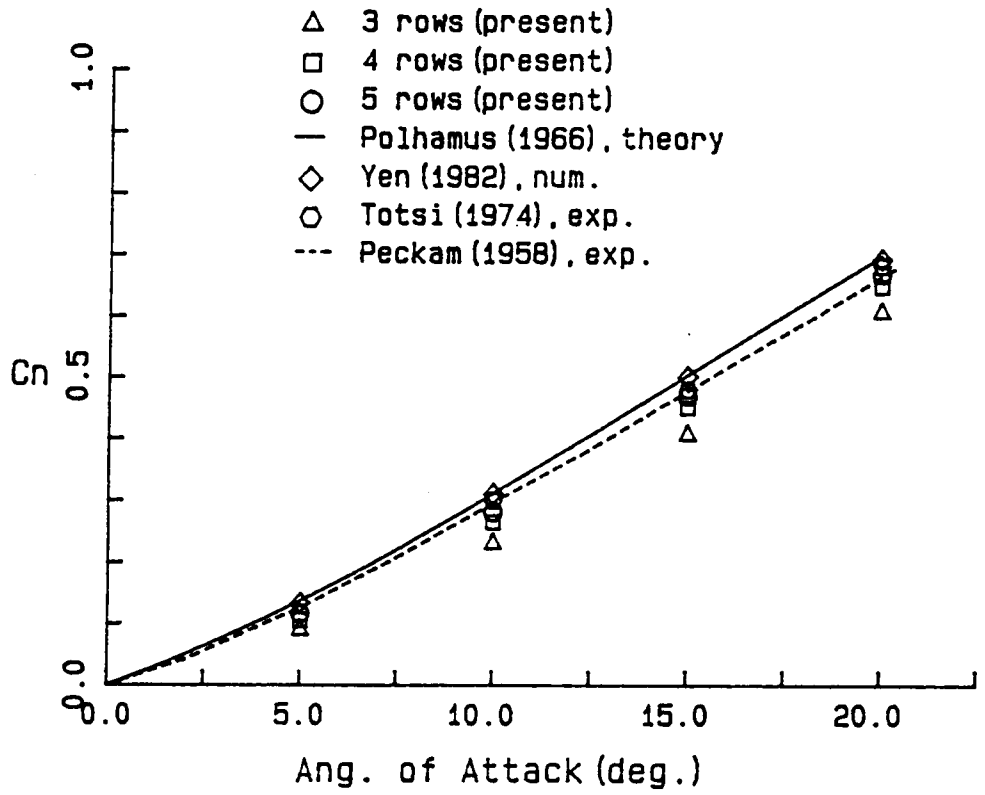

Figure 45. Convergence of normal force coefficients: the results predicted by the present method are compared with others for an 1 % thick, unit aspect flat delta wing.

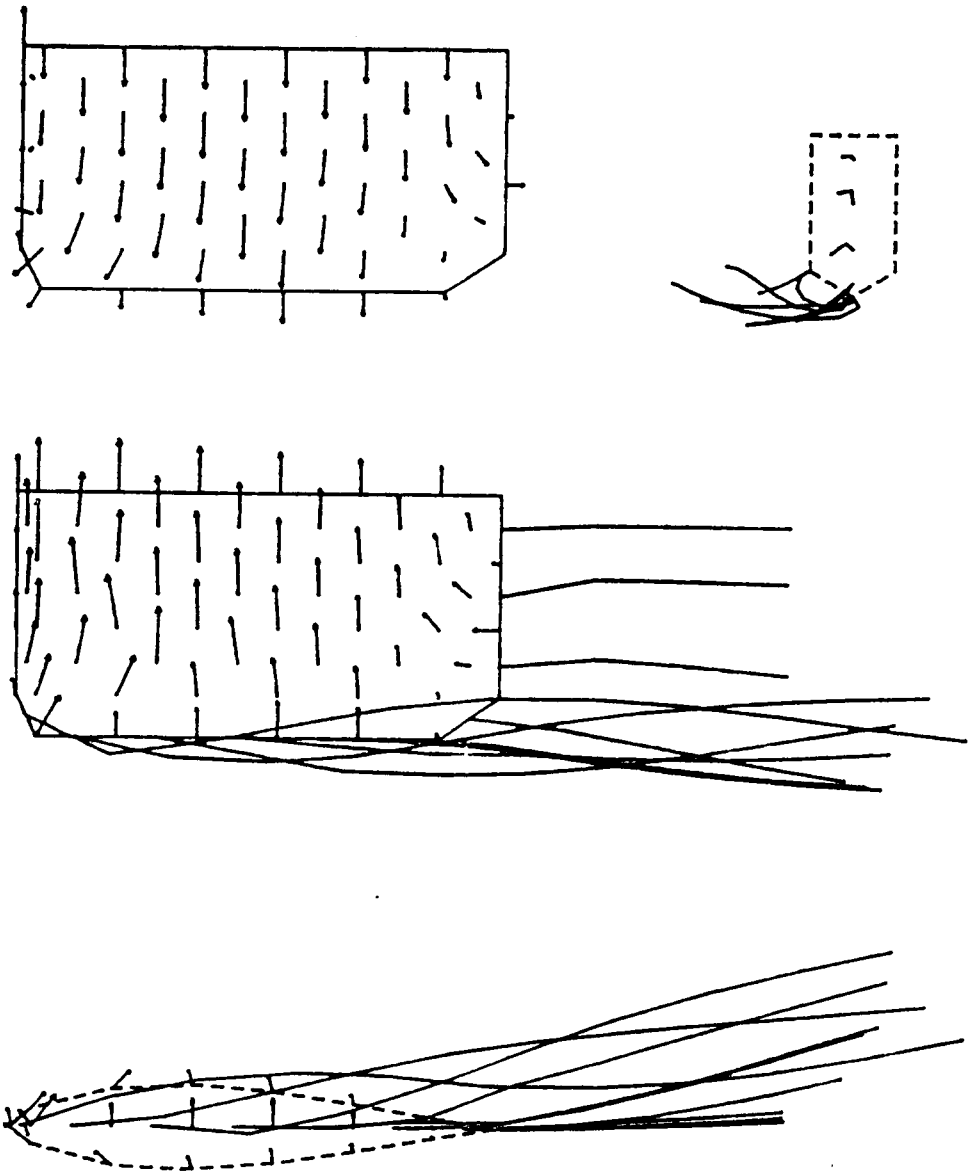

Figure 46. Wakes and vorticity distributions on a thick rectangular wing: 15 degree angle of attack, and unit aspect ratio $63_{(3)}$-013 wing.

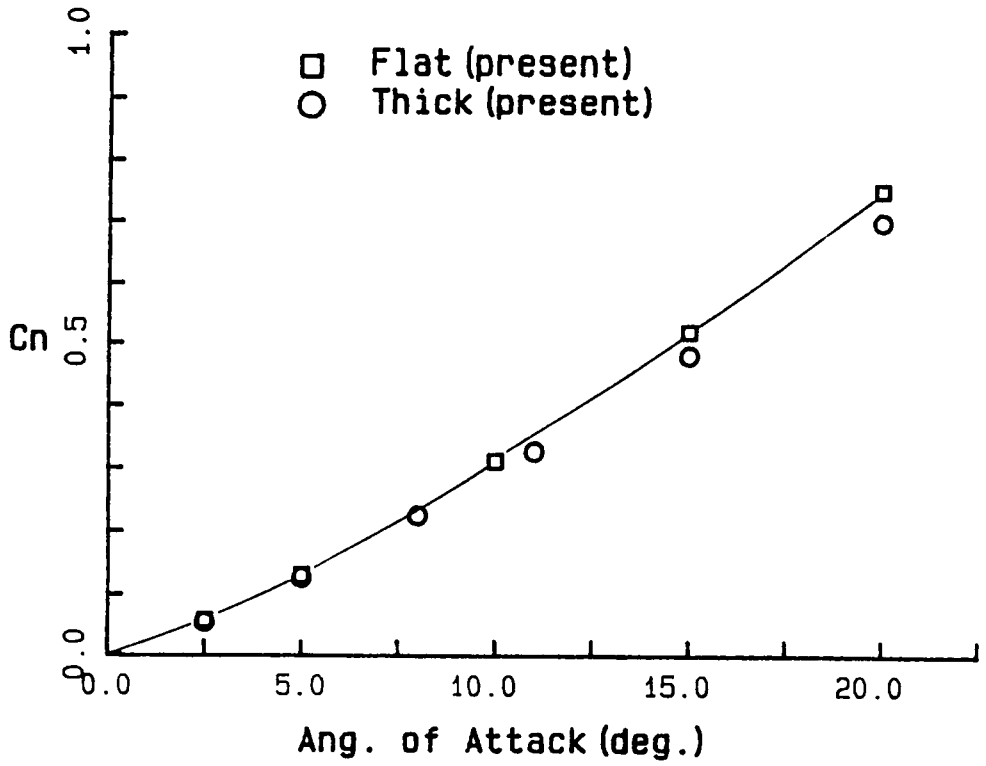

Figure 47. Normal force coefficients of a thick rectangular wing: the normal force coefficients for a unit aspect ratio, $63_{(3)}$- 013 thick wing are shown as a function of angles of attack.

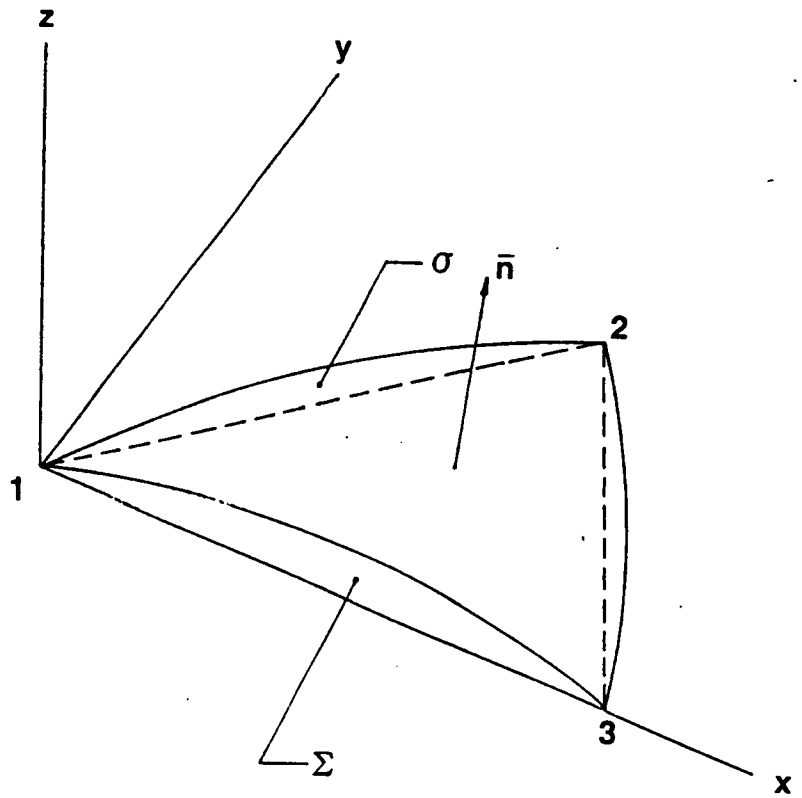

Figure 48. Simulated surface.

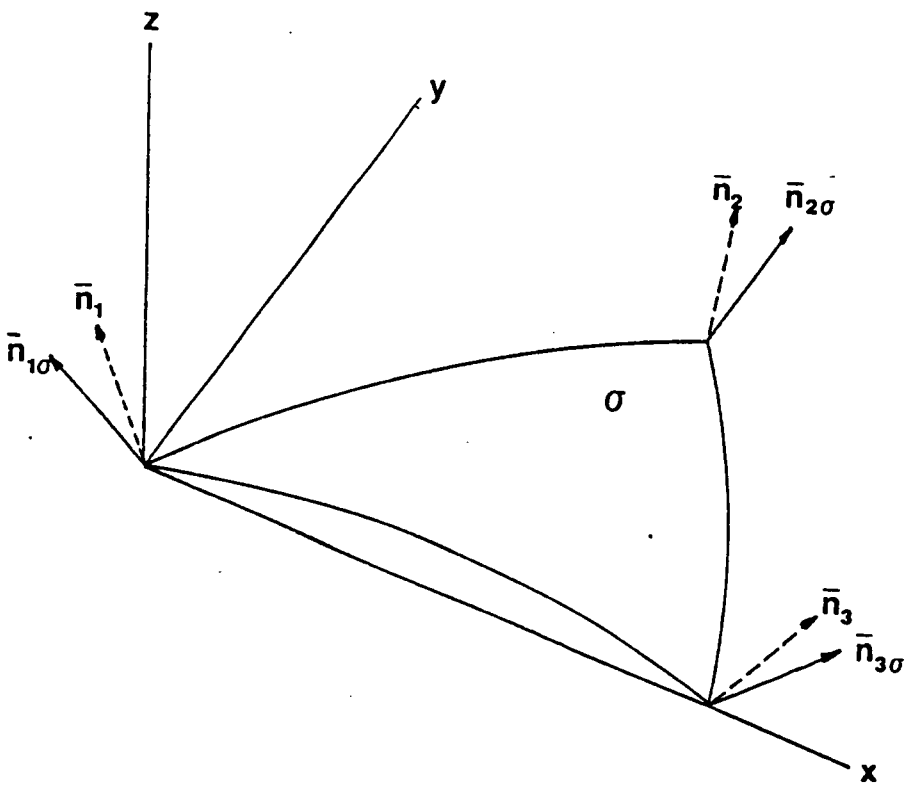

Figure 49. Determination of simulated surface.

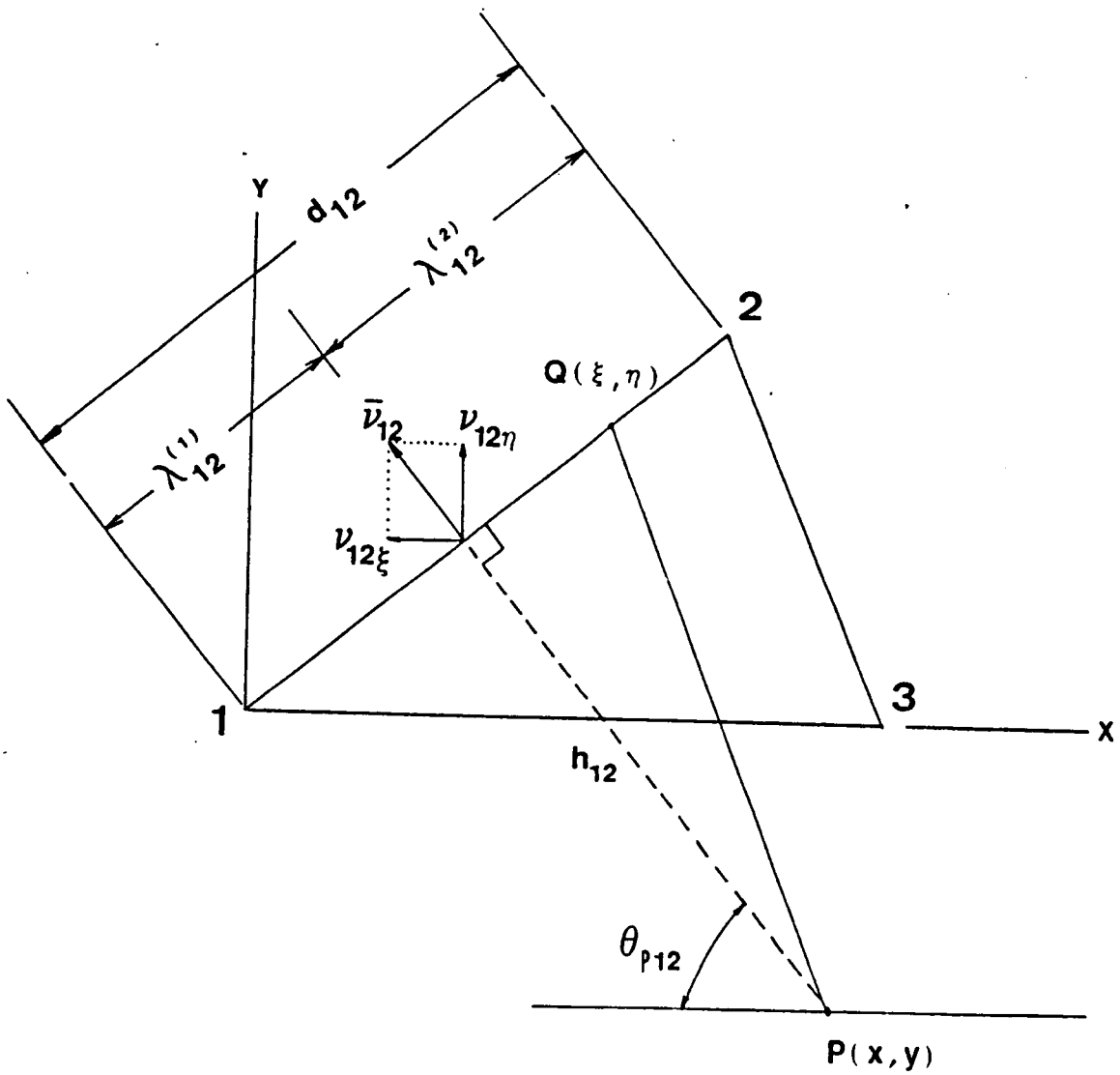

Figure 50. Geometric relationships between parameters.

The vita has been removed from the scanned document

APPLICATION OF PANEL METHODS FOR SUBSONIC AERODYNAMICS

by

Meung Jung Kim

D. T. Mook, Chairman

Engineering Mechanics

(ABSTRACT)

Several panel methods are developed to model subsonic aerodynamics. The vorticity panel method for two-dimensional problems is capable of handling general unsteady, potential, lifting flows. The lifting surface is modelled with a vortex sheet and the wakes by discrete vortices. As an imitation of the conditions at the trailing edge, stagnation conditions on both surfaces are used. The over-determined system is solved by an optimization scheme. The present predictions are in good agreement with experimental data and other computations. Moreover the present approach provides an attractive alternative to those developed earlier.

Two panel methods for three-dimensional nonlifting problems are developed. One uses source distributions over curved elements and the other vorticity distributions over flat elements. For the source formulation, the effect of weakly nonlinear geometry on the numerical results is shown to accelerate the convergence of numerical values in general. In addition, the extensive comparisons between two formulations reveal that the voticity panel method is even more stable and accurate than the curved source panel method.

Another vorticity panel method is developed to study the lifting flows past three-dimensional bodies with sharp edges. The body is mod-

elled by single vortex sheet for thin bodies and two vortex sheets for thick bodies while the wakes are modelled with a number of strings of discrete vortices. The flows are assumed to separate along the the sharp edges. The combination of continuous vorticity on the lifting surface and discrete vortices in the wakes yields excellent versatility and the capability of handling the tightly rolled wakes and predicting continuous pressure distributions on the lifting surface. The method is applied to thin and thick low-aspect-ratio delta wings and rectangular wings. The computed aerodynamic forces and wake shapes are in quantitative agreement with experimental data and other computational results.